Optical Characterization of OLED Emitter Properties by Radiation Pattern Analyses

seit 1558

DISSERTATION

zur Erlangung des akademischen Grades

doctor rerum naturalium
- Dr. rer. nat. -

vorgelegt dem Rat der Physikalisch-Astronomischen Fakultät

der Friedrich-Schiller-Universität Jena

von Diplom-Physiker Michael Flämmich

geboren am 13.02.1982 in Jena

"I learned very early the difference between

knowing the name of something and knowing something."

(Richard Feynman, 1918-1988)

"Praise the science!"

(Hans-Peter Gerdes, *1966)

Contents

Chapter 1

Introduction

Since the first report of an organic light-emitting diode (OLED) in 1987 [1], considerable progress has been achieved in improving the lifetime and efficiency of OLEDs as well as in studying the basic physics of such devices. Due to their attractive features, OLEDs are seen as promising candidates for tomorrow's display and lighting applications [2–4]. OLEDs are slim and lightweight, and the light generation process of electroluminescence yields a high electron-to-photon conversion efficiency, ideally approaching unity [5]. Most importantly, OLEDs are conceptually different from conventional, point-shaped light sources since the light is generated and emitted over a sizable area of up to square meter dimensions. Furthermore, the feasibility of a wet-chemical deposition from solution promises very low fabrication costs and is highly attractive for mass production [6–8]. Inspired by the vision of large-area lighting panels providing ergonomic and economic anti-glare illumination, researchers throughout the world in both industry and academia are developing white OLEDs for the next generation of solid-state light sources [9, 10]. Lab samples of white OLEDs can already rival with incandescent light bulbs or even fluorescent tubes in terms of efficiency [11–13] and very recently first lighting products have become commercially available.

However, one factor still limiting the overall device performance is the rather low light extraction efficiency. This is due to the fact that the energy of an excited emitter can be radiated into different optical channels and only a small fraction of the light energy is finally extracted from the device. In order to perform comprehensive optical analysis and optimization of the OLED layered system, which promise improved device efficiency, the optical

features of the internal emissive process and the OLED layered stack need to be known. The availability of meaningful and reliable optical device properties is *the* fundamental prerequisite for quantitative optical simulations and sophisticated device engineering.

For the purpose of optical modeling, the electroluminescent emissive process in OLEDs can be considered as a dipole transition from an excited molecular state into the ground state. It is important that the emissive event takes place in a microcavity and the interaction with the local environment plays a vital role. As a consequence, the radiation pattern of an OLED is generated by the interplay of the *active* optical properties of the emissive material and the *passive* optical properties of the layered system. With full details, the *active* optical properties of the emissive material are the internal electroluminescence (EL) spectrum, the profile of the emission zone, the orientation of the transition dipole moments, and the internal lumines- cence quantum efficiency; the *passive* optical properties of the layered system are the material refractive indices and the layer thicknesses. Whereas the *passive* optical properties can be measured utilizing standard spectroscopic methods [14, 15], the *active* optical properties of the emissive system are more difficult to access. Frequently, photoluminescence (PL) experiments are performed to determine the spectrum of the emissive material [16] as well as the molecular dipole orientation [17–20]. However, PL experiments generally suffer from the fact that the initially photo-generated excited states are not necessarily identical to the excited states in EL operation [21]. Furthermore, the internal features like the molecular orientation might depend on the exact deposition conditions and post-processing techniques [22]. Consequently, *in situ* investigations of OLEDs are desirable and a promising approach is based on measurements of the optical far field of OLEDs in electrical operation and subsequent optical reverse simu- lations. A variety of more or less elaborate methods utilizing the full angular, spectral, and polarization resolved radiation pattern or some essential aspects of these have been proposed, allowing conclusions to be drawn to the profile of the emission zone [23–31] and the transition dipole moment orientation [32, 33]. However, none of these studies provides any information whether the investigated part of the radiation pattern holds sufficient information about the particular internal feature of interest, and none of these studies addresses the question of how

the OLED layered system could be tuned or adapted in order to increase the sensitivity for of the internal feature of interest in the OLED far field. Furthermore, no general strategy to systematically measure all *active* optical properties of OLED emissive materials has been proposed so far.

In this thesis, novel approaches are discussed that enable an accurate *in situ* determination of the internal EL spectrum, the profile of the emission zone, the orientation of the transition dipole moments [34–36], and the internal luminescence quantum efficiency [37, 38] of OLED emitter materials from measurements of the optical far field of electrically operating OLEDs and corresponding optical reverse simulation. A fundamental idea is to utilize devices with well adapted layered systems that optically enhance the feature of interest [39, 40]. This allows to observe the internal properties of the dipole radiation in the OLED far field with sufficient sensitivity. The methods are applied to sets of OLEDs containing a blue polymeric, as well as a green and a red small-molecular emissive material, respectively, and a routine for a complete *in situ* characterization of the *active* optical properties of OLED emissive materials is demonstrated. Besides results that match the expectations and confirm common assumptions, the analyzed emitter systems exhibit truly unforeseen features that open up novel and highly promising approaches for OLED efficiency optimization.

In Chapter 2 of this thesis, an overview of the current state-of-the-art OLED technology is given, with focus on the optical processes in OLEDs that are introduced in a qualitative and descriptive manner. Chapter 3 reviews the theoretical fundament of emission from OLED-like structures. Chapter 4 introduces the underlying characterization concepts that are based on elementary features of the internal dipole radiation. A general routine is proposed in order to measure the *active* optical property of particular interest with greatest accuracy. In Chapter 5, the measurement setup, the investigated OLED systems, as well as the data analysis and fitting methods are outlined briefly. The experimental data and results are presented in Chapter 6, accompanied by a realistic approach to improve the overall efficiency of OLEDs considerably. Chapter 7 summarizes the results of this thesis and provides an outlook for desired future work.

Chapter 2

Fundamentals of OLED optics

The phenomenon of electroluminescence, "the emission of electromagnetic radiation from condensed matter subjected to an external electric field" [41], was first noted in 1907 on silicon carbide, where "a crystal of carborundum gave out a yellowish light." [42] In 1963, organic materials were found to bear electroluminescence during high-voltage application ($\geq 400\,\mathrm{V}$) to an anthracene single crystal [43]. Another 24 years had to pass before the milestone in OLED development, the first "organic electroluminescent diode" based on two thin layers of single molecular organic semiconductor materials was realized in 1987 [1]. Due to the moderate thickness of the vacuum-evaporated layers ($\approx 100\,\mathrm{nm}$), light emission at rather low driving voltages ($\approx 5\,\mathrm{V}$) was achieved with an external quantum efficiency (EQE) of about 1%. "Light-emitting diodes based on conjugated polymers" were introduced in 1990 [6]. The emissive polymeric material was fabricated by spin coating from solution and the resultant devices showed an EQE of about 0.05% at driving voltages of about 15 V.

Since these early steps, organic semiconductors have evolved rapidly from a topic of basic research to a wide range of applications that include OLEDs based on polymers [6, 44–47] or small molecules [1, 11, 13, 48–50], OLED displays [51, 52], as well as organic lasers [53–55], transistors [56, 57], and solar cells [58–62]. Nowadays, about 20 years after their first demonstration, OLEDs are seen as promising candidates for the next generation of display and lighting applications [2–4]. Although the device architectures of both technologies, OLED displays and lamps, do not differ substantially from the device optics point of view, the present work focuses on OLED structures for lighting applications.
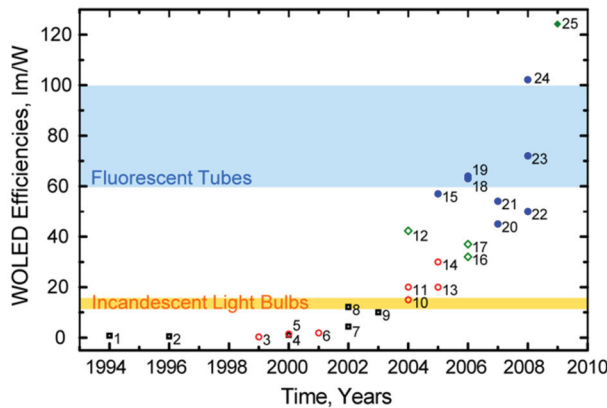
Figure 2.1. Record efficiencies of white OLEDs. Representative efficiency values (considered to be among the highest values reported at the time of their publication) are shown. References and measurement details for each data point can be found in Ref. [10]. The efficiency of incandescent lamps and fluorescent tubes, which are currently the most widely used light sources, are also indicated. Reproduced from Ref. [10] with kind permission.

Particularly with regard to lighting applications, OLEDs benefit from their unique features. The organic layer stack is typically a few 100 nm thick and, thus, the entire OLED remains an extremely thin and lightweight area light source. Moreover, the process of electro-luminescence as the basic principle of light generation is extremely efficient and potentially yields one photon per injected charge. Because the emission spectrum of most chromophores covers only some fraction of the visible spectrum, the common approach is to merge a set of different chromophores, e.g. blue, green and red, to obtain a white emission spectrum that can be tailored to the particular application by the chormophore combination.

The prospect of large-area lighting panels that provide ergonomic and economic glare-free illumination drives extensive research efforts to prepare white OLEDs for the challenges of the solid-state lighting market. Impressive numbers have been published on white OLEDs under laboratory conditions:[a] devices with a luminous efficacy in excess of 120 lm/W [13], devices with 34% EQE [63], as well as devices with a color rendering index greater than 90 and lifetimes in excess of 30.000 h at a luminance of 5000 cd/m^2 [64]. Figure 2.1 summarizes efficiency records that were achieved with white OLEDs over the past 15 years [10]. Although the efficiency of white OLEDs is continously improving, it is not yet clear if such values can be realized in commercial products, as some of the concepts employed to reach these numbers might be cost-prohibitive in mass production [10]. However, first OLED lighting products have become commercially available in 2009.[b]

---

[a]For comparison: Incandescent light bulbs show $\approx$12 lm/W efficiency and an average lifetime $<$ 3000 h [10].

[b]Commercial products are e.g. the 'Lumiblade' from Philips and the 'ORBEOS' from OSRAM. The latter features an active area of 100 cm^2 at a slimness of 2.1 mm and a weight of 24 g, a luminous efficacy of about 25 lm/W at 1000 cd/m^2, a color rendering index of 75, and a median lifetime up to 15.000 operating hours [65].

2.1 Device structure and materials

OLEDs for lighting applications are typically bottom emitting structures that emit light through the indium-tin-oxide (ITO) coated substrate glass, as indicated in Fig. 2.2. A first organic film, the hole-injection layer (HIL) or hole-transport layer (HTL), facilitates hole injection into the device as well as hole transport. On top of the following emissive layer (EML), an electron-transport layer (ETL) or electron-injection layer (EIL) is deposited that defines the distance of the emissive sites to the thermally evaporated metal cathode.

The involved organic materials are often divided into two major classes: polymers and small molecules. Since the fundamental properties of both classes are mainly the same, the division rather relates to the way thin films are prepared. Small molecules are typically thermally evaporated in vacuum [66] and polymers are processed from solution [67]. A shortcoming of thermal evaporation is a rather inefficient use of material and the required high-vacuum condition. Both can be partially circumvented by using the alternative deposition method of 'organic vapor-phase deposition', where the molecules are thermally evaporated into an inert carrier gas stream, which transports the organic material through a heated-wall system to a cool substrate where condensation occurs [68]. For thin film preparation from solution, a number of techniques are available in addition to the standard spin-coating method. Inkjet printing is of particular interest because it promises comparably low production costs [69, 70].
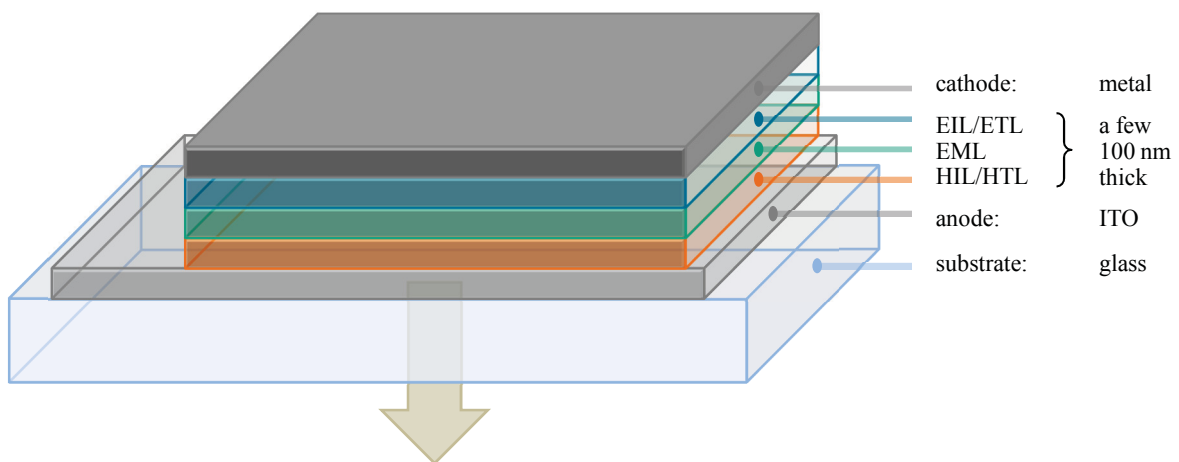
Figure 2.2. Typical structure of a multilayer bottom emitting OLED. Several organic layers are processed onto an ITO coated substrate. The stack is capped by an opaque metal cathode. Light is generated in the EML and emitted through the semitransparent ITO anode (indicated by the arrow).
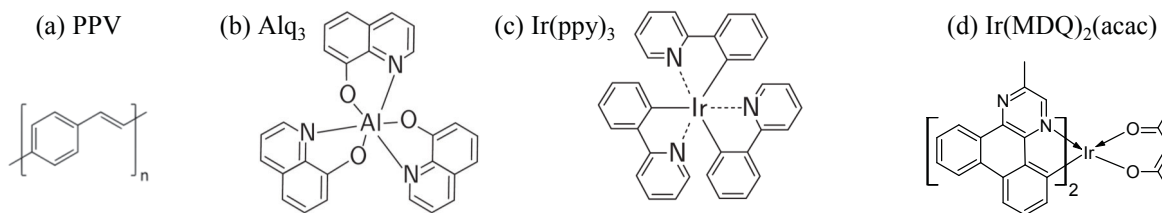
Figure 2.3. **Chemical structure of PPV, Alq$_3$, Ir(ppy)$_3$, and Ir(MDQ)$_2$(acac).** Chemical structure of common OLED emitter materials: (a) poly-(phenylene vinylene) (PPV), (b) tris(8-hydroxy-quinolinato)aluminium (Alq$_3$), (c) tris(2-phenyl-pyridine)iridium(III) (Ir(ppy)$_3$), (d) iridium(III)bis(2-methyldibenzo-[f,h]quinoxaline)-(acetylacetonate) (Ir(MDQ)$_2$(acac).

The key advantage of organic semiconductors is that their structure can be tailored to optimize a particular function such as charge carrier mobility or luminescent properties. In fact, most properties, such as ionization energy, electron affinity, energy gap, solubility, and stability in ambient air, can be widely tuned by changing the chemical composition [71]. The molecular structures of the four common OLED emitter materials are shown in Fig. 2.3. Poly-(phenylene vinylene) (PPV) is formed from a number of connected monomer units, resulting in a long chain polymer. Tris(8-hydroxy-quinolinato)aluminium (Alq$_3$), tris(2-phenyl-pyridine)iridium(III) (Ir(ppy)$_3$), and iridium(III)bis(2-methyldibenzo-[f,h]quinoxaline)-(acetylacetonate) (Ir(MDQ)$_2$(acac) are small-molecular materials that consist of a (heavy) metal central ion bound to functional organic ligands.

The electroluminescent process in OLEDs involves a recombination of electrons and holes, initially generating 25% singlet and 75% triplet excited states. Polymeric emitters are usually fluorescent and the radiative decay of triplet excitons is spin-forbidden. Depending on the molecular mass, the metal central ion of small-molecular emitters introduces spin-orbit coupling and excited triplet states are allowed to decay into the ground state radiatively as well.[c] By this means, the advancement from singlet emitting [1, 6] toward triplet harvesting materials [49, 73] is capable of pushing the internal quantum efficiency limit from 25% up to 100%. In order to combine the high internal electron-to-photon conversion ability of phosphorescent emitters with a cheap, solution based fabrication process, devices utilizing electrophosphorescent polymers showing green, red, and even white emission have been demonstrated [74–76].

---

[c]E.g. Alq$_3$ is a singlet emitter: the phosphorescence quantum yield of Alq$_3$ is extremely low because of the weak effect of the light aluminum ion (atomic number $Z = 13$) [72]. By contrast, Ir(ppy)$_3$ is a triplet emitter: the heavy metal iridium ion ($Z = 77$) enables spin-orbit coupling and allows for efficient phosphorescence [73].

2.2   Basic functionality

The basic functionality and overall efficiency of OLEDs is well described by the external quantum efficiency (EQE) that gives the number of emitted photons per injected charges [77]:

$$\text{EQE} = \gamma \cdot \eta_{S/T} \cdot q_{eff} \cdot \eta_{out} \tag{2.1}$$

The EQE is determined by four terms or rather probabilities, each of which being a number between 0 and 1: (i) Electrons and holes are injected from the cathode and the anode, respectively, and move toward the opposite electrode under the influence of the applied electric field. With the probability given by the 'charge balance factor' γ, electrons and holes accumulate in the emissive layer, recombine, and form excitons. In state-of-the-art small molecule OLEDs the recombination zone is confined within a narrow layer by applying appropriate "blocking" materials and thus, recombination of all charge carriers is achieved ($\gamma \rightarrow 1$) [78]. (ii) During the recombination of electrons and holes, excited singlet as well as triplet states are generated [79]. Following a simple statistical reasoning, 1/4 of all excitons are singlet excitons, and 3/4 are triplet excitons [80].[d] The 'singlet triplet factor' $\eta_{S/T}$ accounts for the exciton fraction that is allowed to decay radiatively, and distinguishes between fluorescent and phosphorescent emitters. As discussed in Sec. 2.1, polymeric emissive materials are usually fluorescent and only singlet excited states are allowed to decay radiatively, yielding $\eta_{S/T} \approx 0.25 \ll 1$ [79, 87]. Small-molecular emitters can utilize heavy metal ions and the resultant strong spin-orbit-coupling enables for triplet emission as well ($\eta_{S/T} \approx 1$), fundamentally promising higher efficiencies [49, 73]. (iii) The third factor regards the limited 'internal luminescence quantum efficiency' q of the excited state that gives the yield of photon-generating, radiative transitions. Today, very efficient OLED emitter materials are availiable, and reduced phonon mediated non-radiative relaxation processes promise the possibility of $q \rightarrow 1$ [73]. However, because the q-value becomes system dependent in any thin film stack due to coupling of the emitter to photonic modes of the cavity, the 'effective quantum efficiency' ($q \rightarrow q_{eff}$) has to be considered. Cavity enhanced and suppressed spontaneous decay rates were already predicted

---

[d]One should note that the issue of singlet-triplet formation ratio is still a subject of debate in the literature, and singlet fractions over 50% have been reported [79, 81–86].

in 1946 [88]. A positive exploitation of this effect is desired in OLEDs by designing smart layered systems [89]. (iv) Finally, only a fraction of the internally generated photons can leave the structure, as regarded by the 'outcoupling factor' η_{out}. Since the light is generated inside optically dense organic layers (refractive index $n \approx 1.8$) and typical OLED substrates show a refractive index of $n \approx 1.5$, η_{out} is fundamentally limited: Roughly estimating the energy transfer in a typical bottom emitting device (as sketched in Fig. 2.2) reveals that only 20% of the light energy is transferred into radiative free space modes, 20% is trapped in the substrate, and 60% is coupled to guided modes of the organics stack [35, 90]. It is evident from these numbers that a more detailed analysis of the optical processes in OLEDs and subsequently derived optimization concepts might yield devices with significantly improved performance.

2.3 Optical processes in OLEDs

Optical investigations of emission inside microcavity structures have always attracted much attention. As mentioned above, cavity depending spontaneous decay rates were already predicted (at radio frequencies) in 1946 [88]. Pioneering experimental work in 1974 demonstrated that the spontaneous emission rate of fluorescent molecules is modified in the proximity of a metal mirror [91]. In the 1990s, the luminescent properties of organic materials in thin film devices [6, 92] and general optical effects due to organic microcavities [93–95] were investigated in some more detail with experiments under optical excitation. Based on a ray optical treatment of light propagation in OLEDs, the approximation that η_{out} is proportional to $1/n^2$, where n is the refractive index of the emissive material, has been proposed in 1994 [96]. Although this simplified concept is continuously cited, it is well known today that a more rigorous treatment of the optical processes in OLEDs is essential to obtain meaningful quantitative information about the radiation pattern, optical loss channels, and the overall device efficiency of OLEDs. Current established approaches to model the emission pattern of OLEDs [97, 98] are based on the theory of radiating dipoles close to plane interfaces [99, 100]. In the following, fundamental determinants of the emission from OLEDs are discussed in a qualitative and descriptive manner; a proper theoretical description is given in Chapter 3.

From the device optics point of view, the radiation pattern of an OLED is generated by the interplay of the *active* optical properties of the emissive material and the *passive* optical properties of the surrounding layered system. With full details, the *passive* optical properties are the material refractive indices and the layer thicknesses, and the *active* optical properties are the internal electroluminescence spectrum, the profile of the emission zone, the orientation of the transition dipole moments, and the internal luminescence quantum efficiency. All these properties are illustrated in Fig. 2.4 and discussed in some detail in the following.

The lateral extension of a typical OLED ($\sim 10\,\text{cm}$) is orders of magnitude larger than the thin film stack thickness ($\sim 100\,\text{nm}$). Hence, an OLED is modeled as a layered system with homogeneous materials that are infinitely spread in two dimensions and that are confined by smooth and parallel interfaces. The thin film stack is treated coherently since the layer thicknesses are in the range of the wavelength of the propagating light, whereas an incoherent treatment is applied for layers thicker than several ten microns like e.g. glass substrates. Light propagation through such a system can be described e.g. by a matrix formalism [101] that regards the *passive* optical properties in terms of the layer thicknesses and material dispersions (d and $n(\lambda)+\mathrm{i}\kappa(\lambda)$ in Fig. 2.4, respectively). These can be measured by standard spectroscopic methods, e.g. spectroscopic ellipsometry [14, 18] or reflection-transmission spectroscopy [15].
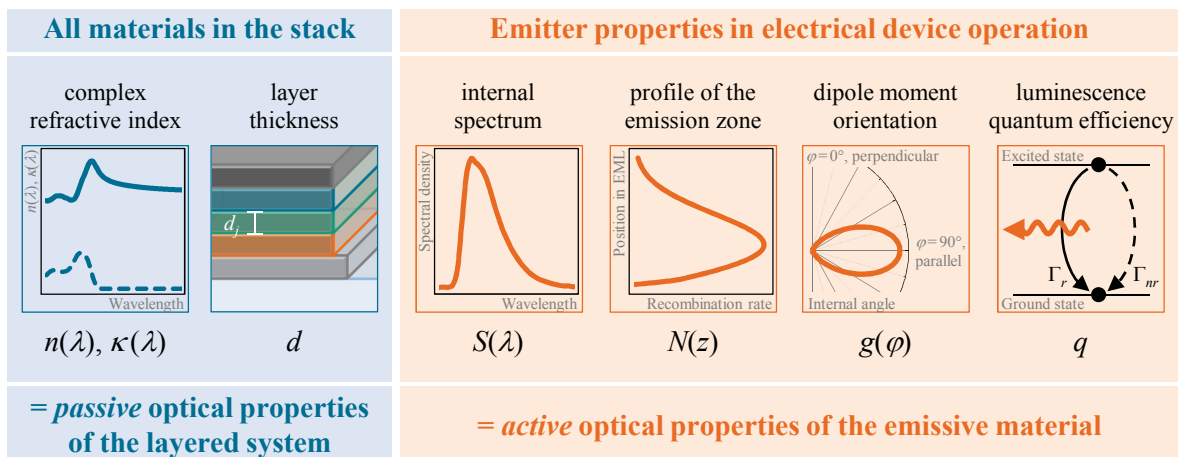
Figure 2.4. ***Passive* and *active* optical properties of OLEDs.** Schematic illustration of the set of parameters that characterizes an OLED for the purpose of optical simulation: the *passive* optical properties of the layered system (which are the material refractive indices and the layer thicknesses of all materials in the stack) and the *active* optical properties of the emissive material in electrical device operation (which are the internal electroluminescence spectrum, the profile of the emission zone, the orientation of the transition dipole moments, and the internal luminescence quantum efficiency).

The *active* optical properties of organic semiconductors are fundamentally regulated by the molecular orbitals of their conjugated π-electron system. The latter is formed by the overlapping p_z-orbitals of sp^2-hybridized C-atoms in the molecules. The delocalized π-bonds are significantly weaker than the σ-bonds that build the backbone of the molecules. Hence, the lowest-energy electronic transitions are those between the bonding π and anti-bonding π^* orbitals, as illustrated in Fig. 2.5. In organic chemistry, these molecular states are denoted as the highest occupied molecular orbital (HOMO) and the lowest unoccupied molecular orbital (LUMO), respectively. For typical luminescent materials utilized in OLEDs, the energetic difference of HOMO and LUMO ranges between 1.5–3.5 eV, covering the visible spectrum of light and, thus, corresponding to an optical excitation energy of photon-emission or -absorption.

During a LUMO→HOMO emissive event, the electron wave function and the probability density associated with the position of the electron flips from the excited molecular state into the ground state, as illustrated in Fig. 2.5. For the purpose of electromagnetic modeling, this is considered as an oscillating current density. The spatial dimensions of the molecular orbitals involved in the transition are considerably smaller than the photon wavelength, which legitimates the theoretical model of the optical transition as an oscillating point dipole $\vec{\mu}$, and typically the term 'dipole transition' is applied.

Typical emission spectra (indicated as $S(\lambda)$ in Fig. 2.4) of organic molecules are considerably broadened due to their complex morphology and disorder effects [102]. The resultant full width at half maximum of the emission spectrum is typically in the range of 0.3 eV and corresponds to $50-100$ nm spectral width. By stacking several different emitter layers in an OLED, the cumulative emission can be tuned to virtually every color including white emission. Most white OLEDs contain blue, green and red emitter layers to create high quality white light, e.g. with a high color rendering index or a desired color temperature.

Provided that the charge carriers are well distributed over the OLED area, the system is electrically homogeneous in the transverse direction, and the active sites are homogeneously distributed in the plane of the layered system interfaces. Hence, the profile of the emission zone (indicated as $N(z)$ in Fig. 2.4) is the spatial distribution of the emissive sites across the
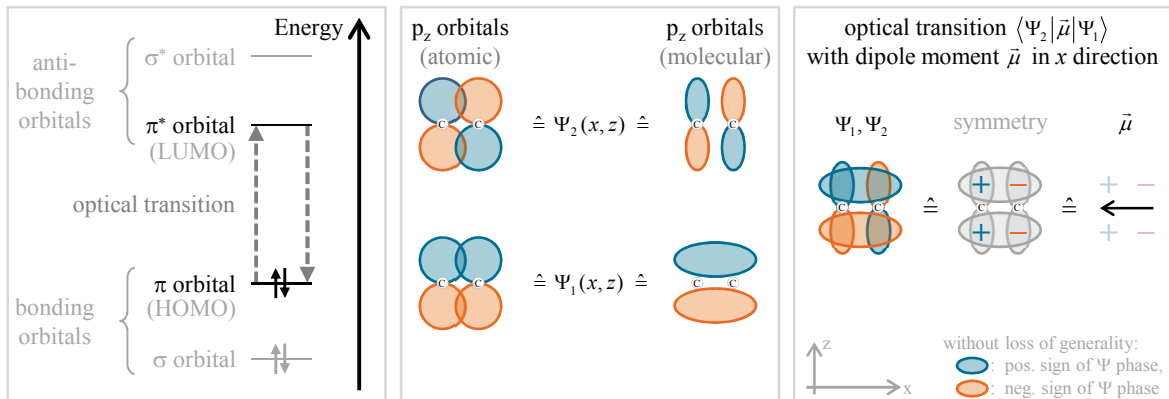
Figure 2.5. Energy levels, p_z-orbitals, and orientation of transition dipole moment. With disregard to any rigorous treatment all schematics are intended for illustration purposes only. Left frame: Energy levels of a π-conjugated molecule. The lowest electronic excitation is between the bonding π orbital (HOMO) and anti-bonding π^* orbital (LUMO). Middle frame: As an example for the simplest conjugated π-electron system, the molecular orbitals of ethene in the ground state (π, lower plot) and the excited state (π^*, upper plot) are drawn schematically. For simplicity, only the optically relevant p_z-orbitals are shown alongside the two carbon atoms. Molecular orbitals (right) are found by combining atomic orbitals (left). Right frame: During an electronic transition, the molecular orbital or rather the electron wave function flips from the excited molecular state into the ground state. Due to the wave function symmetry, the transition dipole moment $\vec{\mu}$ lies along the axis that is connecting the two carbon atoms. More complex molecules have more complex LUMO and HOMO structures and the derivation of the transition dipole moment orientation is not straight-forward.

height z in the active layer. It is given by the charge-carrier recombination zone, potentially broadened by exciton diffusion [103]. The former mechanism of electron and hole recombination severely depends on the particular properties of charge injection and charge transport in the whole OLED stack. It is primarily influenced by the properties of each single material but also by the constitution of all interfaces [104, 105]. The latter attribute, the diffusion length of the excitons after their formation, is an emissive material specific parameter that can be measured indirectly only by experiments using sensing layers [79, 106–111]. In multilayer small-molecular OLEDs the exciton formation zone is usually well localized in the thin emission layer, whereas polymeric OLEDs show typically a rather broad emission zone [46, 112]. The dominant type of charge carrier in the emissive layer and the balance point of the emission origin can be estimated by measuring the electronic properties of the involved materials and modeling the charge carrier dynamics in the device [113–117]. Approaches to measure the emission zone directly are based on measurements of the optical far field of OLEDs and subsequent optical simulations. A variety of more or less elaborate methods utilizing the

full angular, spectral, and polarization resolved radiation pattern or some essential aspects of these have been proposed [23–31]. Recently, it has been demonstrated that devices with adapted layered systems are essential to observe the origin of emission in the OLED far field accurately [39].

The orientation of the transition dipole moments in spontaneously emitting materials utilized in OLEDs is determined by the molecular morphology of the particular material. Due to the fabrication process, the dipoles are isotropically orientated in the plane of the layered system interfaces, whereas a non-isotropic distribution with respect to the layered system normal is possible (indicated as $g(\varphi)$ in Fig. 2.4, where φ is the internal angle of the dipole moment with respect to the layered system normal). Considering polymeric materials deposited from solution by spin-coating, the polymer chains usually align in the plane of the film and the emissive sites tend to adopt this preferential orientation, as indicated by various photoluminescence and Raman studies [21, 118–123]. This is illustrated in Fig. 2.5 for ethene as the simplest π-conjugated system. The symmetry of LUMO and HOMO allow a dipole transition only with the dipole moment aligned along the axis connecting the carbon atoms [124]. This is in the direction of the polymer backbone that is assumed to lie in the plane of the film. Still, the chromophore could be attached to a polymer side-chain rather than to the backbone, which would cancel any orientation-correlation suggested from the spin-coating process. For a long time, vacuum deposited small molecule materials were believed to have no preferred emitter orientation due to their rather isotropic, small molecular structure [125–127]. Strong birefringence accompanied by a preferred parallel orientation of the transition dipole moments in vacuum deposited, fluorescent small-molecular films was observed just recently in photoluminescence investigations and attributed to the increased molecular length of the molecules [17, 18]. General methods to measure the orientation of the emissive sites in optically excited OLED stacks [19, 20] and electrically operating devices [34, 35] have been introduced lately. An unexpected, mainly parallel orientation of the transition dipole moments was observed in phosphorescent materials just recently as well [36], promising considerably enhanced optical outcoupling efficiencies for small molecule devices.

The internal luminescence quantum efficiency (indicated as q-value in Fig. 2.4) is an intrinsic material property of spontaneously emitting materials and denotes the probability of the excited state to relax into the ground state radiatively. The q-value has an outstanding impact on the overall performance of OLEDs: it is not only a multiplicative factor to the EQE but also affects the rate of radiative emission [37, 128]. Hence, the q-value significantly influences the optimal emitter position in planar devices [37, 127, 129, 130] and plays a crucial role for optical OLED optimization strategies [37, 66, 126, 131]. There are well known approaches to determine the q-value by means of photoluminescence experiments on single supported films using optical excitation [132]. However, in addition to the two distinct excitation processes in optical and electrical operation, the local environment of an emissive site in an electrically excited device cannot be compared to its local environment under optical excitation: Because the rate of phonon-mediated, non-radiative transitions e.g. severely depends on the local temperature, q usually changes with driving conditions and charge carrier densities [66, 133]. In order to consider these effects properly, an *in situ* measurement of q in electrical operation is desirable. The q-value is frequently estimated from the measured EQE of OLEDs [5, 16, 32, 96, 127, 134]. However, it can be seen from Eq. (2.1) that this approach requires precise knowledge of the optical outcoupling efficiency and, more importantly, assumptions on the charge recombination probability γ and the singlet/triplet excitation ratio $\eta_{S/T}$. The latter values are only rough estimates for small-molecular and polymeric material systems and thus, a resultant q-value is debatable. Consequently, a relative measurement would be preferable in order to reduce the number of assumptions involved in the analysis [37].

As an interim résumé it is underlined that the *active* optical properties of the emissive material severely affect the OLED performance, the radiation pattern, and, more importantly, the overall device efficiency. In return, it should be possible to determine these internal features by measuring the optical far field of devices in electrical operation with corresponding optical simulation and sophisticated analysis. The overriding ambition of this thesis is to provide universally valid methods for this purpose.

Chapter 3

Theoretical background: Dipole emission in layered systems

In a luminescent material, light is generated via the transition from an excited molecular state to the ground state. A photon is emitted with its energy corresponding to the energy difference between the two states. Even though this transition is a quantum mechanical process, its optical behavior can be modeled using classical electromagnetism: the decaying exciton is treated as an oscillating electrical dipole.

This chapter reviews the theoretical fundament of emission from OLED-like structures. Although the presented optical model is similar to the simulation tools established by other groups and discussed elsewhere [103, 126, 135–137], all calculations in this thesis are performed with an in-house software tool [138]; its central concepts are discussed in this chapter.

The notation of electromagnetic fields in an arbitrary layered system is elaborated at first. As a next step, the emitted power from a radiating dipole is examined for the case that the dipole is embedded in an infinite, homogeneous medium. Because the event of spontaneous emission is a quantum mechanical process, the probability of photon emission is varied when the emissive process takes place in a modified optical environment. This 'microcavity effect' results in an altered relative emission rate that is essential for OLED optics. The considerations are applied to an ensemble of emissive sites to model the radiation pattern and overall device efficiency of OLEDs. All optical determinants that are particularly relevant for the investigations in the following chapters are identified and elaborated in detail.

3.1   The electromagnetic fields in an arbitrary layered system

The notation of electromagnetic fields in a system of parallel slabs is established in this section. Figure 3.1 shows an emissive medium that contains the sources of light generation and that is embedded in an arbitrary stack of layers. Each layer j has a certain thicknesses d_j and consists of an optical medium that is isotropic, homogeneous, linear, and nonmagnetic (permeability $\mu(\mathbf{r}) = 1$). Its relevant properties for the present optical considerations are described by the wavelength-dependent complex refractive index $\widetilde{n}_j(\lambda) = n_j(\lambda) + \mathrm{i}\,\kappa_j(\lambda)$, with refractive index $n_j(\lambda)$ and extinction coefficient $\kappa_j(\lambda)$. The coordinate system is chosen in a way that the thin films are infinitely spread in the x–y plane and the z axis is perpendicular to the interfaces. The stack is surrounded by two semi-infinite media, the "cladding" in $+z$ direction and the "substrate" in $-z$ direction, with refractive indices of $\widetilde{n}_c = n_c$ and $\widetilde{n}_s = n_s$, respectively.

Maxwell's Equations [139, 140] are the basic equations to describe electromagnetic phenomena. In the form given here, they interrelate the space ($\mathbf{r}$) and angular frequency (ω) dependent electric $\bar{\mathbf{E}}(\mathbf{r},\omega)$ and magnetic fields $\bar{\mathbf{H}}(\mathbf{r},\omega)$ as well as the electric displacement field $\bar{\mathbf{D}}(\mathbf{r},\omega)$ and the magnetic induction $\bar{\mathbf{B}}(\mathbf{r},\omega)$ with the charges $\bar{\rho}(\mathbf{r},\omega)$ and current densities $\bar{\mathbf{j}}(\mathbf{r},\omega)$:

$$\nabla \cdot \bar{\mathbf{D}}(\mathbf{r},\omega) = \bar{\rho}(\mathbf{r},\omega) \qquad\qquad \nabla \cdot \bar{\mathbf{B}}(\mathbf{r},\omega) = 0$$

$$\nabla \times \bar{\mathbf{E}}(\mathbf{r},\omega) = \mathrm{i}\omega\bar{\mathbf{B}}(\mathbf{r},\omega) \qquad\qquad \nabla \times \bar{\mathbf{H}}(\mathbf{r},\omega) = \bar{\mathbf{j}}(\mathbf{r},\omega) - \mathrm{i}\omega\bar{\mathbf{D}}(\mathbf{r},\omega)\,. \qquad (3.1)$$

The frequency dependent quantities in Eqs. (3.1) are related to temporal (t) quantities by the Fourier transform that reads e.g. for the electric field as

$$\mathbf{E}(\mathbf{r},t) = \frac{1}{2}\int \bar{\mathbf{E}}(\mathbf{r},\omega)\exp(-\mathrm{i}\omega t)\mathrm{d}\omega + c.c.\,, \qquad (3.2)$$

where $c.c.$ denotes the complex conjugate. In case of optical media with the characteristics specified above, the material equations (or constitutive relations) $\bar{\mathbf{D}}(\mathbf{r},\omega) = \epsilon(\mathbf{r},\omega)\epsilon_0 \cdot \bar{\mathbf{E}}(\mathbf{r},\omega)$ and $\bar{\mathbf{B}}(\mathbf{r},\omega) = \mu_0 \cdot \bar{\mathbf{H}}(\mathbf{r},\omega)$ link the electromagnetic fields to the material properties. The parameters ϵ_0 and μ_0 are the permittivity and permeability in vacuum, respectively. The most important material parameter for optical considerations is the permittivity ϵ that can be expressed in terms of the refractive index: $\epsilon(\mathbf{r})^2 = \widetilde{n}(\mathbf{r})$. For the piecewise homogeneous system depicted in Fig. 3.1, any position $\mathbf{r}$ is associated with a particular medium j: $\widetilde{n}(\mathbf{r}) \to \widetilde{n}_j$.
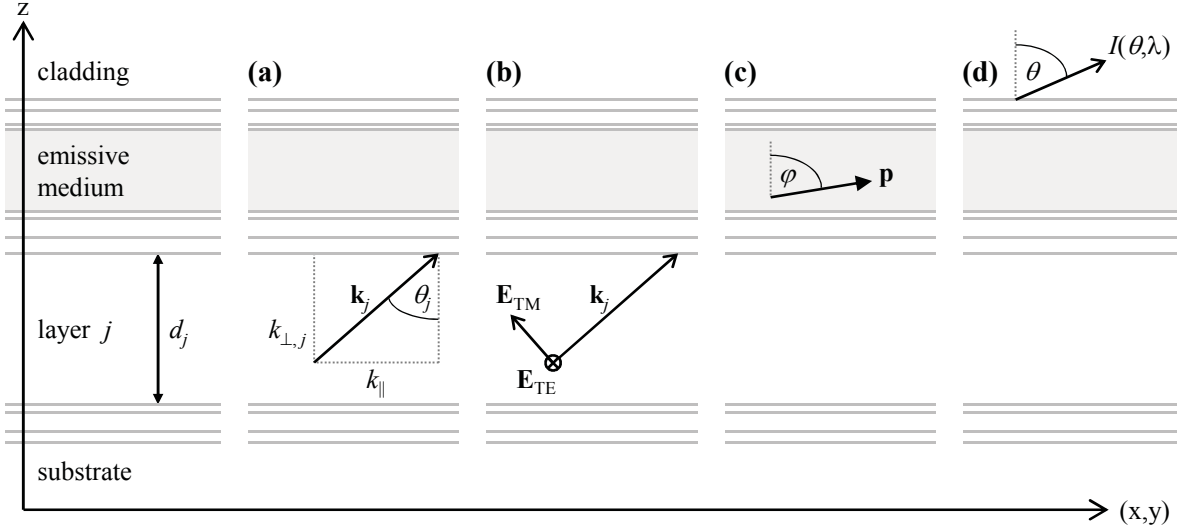
Figure 3.1. Layered system, wavevector, polarization, dipole moment, and radiance. Sketch of an arbitrary layered system. The coordinate system is chosen that all interfaces are parallel to the x–y plane. Illustrations of (a) the wavevector components, (b) the polarization states, (c) the dipole moment, and (d) the direction of observation are also shown.

A harmonically oscillating field that propagates in an optical medium can be written as a Fourier integral of plane waves, representing the decomposition in normal modes of the homogeneous medium:

$$\bar{\mathbf{E}}(\mathbf{r}, w) = \int \hat{\mathbf{E}}(\mathbf{k}, \omega) \exp(\mathrm{i}\mathbf{k}\mathbf{r}) \mathrm{d}\mathbf{k}$$

$$\bar{\mathbf{H}}(\mathbf{r}, w) = \int \hat{\mathbf{H}}(\mathbf{k}, \omega) \exp(\mathrm{i}\mathbf{k}\mathbf{r}) \mathrm{d}\mathbf{k}. \tag{3.3}$$

Inserting the Fourier amplitudes of the electric $\hat{\mathbf{E}}(\mathbf{k}, \omega)$ and magnetic fields $\hat{\mathbf{H}}(\mathbf{k}, \omega)$ from Eqs. (3.3) into Maxwell's Equations (3.1) yields the dispersion relation [140, 141] that connects the wavevector $\mathbf{k}$ and the wavelength λ of propagating light in a medium j:

$$|\mathbf{k}_j(\lambda)| = k_j = (k_{x,j}^2 + k_{y,j}^2 + k_{z,j}^2)^{1/2} = \frac{\omega}{\mathrm{c}}\widetilde{n}_j(\lambda) = \frac{2\pi}{\lambda}\widetilde{n}_j(\lambda). \tag{3.4}$$

The real part of the wavevector $\mathrm{Re}[\mathbf{k}]$ is always perpendicular to the phase fronts and defines the direction of propagation. The imaginary part $\mathrm{Im}[\mathbf{k}]$ describes the attenuation of light.

The system under study is isotropic with respect to the x–y plane. To simplify matters, both horizontal wavevector components $k_{x,j}\cdot\mathbf{e}_x$ and $k_{y,j}\cdot\mathbf{e}_y$ can be combined to the in-plane wavevector $\mathbf{k}_{\parallel}$ as illustrated in Fig. 3.1(a). Its magnitude

$$k_{\parallel} = (k_{x,j}^2 + k_{y,j}^2)^{1/2} \tag{3.5}$$

is constant in every medium due to transition conditions. The z component of the wavevector is vertical to all interfaces and its magnitude

$$k_{z,j} = \pm k_{\perp,j} = \pm\sqrt{k_j^2 - k_\parallel^2}\,, \text{ with } \mathrm{Re}[k_{\perp,j}] \geq 0\,, \tag{3.6}$$

is directly calculated from the dispersion relation in the particular medium.[a] In absorption-free media ($\kappa = 0$) and considering the case of propagating plane waves ($k_{z,j} \in \mathbb{R}$), the magnitude of the in-plane wavevector

$$k_\parallel = k_j \sin\theta_j \tag{3.7}$$

defines the angle of propagation. For $\theta_j < \pi/2$ the wave propagates in $+z$ direction, and for $\theta_j > \pi/2$ in $-z$ direction. By contrast, in the evanescent case ($k_{z,j} \in \mathbb{C}$) no real propagation angle θ_j can be associated with the wave.

All following derivations are conducted for the electric fields; the corresponding magnetic fields can be easily derived from Maxwell's Equations (3.1) if necessary.

Due to the x–y-isotropy of the layered system shown in Fig. 3.1, there is no outstanding x or y direction. Without loss of generality, the x-z plane is chosen as the plane of observation, that is determined by the surface normal of the interfaces and the particularly chosen direction of light propagation (see Fig. 3.1). The electro-magnetic fields separate into the two independent polarization states, transverse electric "TE" and transverse magnetic "TM":

$$\mathbf{E} = \mathbf{E}_{\mathrm{TE}} + \mathbf{E}_{\mathrm{TM}}\,, \quad \text{with} \quad \mathbf{E}_{\mathrm{TE}} = \begin{pmatrix} 0 \\ E_y \\ 0 \end{pmatrix}, \quad \mathbf{E}_{\mathrm{TM}} = \begin{pmatrix} E_x \\ 0 \\ E_z \end{pmatrix}. \tag{3.8}$$

These different field components are illustrated in Fig. 3.1(b). The TE polarization contains electric field components that are perpendicular to the plane of observation and oscillate strictly parallel to the interfaces. The TM polarization oscillates parallel to the plane of incidence and contains both, parallel and perpendicular electric field components[b].

---

[a] In Eq. (3.6), $k_{z,j}$ is a complex square root and two solutions exist. In absorbing media ($\kappa \neq 0$), k_j and $k_{z,j}$ are complex and the amplitudes of propagating waves are attenuated in positive (for $\mathrm{Re}[k_{z,i}] > 0$) or negative (for $\mathrm{Re}[k_{z,i}] < 0$) z direction. In absorption-free media ($\kappa = 0$ and $k_j \in \mathbb{R}$) $k_{z,j}$ is either purely imaginary or real. The first case describes evanescent waves with exponential decaying amplitude in z direction, whereas real $k_{z,j}$ specify plane waves that propagate at an angle of θ_j to the z direction [see Fig. 3.1 and Eq. (3.7)].

[b] In the latter case the corresponding magnetic field $\mathbf{H}_{\mathrm{TM}}$ is strictly parallel to the interfaces.

3.2 Basic theory of dipole emission

The electroluminescent emissive process in OLEDs is considered as a dipole transition (see Section 2.3). Thus, a single emitter is classically modeled by a continuously oscillating electrical dipole, a Hertz dipole: $\mathbf{p}\cos(\omega_0 t)$, oscillating with the angular frequency ω_0. A dipole moment located at $\mathbf{r_0}$ is associated with a source current density $\bar{\mathbf{j}}(\mathbf{r}, \omega)$ by

$$\bar{\mathbf{j}}(\mathbf{r}, \omega) = -\mathrm{i}\omega \cdot \mathbf{p} \cdot \delta(\mathbf{r} - \mathbf{r_0}) \cdot \delta(\omega - \omega_0) \,. \tag{3.9}$$

The electric field $\bar{\mathbf{E}}(\mathbf{r}, \omega)$ of any stationarily oscillating source current density distribution $\bar{\mathbf{j}}(\mathbf{r}, \omega)$ can be calculated using the dyadic Green's function $\mathbf{G}(\mathbf{r}, \mathbf{r}')$ of the system [100, 142]:

$$\bar{\mathbf{E}}(\mathbf{r}, \omega) = \mathrm{i}\omega\mu_0 \int \mathbf{G}(\mathbf{r}, \mathbf{r}') \cdot \mathbf{j}(\mathbf{r}', \omega) \, \mathrm{d}^3 \mathbf{r}' \,. \tag{3.10}$$

The integration is performed over the whole volume containing sources. Thus, the field in entire space is represented by the coherent superposition of all source contributions. For the present considerations, the interaction of emissive sites can be neglected, and the emission of single, independent emitters is taken into account only. The real emission from a device is then calculated by an incoherent superposition of emitters by using appropriate weighting functions, as discussed in more detail in Section 3.5.

Note that the Green's function $\mathbf{G}(\mathbf{r}, \mathbf{r}')$ in Eq. (3.10) is a 3x3 matrix transforming the three current density components into the corresponding electric field components. In this study, a transfer-matrix formulation is applied in order to calculate $\mathbf{G}(\mathbf{r}, \mathbf{r}')$ of arbitrary layered systems. Further details on the generation of the Green's function and the dipole fields can be found in Ref. [128] and references therein.

Inserting Eq. (3.9) into Eq. (3.10) yields the electric field of a single emitter in the entire space: $\bar{\mathbf{E}}(\mathbf{r}, \omega) = \omega^2 \mu_0 \cdot \mathbf{G}(\mathbf{r}, \mathbf{r_0}) \cdot \mathbf{p} \cdot \delta(\omega - \omega_0)$. A far field expansion transforms the location of measurement or observation $\mathbf{r}$ into a direction of emission represented by the wavevector $\mathbf{k}$: $\mathbf{k} = (2\pi/\lambda) \cdot n_{obs} \cdot (\mathbf{r}/|\mathbf{r}|)$, where n_{obs} is the refractive index of the absorption free medium of observation (e.g. the cladding in Fig. 3.1). The time averaged pointing vector $\mathbf{S} = \frac{1}{2}\mathrm{Re}[\bar{\mathbf{E}} \times \bar{\mathbf{H}}^*]$ yields the power $P^{dipole}(\theta, \omega)$ per solid angle interval $\mathrm{d}\Omega$ that is emitted from the dipole into

the medium of observation [140]:

$$\frac{\mathrm{d}^2 P^{dipole}(\theta,\omega)}{\mathrm{d}\Omega \cdot \mathrm{d}\omega} = \frac{4\pi^2}{2} \cdot \frac{n_{obs}}{\mu_0\, c} \cdot k_{z,obs}^2 \left| \hat{\mathbf{E}}(\mathbf{k},\omega) \right|^2 . \tag{3.11}$$

In Eq. 3.11, $c = (\epsilon_0 \mu_0)^{-1/2}$ denotes the speed of light in vacuum and $\hat{\mathbf{E}}(\mathbf{k},\omega)$ represents the Fourier amplitude of the electric field according to Eq. (3.3). The total power emitted from the dipole, including radiative and guided modes as well as potential absorption, is found from Poynting's theorem [140]:

$$\frac{\mathrm{d}p_{tot}^{dipole}}{\mathrm{d}\omega} = -\frac{1}{2} \int \mathrm{Re}[\bar{\mathbf{E}}(\mathbf{r},\omega) \cdot \mathbf{j}(\mathbf{r},\omega)^*]\, \mathrm{d}V , \tag{3.12}$$

The integration is performed over a small volume encircling the emitter (epsilon environment). The index *dipole* in Eqs. (3.11) and (3.12) refers to the power emitted by a single dipole.

3.3 Spontaneous emission and the emitter lifetime

So far, the fields of a continuously oscillating Hertz dipole have been calculated based on a classical electrodynamic description; the emission is assumed to be monochromatic and temporal infinitely extended, respectively. However, a real emitter is unlikely to radiate continuously and behaves somehow different: Once the excited state is reached, the emitter will relax into the ground state after a certain time period τ or rather with a certain rate Γ. The probability that a photon is emitted during this transition is given by

$$q = \frac{\Gamma_r}{\Gamma_r + \Gamma_{nr}} , \quad 0 \leq q \leq 1 . \tag{3.13}$$

The internal luminescence quantum efficiency q is an intrinsic material property of spontaneously emitting materials and describes the ratio of radiative transitions (with rate Γ_r) with respect to all transitions including competing non-radiative excited state depopulation (with rate Γ_{nr}). The total transition rate equals the inverse lifetime of the excited state:

$$\frac{1}{\tau} \equiv \Gamma = \Gamma_r + \Gamma_{nr} . \tag{3.14}$$

In a very efficient emissive material the radiative events dominate the non-radiative ones ($\Gamma_r \gg \Gamma_{nr}$, $q \to 1$), whereas an inefficient material allows for many non-radiative events and the emission of a photon is rather unlikely ($\Gamma_r \ll \Gamma_{nr}$, $q \to 0$).
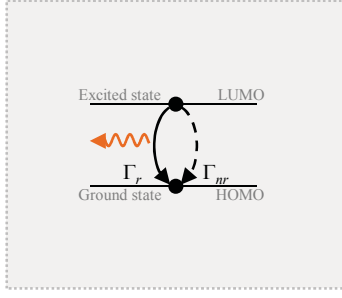
homogeneous medium: Γ_r **layered system / cavity:** Γ_r^*
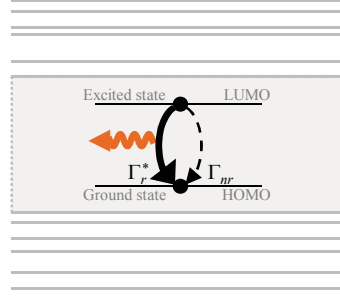
Figure 3.2. Modified radiative transition rate. The radiative rate of a transition from an excited state to the ground state is modified in a layered system or cavity (right) compared to the homogeneous medium (left). This is known as 'Purcell effect' or 'microcavity effect'.

It is well known that the spontaneous emission rate of a transition changes when the emissive system is placed in a microcavity or in a layered system [88, 91, 99, 143]: $\Gamma_r \rightarrow \Gamma_r^{cav} \equiv \Gamma_r^*$, whereas non-radiative transitions are assumed to be unaffected by the surrounding system: $\Gamma_{nr}^* \equiv \Gamma_{nr}$, as illustrated in Fig. 3.2. Thus, the lifetime of an excited state and the total transition rate in a cavity become:

$$\frac{1}{\tau^*} = \Gamma^* = \Gamma_r^* + \Gamma_{nr}\,. \tag{3.15}$$

Referring to the lifetime or emission rate in the homogeneous medium given in Eq. (3.14), a relative lifetime or transition rate is introduced:

$$\frac{1}{\tau_{rel}} = \frac{\tau}{\tau^*} = \Gamma_{rel} = \frac{\Gamma^*}{\Gamma} = \frac{\Gamma_r^* + \Gamma_{nr}}{\Gamma_r + \Gamma_{nr}}\,. \tag{3.16}$$

Similar to Eq. (3.13), the *effective* internal luminescence quantum efficiency q_{eff} can be defined

$$q_{eff} = \frac{\Gamma_r^*}{\Gamma_r^* + \Gamma_{nr}}\,, \quad 0 \leq q_{eff} \leq 1\,, \tag{3.17}$$

that is the probability of the excited state *in the cavity* to relax in the ground state radiatively.

In order to quantify the variation of the radiative rate due to the presence of the layered system, the equivalence between the probability for spontaneous emission of a photon via a dipole transition and the radiated power of a classical dipole source in the corresponding layered system is utilized (see e.g. Ref. [99]). When the presence of a thin film cavity increases the total power radiated by the dipole, then the corresponding probability for the excited state to emit a photon will increase by the same factor [97]:

$$\Gamma_r^* = F\Gamma_r = \frac{p_{tot}^{cav}}{p_{tot}^{hom}}\Gamma_r\,. \tag{3.18}$$

By this means, the effect of the cavity on the radiative transition rate is expressed in terms of the total radiated power in the system p_{tot}^{cav} with respect to the one in the homogeneous medium p_{tot}^{hom} – both are calculated according to Eq. (3.12). The indices *hom* and *cav* refer to the dipole in the *homogeneous medium* and in a *cavity*, respectively.

The relative transition rate according to Eq. (3.16) can now be rendered:

$$\Gamma_{rel} = 1 + q \left(\frac{p_{tot}^{cav}}{p_{tot}^{hom}} - 1 \right) . \tag{3.19}$$

Thus, the variation of the emission rate can be evaluated when the internal luminescence quantum efficiency q of the emitter and the total emitted power in the cavity with respect to the homogeneous medium are known. This expression of the relative transition rate highlights: For the low-q limiting case $(q \rightarrow 0)$, where non-radiative transitions dominate the depopulation of the excited state, no influence of the cavity on the emission rate is present. By contrast, cavity effects have a more pronounced influence and directly scale Γ_{rel} when employing high-q emitters. The latter case of $q \rightarrow 1$ is obviously the desired one for efficient OLED systems.

The total radiative emission from a dipole transition in a cavity or layered system follows from Eqs. (3.13) and (3.17):

$$\eta^{cav} = \frac{q_{eff}}{q} = \frac{1}{\Gamma_{rel}} \cdot \frac{p_{tot}^{cav}}{p_{tot}^{hom}} . \tag{3.20}$$

This measure represents the efficiency of a spontaneous radiative decay in a cavity, with respect to the same emitter in the homogeneous medium. The factor $1/\Gamma_{rel}$ accounts for the quantum nature of the spontaneous emission. The term $p_{tot}^{cav}/p_{tot}^{hom}$ represents the ratio of the total power emitted from the excited state in the cavity with respect to the homogeneous medium. Both power values are obtained by classical electrodynamics as described in Section 3.2.

3.4 Dipole emitter ensembles and appropriate distributions

The Equations (3.18)-(3.20) suggest to normalize all classical optical power values to the totally irradiated power of a corresponding dipole in the homogeneous medium. The reason for this normalization originates from the fact that the internal luminescence quantum efficiency q, or rather the original transition rates Γ_r and Γ_{nr}, are defined in the homogeneous

emissive material. Additionally, the absolute value of the dipole moment, which is normally not characterized, is not required for optical simulations due to such a normalization. The emitted power density $\mathrm{d}^2 P^{dipole}(\theta, \lambda, \mathbf{r_0}, \mathbf{p})/(\mathrm{d}\Omega\, \mathrm{d}\lambda)$ of a dipole emitter $\mathbf{p}$ at position $\mathbf{r_0}$ given by Eq. (3.11) corresponds to the angular and spectral emission

$$I^{dipole}(\theta, \lambda, \mathbf{r_0}, \mathbf{p}) \equiv \frac{\mathrm{d}^2 P^{dipole}(\theta, \lambda, \mathbf{r_0}, \mathbf{p})}{\mathrm{d}\Omega \cdot \mathrm{d}\lambda} \Big/ p_{tot}^{hom} \ , \tag{3.21}$$

which is now normalized to the totally irradiated power of the emitter in the homogeneous medium p_{tot}^{hom}. The far field angle θ is determined by the in-plane wavevector $k_\parallel$ given in Eq. (3.7). It is interrelated with the wavelength by the dispersion relation Eq. (3.4).

So far, the calculations have been performed for a single dipole with dipole moment $\mathbf{p}$ at a fixed position $\mathbf{r_0}$. Because the radiation pattern of an OLED is generated by an ensemble of emissive dipoles, appropriate ensemble distributions need to be regarded.

The orientation distribution of the dipole transition moments $g(\varphi)$

The first ensemble distribution to be considered is the orientation distribution of the dipole transition moments in the emissive layer. In this work, typical OLEDs with a homogeneous layered system are considered. In consequence of the device fabrication process, the dipole moments are isotropically oriented in the plane parallel to the layered system interfaces and a distinction between the different parallel dipole moments $p_x = \mathbf{e}_x\mathbf{p}$ and $p_y = \mathbf{e}_y\mathbf{p}$ is not required. Hence, only a non-isotropic distribution $g(\varphi)$ with respect to the internal angle φ between the dipole moment and the layered system normal (see Fig. 3.1(c)) has to be regarded. The dipole orientation distribution $g(\varphi)$ satisfies the normalization

$$\int_0^\pi g(\varphi) \cdot \sin\varphi \, \mathrm{d}\varphi = 1 \,. \tag{3.22}$$

The orientation angle φ is related to the direction of the dipole moment: $\cos\varphi = |\mathbf{e}_z\mathbf{p}|\,/|\mathbf{p}| = p_z/|\mathbf{p}|$. Thus, the fractions of all dipole moments that are parallel $p_\parallel$ and perpendicular $p_\perp$
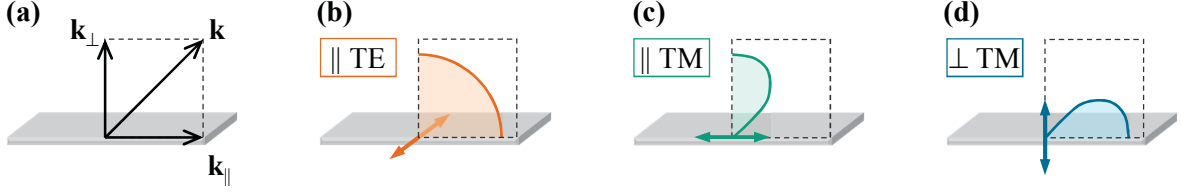
Figure 3.3. Three orthogonal dipoles. (a) The wavevector $\mathbf{k}$ (representing the direction of observation or measurement) and its two components in the directions parallel ($\mathbf{k}_\parallel$) and perpendicular ($\mathbf{k}_\perp$) to the interfaces of the layered system (gray plane). The orientations of the dipole transition moments (arrows) of the three orthogonal dipoles $\parallel$TE (b), $\parallel$TM (c), $\perp$TM (d), with respect to the layered system are also illustrated. The indicated schematics of the internal radiation patterns of the dipoles correspond to those in the homogeneous, infinite emissive material and are distorted in the presence of the interfaces of the layered system.

to the layered system interfaces are quantified by

$$p_\parallel = \frac{1}{|\mathbf{p}|^2} \int_0^\pi (p_x^2 + p_y^2) \cdot g(\varphi) \cdot \sin\varphi \, \mathrm{d}\varphi = \int_0^\pi g(\varphi) \cdot \sin^2\varphi \cdot \sin\varphi \, \mathrm{d}\varphi \,,$$

$$p_\perp = \frac{1}{|\mathbf{p}|^2} \int_0^\pi p_z^2 \cdot g(\varphi) \cdot \sin\varphi \, \mathrm{d}\varphi = \int_0^\pi g(\varphi) \cdot \cos^2\varphi \cdot \sin\varphi \, \mathrm{d}\varphi \,. \tag{3.23}$$

The normalization of $g(\varphi)$ in Eq. (3.22) ensures that $p_\parallel + p_\perp \equiv 1$. For the purpose of optical simulations, the classical emission pattern of an arbitrarily oriented dipole can be decomposed into contributions from three orthogonal dipoles ($\parallel$TE, $\parallel$TM, $\perp$TM) [39, 144, 145]:

$$I^{dipole}(\theta, \lambda, \mathbf{r_0}, \varphi) = \sin^2\varphi \left[I_{\parallel\mathrm{TE}}^{dipole}(\theta, \lambda, \mathbf{r_0}) + I_{\parallel\mathrm{TM}}^{dipole}(\theta, \lambda, \mathbf{r_0}) \right] + \cos^2\varphi \left[I_{\perp\mathrm{TM}}^{dipole}(\theta, \lambda, \mathbf{r_0}) \right] \,.$$
$$\tag{3.24}$$

These orthogonal dipoles are illustrated in Fig. 3.3. They are specified according to their orientation with respect to the interfaces of the layered system (parallel "$\parallel$", perpendicular "$\perp$") and the corresponding polarization of the emitted radiation ("TE", "TM"); the direction of measurement or observation is represented by the wavevector $\mathbf{k}$. Figure 3.3 indicates additionally the schematics of the internal radiation patterns of the dipoles in the homogeneous, infinite emissive material that are distorted in the presence of the interfaces of the layered system. Similar to the radiation pattern decomposition in Eq. (3.24) the total emitted power (from Eq. (3.12)) of an arbitrarily oriented dipole can be decomposed into the three orthogonal dipole contributions:

$$p_{tot}^{dipole}(\mathbf{r_0}, \varphi) = \sin^2\varphi \left[p_{\parallel\mathrm{TE},tot}^{dipole}(\mathbf{r_0}) + p_{\parallel\mathrm{TM},tot}^{dipole}(\mathbf{r_0}) \right] + \cos^2\varphi \left[p_{\perp\mathrm{TM},tot}^{dipole}(\mathbf{r_0}) \right] \,. \tag{3.25}$$

Equations (3.24) and (3.25) emphasize that the knowledge of the detailed orientation distribution $g(\varphi)$ is not necessary for optical simulations, but rather the fraction of parallel and perpendicular dipole moments (according to Eqs.(3.23)) that contribute to the radiation pattern. Hence, a common reasoning is that the emission from OLEDs is generated by two parallel dipoles ($\|$TE and $\|$TM) and, depending on the emissive material, a fraction of ν perpendicular dipole contributions ($\perp$TM), according to $p_\| : p_\perp = 2 : \nu$. If e.g. the dipoles are completely randomly distributed (corresponding to $g(\varphi) = 0.5$, the commonly assumed case in small-molecular materials), the radiation pattern is generated by one perpendicular dipole per two parallel dipoles: $p_\| = 2/3$ and $p_\perp = 1/3$, or $p_\| : p_\perp = 2 : 1$. Materials with a purely parallel emitter orientation yield $p_\| : p_\perp = 2 : 0$. Note that these considerations are valid only if the normalization of $g(\varphi)$ according to Eq. (3.22) is ensured subsequently.

The spatial distribution of the dipoles $N(z)$

The next ensemble distribution to be discussed is the spatial distribution of the dipoles in the emissive layer. Provided that the charge carriers are well distributed across the observed OLED area, the system is electrically homogeneous in the x-y plane. Hence, the active sites are homogeneously distributed in the plane of the layered system interfaces. The spatial distribution of the dipoles simplifies to a one-dimensional function, the so-called 'profile of the emission zone' $N(z)$ that depends solely on the height z in the active layer. The integral of $N(z)$ is normalized to one: $\int N(z)\mathrm{d}z = 1$. As a consequence, the radiation pattern and totally emitted power according to Eqs. (3.24) and (3.25), respectively, simplify ($\mathbf{r_0} \to z$):

$$I^{dipole}(\theta, \lambda, \mathbf{r_0}, \varphi) \to I^{dipole}(\theta, \lambda, z, \varphi), \qquad p_{tot}^{dipole}(\mathbf{r_0}, \varphi) \to p_{tot}^{dipole}(z, \varphi). \qquad (3.26)$$

3.5 OLED radiation pattern and external device efficiency

In this section, the approach for the calculation of the electromagnetic fields emitted from a single dipole (derived in Sec. 3.2), the character of the spontaneous emission event (discussed in Sec. 3.3), and the emitter ensemble distributions (described in Sec. 3.4) are combined to formulate the radiation pattern of an OLED.

Similarly to Eq. (3.20), the relative emission rate Γ_{rel} provides a link between the classical description of a continuously oscillating dipole and the quantum world of the spontaneous emission event:

$$I(\theta, \lambda, z, \varphi) \propto \frac{1}{\Gamma_{rel}(q, z, \varphi)} I^{dipole}(\theta, \lambda, z, \varphi). \tag{3.27}$$

By this means, the influence of the cavity on the rate of emission, the so-called 'microcavity effect', is taken into account and the normalization of power emitted from the dipole in the layered system is ensured. The expression of the relative transition rate in Eq. (3.19) highlights: For the low-q limiting case ($q \to 0$), where non-radiative transitions dominate the depopulation of the excited state, no influence of the cavity on the emission rate is present and the emission in Eq. (3.27) is readily given by the classical emission $I^{dipole}(\theta, \lambda, z, \varphi)$. By contrast, when employing high-q emitters which is the desired case for OLED systems, cavity effects influence both, $I^{dipole}(\theta, \lambda, z, \varphi)$ and $\Gamma_{rel}(q, z, \varphi)$.

In real OLED devices the emissive material is treated as an ensemble of incoherent radiators as discussed above. Following Section 3.4, distributions in (i) emitter location z, (ii) dipole orientation φ, and (iii) wavelength dependent spectral intensity account for (i) the profile of the emission zone $N(z)$, (ii) the distribution of emitter orientation $g(\varphi)$, and (iii) the internal EL spectrum $S(\lambda) = (hc/\lambda) \cdot \hat{s}(\lambda)$, respectively. The internal spectrum takes the photon energy $\hbar\omega = hc/\lambda$ into account, where $h = 2\pi\hbar$ denotes the Planck constant. The integrals of all distributions are normalized to one: $\int N(z)\mathrm{d}z = 1$, $\int g(\varphi)\sin\varphi\mathrm{d}\varphi = 1$, and $\int \hat{s}(\lambda)\mathrm{d}\lambda = 1$. By this means, the integrated distribution weight yields a single emissive event in total and $\int S(\lambda)\mathrm{d}\lambda$ corresponds to the mean photon energy with respect to the spectral distribution $\hat{s}$. The emission pattern from the OLED layered system $I^{cav}(\theta, \lambda)$ is obtained by an incoherent superposition of all contributions:

$$
\begin{aligned}
I^{cav}(\theta, \lambda) &= S(\lambda) \int_z \int_\varphi N(z)g(\varphi) \frac{I^{dipole}(\theta, \lambda, z, \varphi)}{\Gamma_{rel}(q, z, \varphi)} \sin\varphi \, \mathrm{d}\varphi \, \mathrm{d}z \\
&= S(\lambda) \left\langle \frac{I^{dipole}(\theta, \lambda, z, \varphi)}{\Gamma_{rel}(q, z, \varphi)} \right\rangle_{\varphi, z}.
\end{aligned}
\tag{3.28}
$$

In principle, the emission spectrum $S(\lambda)$ has to be taken into account for the calculation of the relative transition rate $\Gamma_{rel}(q, z, \varphi)$ used in Eq. (3.28). By this means, $\Gamma_{rel}(q, z, \varphi)$

represents an integral over the spectrum. In the frame of this thesis, however, $\Gamma_{rel}(q, z, \varphi)$ is determined at the mean wavelength of the internal emission spectrum which leads to a very well approximation for typical OLED structures and moderate spectral widths. Thus, Eq. (3.28) will be continuously applied in the following. Furthermore it is worth noting that Eq. (3.28) supports different types of ensemble-averaging methods regarding the orientation of the dipole transition moment φ, where the particular character of the emissive species is accounted in the detailed calculation of $\Gamma_{rel}(q, z, \varphi)$ [144]. In this work, the orientation of the dipole transition moment φ is assumed to be fixed during the process of emission. However, applying different ensemble-averaging methods typically results in small quantitative differences only, which have no qualitative impact on the presented considerations.

On purpose, $I^{cav}(\theta, \lambda)$ in Eq. (3.28) includes only optical effects due to the layered system. Electrical phenomena, like charge carrier injection and recombination, are excluded from corresponding investigations. Hence, it is this quantity which should be considered for optical analyses. It is related to the experimentally accessible spectral radiance of a device $I(\theta, \lambda)$ by the formula:

$$I(\theta, \lambda) = (I_{inj}/e) \cdot \gamma \cdot \eta_{S/T} \cdot q \cdot I^{cav}(\theta, \lambda) \,. \tag{3.29}$$

This equation includes (i) the number of injected charge carriers (I_{inj}/e), where I_{inj} denotes the current applied to the device and e denotes the elementary charge. The other terms express that the emission is further limited by (ii) the probability of charge carrier recombination and subsequent exciton formation γ, and (iii) by the generation of excited singlet as well as triplet states according to spin statistics, where allowed and forbidden transitions are regarded by the singlet triplet factor $\eta_{S/T}$. Additionally, (iv) the internal luminescence quantum efficiency q of the emissive system enters the spectral radiance. The latter three factors (ii)-(iv) are discussed in detail in some more detail Chapter 2.

The fraction of photons emitted from a device with respect to the infinite emissive material is given by an integration of the spectral and angular radiation pattern:

$$\eta_{out}^{cav} = 2\pi \int_{\lambda} \int_{\theta} \frac{I^{cav}(\theta, \lambda)}{hc/\lambda} \sin\theta \, d\theta \, d\lambda \,. \tag{3.30}$$

It yields a measure of how the number of emitted photons is influenced by the presence of the

layered system. It defines the overall device efficiency, represented by the well known external quantum efficiency that gives the number of emitted photons per injected charges:

$$\text{EQE} = \gamma \cdot \eta_{S/T} \cdot \left\langle q_{eff} \cdot \eta_{out}^{class} \right\rangle_{\varphi,z} = \gamma \cdot \eta_{S/T} \cdot q \cdot \eta_{out}^{cav}. \tag{3.31}$$

The middle term of Eq. (3.31) is known from Sec. 2.2 and is well established: In any microcavity the luminescence quantum efficiency of an excited state is system dependent due to near field effects ($q \rightarrow q_{eff}$, discussed broadly in Sec. 3.3). Furthermore, only a fraction of the internally generated light can leave the structure. This is taken into account by the classical outcoupling factor η_{out}^{class} that corresponds to the number of photons emitted from the layered system with respect to the number of photons generated inside the cavity. In this notation, however, q_{eff} accounts for the variation of the emissive rate due to the surrounding layered system according to Eq. (3.17), and the outcoupling factor η_{out}^{class} is calculated by classical theory given in Sec. 3.2. Thus, both quantities, q_{eff} and η_{out}^{class}, depend on the exact emitter position z in the system as well as on the emitter orientation φ, a fact which is often disregarded. In order to transform q_{eff} to an emissive system specific parameter, the internal luminescence quantum efficiency q is introduced into Eq. (3.31) on the right hand side. This gains the important advantage that the material dependent quantities ($\gamma, \eta_{S/T}, q$) are separated from the layered system specific effects (η_{out}^{cav}).

Chapter 4

Strategies to access the *active* emitter properties

In recent years, the characterization of OLED emitter properties by optical analysis of radiation patterns of OLEDs in electrical operation has been established as an *in situ* investigation method. Most studies analyze the spectral emission of conventional devices and leave an important issue open to debate: Does the investigated fraction of the OLED radiation pattern actually hold sufficient information about the internal feature of interest?

In order to pursue this question systematically, the simulated emission from a simplified bottom emitting OLED stack is discussed in this chapter. Starting from very basic considerations of the internal dipole emission process that have been compiled in the previous chapter, it is exploited that the distance between the emissive sites and the metal cathode is most crucial to the overall optical device behavior. Furthermore, the potential of polarization resolved analyses to separate the contributions from differently oriented emitters is considered. A macroscopic glass-hemisphere is frequently attached to the OLED substrate in order to observe an extended fraction of the internal emission pattern. Since this increases the complexity of the experiments considerably, it is worth to review its advantages in comparison to conventional analyses of the far field pattern in air.

Finally, a general routine is proposed that shall allow to determine the internal features of particular interest with greatest accuracy and in a manner almost independent of the other *active* properties of the emissive material.

4.1   Model layered system

The considerations in this chapter are illustrated by monochromatic analyses ($\lambda = 550\,\text{nm}$) of the artificial OLED system shown in Fig. 4.1. In fact, it is a simplified duplicate of typical bottom emitting devices as sketched in Fig. 2.2. Conventional OLED substrates are about $1\,\text{mm}$ thick and have refractive indices around $n = 1.5$. An ITO layer of about $100\,\text{nm}$ thickness is typically utilized as transparent anode and is covered by a HTL. The anode-sided part of the OLED stack has a minor impact on the basic effects addressed in this chapter. Thus, the HTL thickness is set to $60\,\text{nm}$, corresponding approximately to maximized radiation into air. An ETL performs as the optical spacer between the emissive sites and the opaque metal cathode of, in this case, silver. The optical properties of silver were taken from Ref. [146]. The organic materials and ITO utilized in conventional OLED systems have refractive indices around $n = 1.8$ at $\lambda = 550\,\text{nm}$ accompanied by negligible absorption [14, 34, 37].

All in all, the proposed model layered system consists of some ITO/organic ($n = 1.8$) on glass ($n = 1.5$) capped with opaque silver. The location of the emissive sites is assumed as a delta distribution with a fixed distance of $160\,\text{nm}$ to the substrate interface and a variable distance d to the silver mirror. Although this artificial configuration is pretty simple, it adequately represents most real OLED systems for the considerations addressed. It is apparently very similar to bottom emitting structures based on small-molecule materials, where charge carrier injection and blocking layers have refractive indices around $n = 1.8$ as well, and the emissive sites are well confined within the thin emissive layer (EML) of typically $10\,\text{nm}$ thickness. Top emitting OLEDs could be described by inverting the whole structure without the
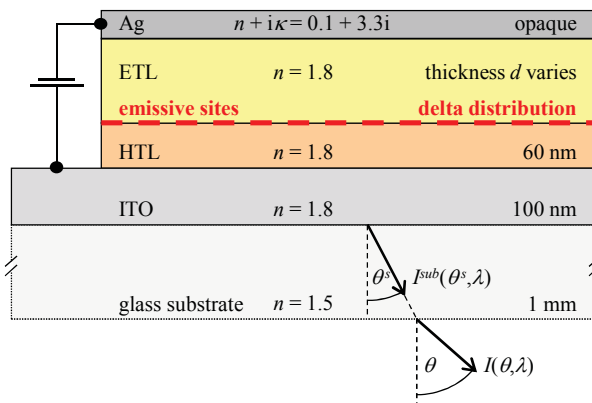
Figure 4.1. Model layered system. A simplified OLED system is used for the present considerations. The experimentally accessible spectral radiance $I(\theta, \lambda)$ is indicated. Attaching an index-matched, macroscopic glass-hemisphere or -prism to the substrate enables for an investigation of the substrate radiation pattern $I^{sub}(\theta^s, \lambda)$.

substrate and exchanging the ITO layer by a thin ($\approx 20\,\text{nm}$) metal layer [125]. However, in such a system the distance between the emissive sites and the semi-transparent metal has to be carefully adjusted as well, in order to observe the effects addressed later in this chapter. Typical polymeric OLEDs have a combined emissive and electron transport layer and a rather broad emission zone $N(z)$ of several ten to around $100\,\text{nm}$ [112]. Since the overall emission pattern is a superposition of all patterns from discrete emitter positions (see Eq. (3.28)), it is meaningful to divide the origin of this emission into single sheets for the purpose of optical analyses [125, 129, 147]. Furthermore, polymeric OLEDs can exhibit a confined emission zone at the anode-sided interface of the EML if the charge transport inside the emissive material is electron dominated [26]. Consequently, this case is included by an association of the real polymeric EML with a combination of ETL and emissive sites in the model system. In summary, the proposed model system matches most real OLED systems well enough to describe the experimental aspects addressed in this chapter. Furthermore the conciseness of the following arguments will benefit from the simplicity of this model system.

A glass-hemisphere or -prism is frequently attached to the OLED substrate to cancel the total internal reflection at the substrate-air interface [27, 28, 126, 148]. By this means, the radiance in the OLED substrate $I^{sub}(\theta^s, \lambda)$, where θ^s denotes the propagation angle in the substrate with respect to the system normal, is accessed and an extended fraction of the internally generated angular radiation pattern is investigated. However, it considerably increases the difficulty of experiments when a glass-hemisphere is attached to the OLED substrate using an index-matched oil because the OLED has to be placed precisely with respect to the center of the hemisphere, and the hemisphere should be much larger than the OLED area in order to obtain meaningful radiation patterns. Moreover, further parameters are introduced to the simulations since the refractive indices of the index-matching oil and the glass-prism material have to be considered. The following analyses are conducted for both cases, i.e. the emission pattern in air, $I^{air}(\theta, \lambda) = I^{cav,air}(\theta, \lambda)$, and in the substrate, $I^{sub}(\theta^s, \lambda) = I^{cav,sub}(\theta^s, \lambda)$, according to Eq. (3.28), in order to evaluate the real benefit of hemisphere measurements for radiation pattern analyses.

4.2   Dipole emission basics and the emitter-cathode distance

As pointed out by Eq. (3.24) and illustrated in Fig. 3.3, the radiation pattern of an arbitrarily oriented emissive dipole moment can be decomposed into contributions from three orthogonal dipoles ($\parallel$TE, $\parallel$TM, $\perp$TM). Parallel dipole moments contribute to both TE and TM polarized radiation, whereas perpendicular moments emit TM polarized radiation only. To elaborate the differences of these three orthogonal dipoles in some more detail, their contributions to the OLED far field are discussed individually in the following.

It is well known, that the emitter interacts with its reflected field from the mirror like metal cathode. Consequently, the distance between the emissive sites and the metal cathode mainly determines the interference conditions at the position of the emissive sites, and varying the emitter-cathode distance imposes the most pronounced effects onto the optical device properties. In result, the emitter-cathode distance is most crucial to enhance or suppress certain dipole contributions to the far field of the device.

In order to present the following reasoning independently of the particular refractive index n of the materials and wavelength λ of emission, the normalized emitter-cathode distance

$$k \cdot d = 2\pi \cdot n/\lambda \cdot d \tag{4.1}$$

is introduced by simply scaling the emitter-cathode distance d with the magnitude of the wavevector k. The product $k{\cdot}d$ represents a phase distance between the emitter and the metal cathode. There are three outstanding emitter-cathode distances for the following considerations, and the respective conversion of a real ETL thickness in the model layered system is: $d_1 = 70\,\text{nm} : k{\cdot}d_1 \approx \pi/2; \;\; d_2 = 135\,\text{nm} : k{\cdot}d_2 \approx \pi; \;\; d_3 = 220\,\text{nm} : k{\cdot}d_3 \approx 3/2\pi.$

As a measure of the far field contribution, the radiant flux in air (i.e. emitted intensity into air integrated over all emission angles $\Phi = 2\pi \cdot \int I^{air}(\theta, 550\,\text{nm}) \sin\theta \mathrm{d}\theta$) at $\lambda = 550\,\text{nm}$ of the three orthogonal dipoles embedded in the model device is calculated as a function of the normalized emitter-cathode distance and depicted in Fig. 4.2. Evidently, the emission from parallel and perpendicular emitters experience opposite interference conditions. This might be surprising at first because one might expect that the difference in phase shift of
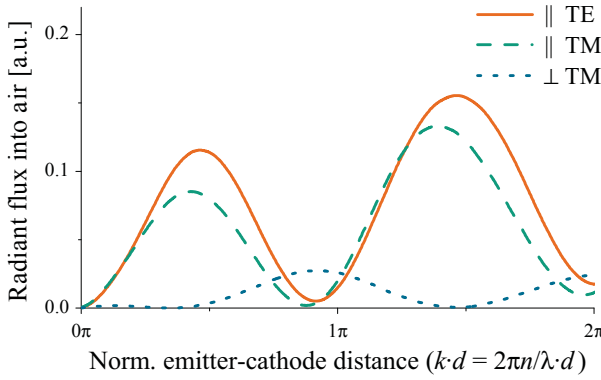
Figure 4.2. Opposite interference conditions for parallel and perpendicular dipoles. As a measure for the contribution to the OLED radiation pattern, the calculated radiant flux in air at $\lambda = 550\,\mathrm{nm}$ is shown as a function of the normalized emitter–cathode distance $k{\cdot}d$ for the three single dipoles ∥TE (orange, line), ∥TM (green, dashed), and ⊥TM (blue, dotted) embedded in the OLED stack depicted in Fig. 4.1.

approximately π (at moderate emission angles) upon reflection of TE and TM polarized light at the cathode results in a different interference behavior for TE and TM radiation. However, the typical character of dipole emission has to be taken into account as well (see e.g. Ref. [145]): the interference behavior additionally depends on the initial phase relation of the relevant electromagnetic fields emitted by the dipoles in the backward direction toward the cathode and the forward direction toward the OLED substrate. The forward and backward emitted electric TE fields of a parallel oriented dipole (∥TE) oscillate in phase initially. In case of the magnetic TM fields, there is a π phase difference for a parallel emitter (∥TM), but an in-phase-behavior for perpendicularly oriented dipoles (⊥TM) [145].[a] Combining both effects, (i) the phase difference due to cathode reflection and (ii) the initial phase relation of the emitted fields, results in a similar interference behavior for the TE and the TM waves of parallel dipoles (∥TE, ∥TM), but the interference effects of the radiation from perpendicularly oriented emitters (⊥TM) are shifted by π. This π phase shift corresponds to a discrepancy in the emitter-cathode distance of a quarter wavelength $1/4{\cdot}\lambda/n$ (n is the refractive index of the medium separating the emissive sites from the cathode) which is equivalent to $k{\cdot}d \approx \pi/2$. Thus, at emitter-cathode distances where parallel emitters experience constructive interference, destructive interference emerges for perpendicularly oriented emitters and vice versa. Constructive interference of parallel dipoles is expected at emitter-cathode distances of $1/4{\cdot}\lambda/n$, $3/4{\cdot}\lambda/n$, ..., equivalent to $k{\cdot}d \approx \pi/2$, $k{\cdot}d \approx 3/2\pi$, ... Constructive interference of perpendicular dipoles occurs at emitter-cathode distances of $2/4{\cdot}\lambda/n$, $4/4{\cdot}\lambda/n$, ..., equivalent

---

[a]This behavior corresponds to the change of signs in Eqs. (17) and (18) of Ref. [128].

to $kd \approx \pi$, $kd \approx 2\pi$, ...   The rigorous numerical simulation in Fig. 4.2 predicts slightly displaced positions of interference maxima and minima as the imperfect cathode mirror induces a non-ideal phase shift. Although the considerations above are strictly valid only for single, small emission angles θ, only minor deviations occur when the radiant flux is analyzed.

Two major effects need to be pointed out when the different contributions from the three orthogonal dipoles are discussed to highlight the relevance of the orientation of the emissive sites in OLEDs: First, perpendicularly oriented dipoles emit most power in the direction parallel to the interfaces (see Fig. 3.3(d)) and not in the desired perpendicular direction toward the outside medium air. Second, different interference conditions with the surrounding multilayer system apply to the fields of the three basic orthogonal dipoles, as can be clearly seen from Fig. 4.2. As a consequence of both effects, the orientation of the emissive sites in the light-emitting material has a major impact on the device performance and overall efficiency - a fact which is well-known [32, 34, 35, 126, 129]. Most common and optimized OLED stacks are designed to enhance the emission of parallel dipoles, as this allows extracting most power to the outside medium air (see Fig. 4.2 for $kd \approx \pi/2$, or $kd \approx 3\pi/2$). Unfortunately, this optimized stack architecture traps almost all light generated by perpendicularly oriented dipoles inside the layered system or the substrate glass. As a result, the optical outcoupling efficiency for emitters with exclusively parallel orientation is about 50% larger than for isotropic oriented emitters [19, 34, 36]. Within this context Fig. 4.2 illustrates the typical misery for light-emitting materials with isotropic emitter orientation: at the position for optimal outcoupling almost all light from perpendicular dipoles is trapped inside the OLED stack.

4.3 Optical reverse simulation: The inverse outcoupling problem

The relations for the radiation pattern and EQE from an electrically operating OLED given by Eqs. (3.29) and (3.31), respectively, illustrate the fundamental reason why optical reverse simulation from external device measures is not straight forward: externally measured device outputs are necessarily an average of all single emitter contributions. It is almost impossible to estimate features of the internal dipole radiation by starting from EQE measurements

because the EQE is an integral over all angular and spectral components. Furthermore, the other factors in the EQE-Eq. (3.31) have to be known precisely in order to deduce meaningful results from the measured EQE. By contrast, angular, spectral, and polarization resolved measurements of the radiation pattern are more likely to allow for conclusions about the emissive sites properties. However, in order to separate the contributions from emitters with distinct locations or orientations in the optical far field (see Eq. (3.29)), two ideas are fundamental:

(i) According to Eq. (3.24), parallel dipoles emit TE and TM polarized radiation, whereas perpendicular dipoles contribute to TM polarized radiation only. Hence, polarization dependent measurements should allow for a separation of the contributions from parallel and perpendicular dipoles. By analyzing the TE polarized radiation pattern, investigations of the internal EL spectrum $S(\lambda)$ and the emission zone $N(z)$ are performed independently of the dipole orientation. Keeping the internal spectrum and emission zone fixed while analyzing the TM polarized radiation pattern, the emitter orientation distribution $g(\varphi)$ remains the only unknown parameter that is adjusted to match TM experiment and simulation.

(ii) As discussed broadly in the previous section, the emitter-cathode distance mainly determines the interference conditions at the position of the emissive sites and is most crucial to enhance or suppress certain dipole contributions to the OLED far field. Thus, the device architecture should be well adapted in order to optically enhance the feature of interest.

Solving the inverse outcoupling problem is based on performing a least-squares fit to the measured angle, wavelength, and polarization dependent radiance of a device. In order to circumvent the complexity of absolute measurements and the consideration of absolute factors in Eq. (3.29), a non-absolute reverse simulation based on Eq. (3.28) is usually performed. A number of discrete emitter positions z within the emissive layer are assumed, each with identical internal spectrum $S(\lambda)$ and orientation distribution $g(\varphi)$. Some investigations are conducted considering a single dipole at a single position within the emissive layer [126, 127]. Other studies take an extended emission zone $N(z)$ into account, assuming a parametric distribution deduced from electrical considerations [25–28] with numerically reasonable emitter position discretizations (e.g. $\Delta z \approx 10\,\mathrm{nm}$ [26], or $\Delta z \approx 20\,\mathrm{nm}$ [27]). However, applying a para-

metric distribution is intrinsically limited since the resultant emission zone is always within the frame of the electrical model. Consequently, the derived results are as open to debate as is the underlying electrical model. This is especially relevant for investigations considering the emission from positions very close to interfaces [26, 27]. Unfortunately, optical reverse simulations based on a large number of discrete emitter positions without assuming a distribution fail because the radiation patterns of the emissive sites are not sufficiently distinct and not linearly independent. Regarding the orientation of the emissive sites, it is impossible to measure the detailed orientation distribution $g(\varphi)$, but rather the fraction of parallel and perpendicular dipole contributions $(p_{||} : p_{\perp})$ that generate the radiation pattern. This has been shown by experiments using both optical [19] and electrical [34] excitation. However, Eq. (3.24) shows that the knowledge of the detailed emitter orientation distribution is not necessary for optical evaluations and information about the relative contributions from parallel and perpendicular dipoles is sufficient.

4.4   TE polarization: Internal spectrum and emission zone

As mentioned in Sec. 4.2, only TE polarized radiation should be considered if an investigation of the internal EL spectrum and/or emission zone is intended. To illustrate the following reasoning, Fig. 4.3(a) depicts the dependence of the radiant flux ($\Phi_{\mathrm{TE}} = 2\pi \cdot \int I_{\mathrm{TE}}^{air}(\theta, 550\,\mathrm{nm}) \sin\theta \mathrm{d}\theta$) of TE polarized radiation from the model device into air on the normalized emitter-cathode distance $k \cdot d$. In this context the radiant flux from a device can be interpreted as a measure of the optical efficiency of an OLED. An optically optimized device architecture ensures that the emissive sites are placed at a distance of $k \cdot d \approx \pi/2$ to the cathode (corresponding to a quarter wavelength distance $1/4 \cdot \lambda/n$, shifted additionally by the non-ideal phase change upon reflection at the non-ideal cathode mirror). The emission into air is enhanced at this distance due to constructive interference of light emitted directly into the substrate direction with that reflected at the metal cathode. By contrast, for an normalized ETL thickness of about $k \cdot d \approx \pi$ (corresponding to about a half wavelength distance $2/4 \cdot \lambda/n$) radiation from the emissive sites experiences destructive interference and emission into air is

suppressed. A comparison of Figs. 4.2 and 4.3(a) reveals that the behavior of the TE radiant flux (Φ_{TE}) represents the characteristics of the overall radiant flux ($\Phi = \Phi_{\text{TE}} + \Phi_{\|\text{TM}} + \Phi_{\perp\text{TM}}$) from a device as well.

The shape of the angular radiation pattern is related to the interference conditions at the position of the emissive site. Figs. 4.3(b)–(k) show the TE angular radiation pattern in air $I_{\text{TE}}^{air}(\theta, 550\,\text{nm})$ according to Eq. (3.28) for some representative normalized emitter-cathode distances. The characteristics shown in Figs. 4.3(b)–(d) and Figs. 4.3(h)–(k) correspond to emissive sites located at values of emitter–cathode distance in the first and second maximum
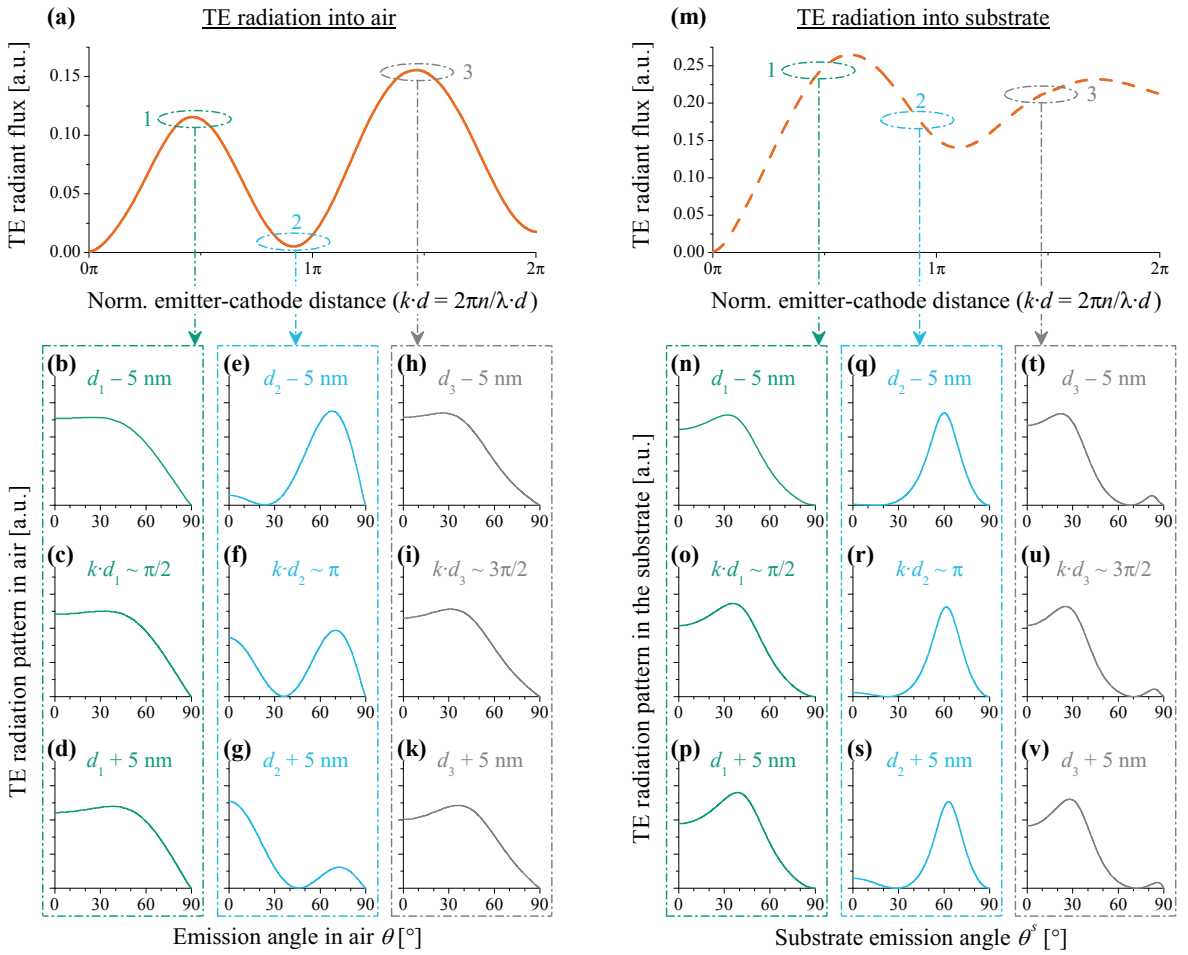
Figure 4.3. TE radiant flux and radiation patterns. As a measure for the optical efficiency of the model OLED stack, the TE polarized radiant flux is shown versus the normalized emitter-cathode distance for radiation into air (a) and radiation into the substrate (m). From the point of optical analyses, there are three outstanding emitter positions, labeled 1, 2, and 3. For these positions, TE polarized angular radiation patterns according to Eq. (3.28) are shown for emission into air (left) and into the substrate (right). Position 1 corresponds to the first maximum of radiation in air [(b)–(d) and (n)–(p), $k \cdot d_1 \approx \pi/2$], position 2 yields minimal radiation in air [(e)–(g) and (q)–(s), $k \cdot d_2 \approx \pi$], and position 3 corresponds to the second maximum of radiation in air [(h)–(k) and (t)–(v), $k \cdot d_3 \approx 3/2\pi$].

of the TE polarized radiant flux into air, respectively. The angular pattern is nearly Lambertian like for these cases and all characteristics are very similar to each other due to the constructive interference conditions for moderate emission angles around these positions. By contrast, the angular characteristics of emissive sites around the minimum of the TE polarized radiant flux into air, as shown in Figs. 4.3(e)–(g), are significantly modulated and deviate strongly from a Lambertian emission pattern. Furthermore, the absolute emission intensity is considerably reduced due to destructive interference. Surprisingly, it can be seen that the angular characteristics vary considerably for emitters displaced by just a few nanometer. For emissive sites at a distance $k \cdot d \approx \pi$ to the cathode, there is destructive interference for emission into oblique angles of $\theta \approx 40°$. This condition shifts significantly toward smaller or larger emission angles upon moving the emissive sites closer to or farther from the cathode, causing a variation of the balance between radiation into normal or oblique angles.

The right part of Fig. 4.3 illustrates a similar characteristics as the left part, but for emission inside the OLED substrate. The normalized TE polarized substrate radiant flux shown in Fig. 4.3(m) consists of an extended fraction of the internally generated angular radiation pattern and is less modulated than the radiant flux into air. All angular patterns from emitter–cathode distances corresponding to maxima of the normalized TE polarized radiant flux into air (Figs. 4.3(n)–(p) and Figs. 4.3(t)–(v)) exhibit enhanced radiation into larger substrate angles, yielding a higher flux due to solid angle considerations. Their characteristics deviate from a Lambertian emission significantly and are very similar to each other. The angular characteristics in the substrate of emissive sites around the minimum of normalized TE polarized radiant flux into air (Figs. 4.3(q)–(s)) are again significantly modulated, destructive interference for substrate emission angles around 20..30° is found, and the absolute emission intensity is reduced. However, compared to the data in air shown in Figs. 4.3(e)–(g), there is much less effect of the emitter–cathode distance on the radiation pattern shape.[b]

---

[b]Notice that the same emitter-cathode distances (d_1, d_2, d_3) are used for discussing the TE and TM radiation in air and in the substrate, although these stacks do not exactly correspond to maximum or minimum radiation into the substrate. However, the consideration of the two emitter-cathode distances that yield optically optimized devices (d_1, d_3) is essential for the line of reasoning in this chapter. The same d_2 is assumed for simplicity. The two parameters that are introduced in the following ($V_\theta(d)$, $V_\perp(d)$) cover all reasonable d and reveal that this approach does not influence the overall statement of this chapter.

In order to quantify the variation of angular radiation pattern due to the emitter–cathode distance, the parameter $V_\theta(d)$ is introduced:

$$V_\theta(d) = \int\limits_{\theta=0°}^{\theta=90°} \left| \frac{I_{\mathrm{TE},d_-}^{air}(\theta, 550\,\mathrm{nm})}{\Phi_{\mathrm{TE},d_-}} - \frac{I_{\mathrm{TE},d}^{air}(\theta, 550\,\mathrm{nm})}{\Phi_{\mathrm{TE},d}} \right| \cdot \frac{\sin\theta\,\mathrm{d}\theta}{\Delta d} \,. \tag{4.2}$$

In this relation, $I_{\mathrm{TE},d}^{air}(\theta, 550\,\mathrm{nm})$ denotes TE polarized radiation emitted into the angle θ in air from an emissive site at a distance d to the cathode, and d_- denotes the next distance closer to the cathode, depending on the discretization $\Delta d = |d - d_-|$ of the emitter–cathode distances chosen for the calculation of $V_\theta(d)$. In Eq. (4.2), normalization with respect to the radiant flux at the particular distance to the cathode is important to distinguish the desired relative variation of the shape of the angular pattern from a variation of the absolute emitted power. In other words, all radiation patterns are normalized to the same area in terms of solid angle and only the relative variation of the characteristics is considered. By this means, $V_\theta(d)$ provides a measure of how distinguishable are the radiation pattern shapes of two neighboring positions, d_- and d, in the device. Replacing $I_{\mathrm{TE},d}^{air}(\theta, 550\,\mathrm{nm})$ by the TE radiation pattern in the substrate as a function of the substrate angle $I_{\mathrm{TE},d}^{sub}(\theta^s, 550\,\mathrm{nm})$ and normalizing to the radiant flux in the substrate in Eq. (4.2) yields the corresponding variation of angular radiation pattern in the substrate as a function of emitter–cathode distance.

The angular radiation pattern variation $V_\theta(d)$ versus the normalized emitter–cathode distance is shown in Fig. 4.4 for both radiation in air and in the substrate. It can be seen that $V_\theta(d)$ is low for almost all emitter–cathode distances, including the case of optically optimized devices, apart from emission from around the radiant flux minimum. The latter feature can be explained by the destructive interference conditions for emission into certain oblique angles,
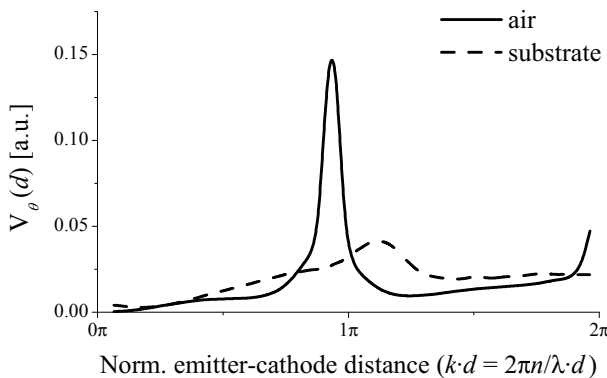
Figure 4.4. Sensitivity to the emission origin. The variation of the TE polarized angular radiation pattern in air and in the substrate according to Eq. (4.2) is plotted. Maxima of $V_\theta(d)$ correspond to minima of optical outcoupling (compare Fig. 4.3(a) and Fig. 4.3(m)). Placing the emissive sites around $k \cdot d \approx \pi$ enables for an accurate determination of the exact emission origin.

which considerably modulates the angular radiation pattern, as discussed above. Surprisingly, analyzing the substrate radiation pattern yields only little more information compared to the emission in air. The radiation in air exhibits even better contrast to the exact emission origin if the emissive sites are placed around the radiant flux minimum. This might be surprising at first because one might expect the substrate radiation, containing an extended fraction of the OLED-internal radiation pattern, to yield much more information than the radiation into air. However, the suggested approach is based on observing radiation pattern changes and the pattern variations are maximized at small emission angles. This sensitive interval is expanded in air because the transition from the substrate into air restricts the observed fraction of the OLED-internal radiation pattern. Hence, the qualitative impression from the shape of the angular emission patterns in Figs. 4.3(b)–(k) and Figs. 4.3(n)–(v) is confirmed by the quantitative measure $V_\theta(d)$.

Of course, when designing an experiment to measure the internal EL spectrum of a material, relatively weak changes of the interference conditions are desired in order to minimize the influence of the actual position of the emissive sites $N(z)$ on the result. Consequently, the emissive sites should be placed around a maximum for optical outcoupling which additionally ensures a high outcoupling intensity.

By contrast, the radiation pattern is most sensitive to the position of the emissive sites at the minimum of optical output where destructive interference conditions apply. The following experiment is considered as an example: the emission layer of a small-molecular device has a width of 10 nm and the exact emission origin is of particular interest. In this case, the ETL thickness should be adjusted in order to match the efficiency minimum in air (corresponding to $k{\cdot}d \approx \pi$). Even analyzing the angular radiation pattern in air in a purely qualitative manner provides information about how the emission zone is balanced. If the angular emission pattern is larger at larger angles, the origin of the emission is at the cathode side of the EML, whereas a larger emission in the perpendicular direction provides evidence for anode-sided emission (compare Figs. 4.3(e)–(g)). Of course, quantitative reverse simulations using an extended spectral range promise even more accurate results.

These monochromatic considerations can be extended in a straightforward manner to the case of real emissive materials for OLEDs with a spectral width of typically about $50-100\,\mathrm{nm}$. The layered stack should be designed to match the desired criterion for maximum or minimum outcoupling at the mean wavelength of the spectrum under investigation. As can be seen from Fig. 4.3, the interference conditions do not change significantly with emitter–cathode distance around the quarter wavelength distance at $k{\cdot}d \approx \pi/2$, which implies that the interference conditions do not change significantly with wavelength as well. Consequently, for emitters around the optical maximum the determination of the internal spectrum is almost independent of the actual position of the emissive sites, as discussed above. One would expect to gather more information about the profile of the emission zone if the investigated spectral range is extended. However, the condition for good contrast on the emitter position, corresponding to the $V_\theta(d)$ maximum in Fig. 4.4, is wavelength dependent. This is potentially a positive feature when analyzing extended emission zones but yields no benefit when investigating rather confined emission zones. For the latter case, a certain spectral width relaxes the requirement to meet the specified emitter-cathode distance d with a very high accuracy because it is the product $k{\cdot}d$ that has to be adjusted.

Measuring the emission profile of broad emission zones, which are typical for polymeric OLEDs, is problematic. It is essentially critical for such experiments that positions with good extraction efficiency and thus large far field contribution possess low sensitivity to the emission origin, as indicated by a small $V_\theta(d)$. By contrast, positions featuring a high sensitivity to the emission origin have only weak contributions to the far field. In other words, radiation from positions around the efficiency minimum might not be visible in the far field of the OLED because it is much weaker than the brighter signal from positions around the efficiency optimum. Although there have been extensive studies on measurements of the profile of the emission zone in polymeric OLEDs recently, this general and problematic issue has not been considered yet [26–28, 31].

4.5   TM polarization: Dipole orientation

In order to sense perpendicular dipoles in the TM polarized optical far field of an OLED, their contributions to the radiation pattern must be sufficiently large compared to the TM polarized contributions arising from parallel dipoles. As a measure of the far field contribution, the radiant flux in air $\Phi_{\mathrm{TM}}^{air} = 2\pi \cdot \int I_{\mathrm{TM}}^{air}(\theta, 550\,\mathrm{nm}) \sin\theta \mathrm{d}\theta$ and in the substrate $\Phi_{\mathrm{TM}}^{sub} = 2\pi \cdot \int I_{\mathrm{TM}}^{sub}(\theta^s, 550\,\mathrm{nm}) \sin\theta^s \mathrm{d}\theta^s$ at $\lambda = 550\,\mathrm{nm}$ of the two TM dipoles embedded in the model OLED stack is calculated as a function of the normalized emitter-cathode distance (see Fig. 4.5(a) and Fig. 4.5(e), respectively). The emission from parallel and perpendicular emissive sites is governed by opposite interference conditions as discussed in detail in Sec. 4.2. This feature is utilized for investigations of the dipole emitter orientation.

In order to quantify the visibility of perpendicular emitters in the TM polarized OLED radiation pattern, the parameter $\mathrm{V}_\perp(d)$ is introduced:

$$\mathrm{V}_\perp(d) = \frac{\Phi_{\perp\mathrm{TM},d}}{\Phi_{\|\mathrm{TM},d} + \Phi_{\perp\mathrm{TM},d}}, \tag{4.3}$$

giving the contrast of $\perp$TM dipole contributions in the overall TM polarized emission in air
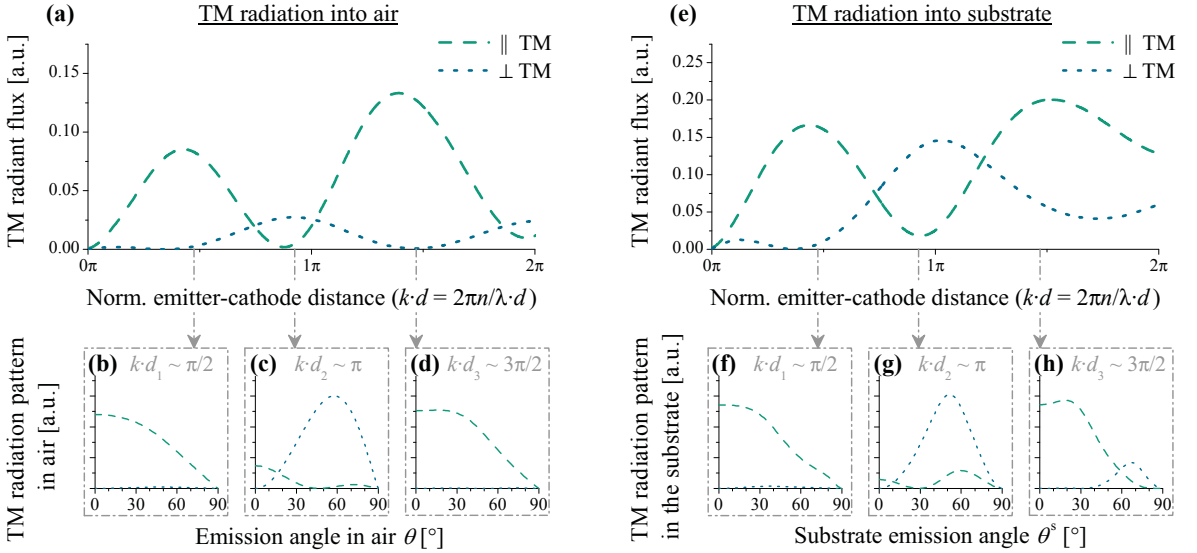
Figure 4.5. TM radiant flux and radiation patterns. The TM polarized radiant flux of the two TM dipoles ∥TM (green, dashed), and ⊥TM (blue, dotted) versus the normalized emitter-cathode distance is shown for radiation in air (a) and in the substrate (e). For the three outstanding emitter positions, TM polarized angular radiation patterns according to Eq. (3.28) are shown for emission into air (left) and into the substrate (right), split into the contributions from ∥TM (green, dashed) and ⊥TM (blue, dotted) dipoles.
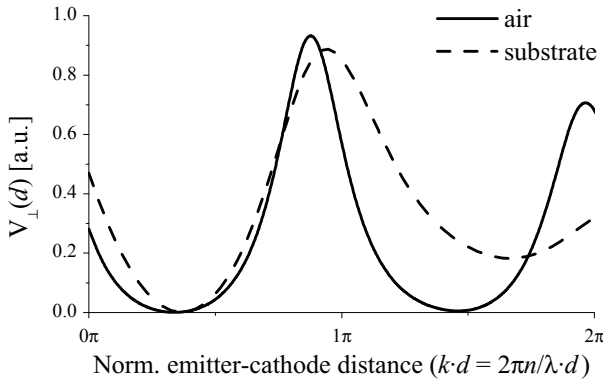
Figure 4.6. Sensitivity to the emitter orientation. The contribution of radiation from perpendicular dipoles ($\perp$TM) to the overall TM polarized far field ($\|$TM + $\perp$TM) in air and in the substrate, respectively, according to Eq. (4.3). Maxima of $V_\perp(d)$ correspond to minima of optical outcoupling (compare Fig. 4.2). Thus, positions around the optical minimum at $k \cdot d \approx \pi$ are favorable for a measurement of the dipole orientation.

and in the substrate, respectively. The dependence of the $V_\perp(d)$-parameter on the emitter–cathode distance is plotted in Fig. 4.6. Positions close to the cathode are not suitable for any optical experiment because they suffer from strong coupling to the surface plasmon mode and the overall outcoupling efficiency is very weak. However, the interference conditions around the optical maximum enhance radiation from parallel dipoles and suppress light from perpendicular emitters (see Fig. 4.5(b) and Fig. 4.5(f), as well as Fig. 4.6 for $k \cdot d \approx \pi/2$). Consequently, the distribution of the dipole moment orientation is almost impossible to obtain using standard, efficient OLED geometries which are optimized for maximum emission because almost all light generated by perpendicularly oriented emitters is trapped inside the OLED stack. This argument holds for both, the air and substrate emission. By contrast, changing the emitter–cathode distance to the minimum of optical outcoupling yields a large far field contribution from perpendicular dipole moments accompanied by weaker outcoupling of the radiation from parallel dipoles (see Fig. 4.5(c) and Fig. 4.5(g), as well as Fig. 4.6 for $k \cdot d \approx \pi$). This is the desired case for an emitter orientation analysis. Again, this rule is valid for both, air and substrate emission. Measurements using a glass-hemisphere will yield a little more information for very large emitter–cathode distances only (see Fig. 4.5(d) and Fig. 4.5(h), as well as Fig. 4.6 for $k \cdot d > \pi$), but offer no benefits compared to an emitter orientation investigation based on the radiation pattern in air utilizing a well adapted OLED layered system.

4.6   Internal luminescence quantum efficiency q

According to Eqs. (3.28) and (3.29), the optically relevant factors to the spectral radiance $I(\theta, \lambda)$ of a device are (i) the q-value, (ii) the relative lifetime of the excited states $\tau_{rel} = 1/\Gamma_{rel}$, and (iii) the radiation pattern of a continuously oscillating dipole $I^{dipole}(\theta, \lambda)$:

$$I(\theta, \lambda) \propto q \cdot \frac{1}{\Gamma_{rel}} \cdot I^{dipole}(\theta, \lambda) . \qquad (4.4)$$

Placing an emitter at a certain distance to the cathode, the relative transition rate of the excited states (Γ_{rel}) depends on all modes of the surrounding layered system. The q-value determines how much the relative transition rate is affected (see Eq. (3.19)). This has significant impact on the performance of the layered system $I^{cav} \propto I^{dipole}/\Gamma_{rel}$. Moreover, the q-value is a multiplier to the real emitted power $I \propto q \cdot I^{cav}$.

To understand the role of the q-value in OLEDs, the forward radiance from the model layered system $I(0°, 550\,\mathrm{nm})$ is discussed in detail in the following. Figure 4.7 shows several relevant measures of an emitter placed in the model layered system as a function of the emitter distance to the metal cathode for some representative q-values. The behavior of the relative lifetime (τ_{rel}), i.e. the inverse transition rate ($1/\Gamma_{rel}$), of this emitter is depicted in the upper plot. The middle plot illustrates the effects due to the layered system ($I^{cav} \propto I^{dipole}/\Gamma_{rel}$), and the lower plot shows the corresponding emitted radiance in forward direction. For the sake of conciseness, only parallel emitters are considered. The case of low-q emitters ($q \rightarrow 0$) in Fig. 4.7(a) clearly exhibits no influence of the layered system on the relative transition rate ($q \rightarrow 0$ in Eq. (3.19) and the transition rate is identical to the rate in the homogeneous emissive medium). In Fig. 4.7(b), the radiation pattern of low-q emitters is readily given by the classical radiation pattern and the modulation is again due to internal interference effects. Of course, the overall emission from a low-q emitter is pretty weak (see Fig. 4.7(c) for $q \rightarrow 0$). By contrast, the surrounding stack has a large influence on the relative rate for high-q emitters ($q \rightarrow 1$). The relative lifetime is very low close to the cathode and the relative rate is considerably enhanced. This is due to the fact that the emitter couples very efficiently to the surface plasmon propagating at the metal-ETL interface. As one result, the contribution

to the far field radiation for high-q emitters is decreased in Fig. 4.7(b) because more energy is lost into the plasmon compared to the low-q limiting case. Of course, the overall emitted power in Fig. 4.7(c) is larger the larger the q-value is.

These considerations suggest that the emitter's q-value could be determined via the modified $\Gamma_{rel}(q)$ by somehow shifting the emissive sites through the device because the emitter-cathode distance induces the most pronounced effects on the interference conditions in the layered system. Based on a quantitative efficiency comparison of a series of OLEDs, each of which comprises a different emitter-cathode separation, the change in the radiative rate due to the modified surrounding layered system can be scanned to enable a determination of q by optical means [37]. It should be noted that the given reasoning is not limited to the forward radiance from OLEDs. In the same manner, e.g. the radiant flux, the EQE, or the radiance into another emission angle (with or without a particular polarization state) from several devices could be quantitatively compared. By this means, the proposed approach is similar to basic experiments on the fluorescence lifetime of molecular ensembles near interfaces [144].
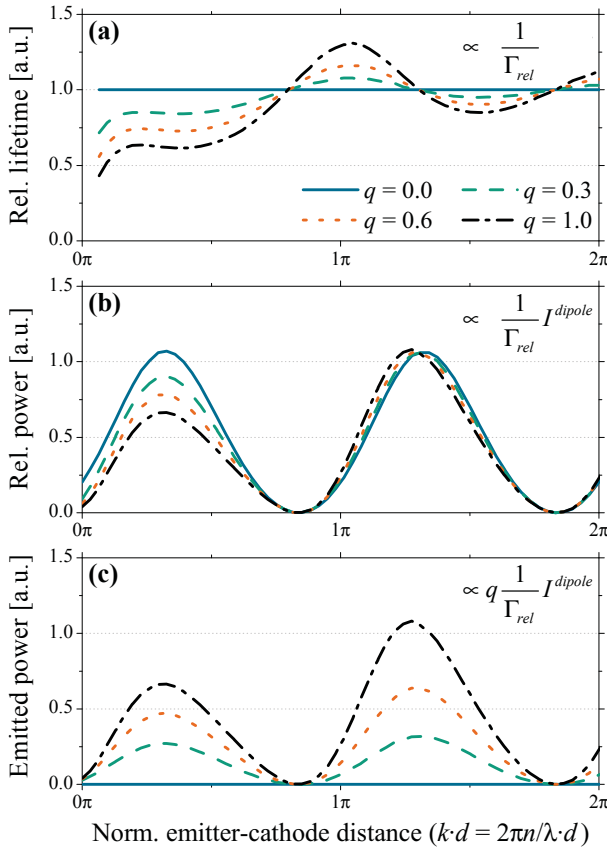
Figure 4.7. The role of q in OLEDs. Several relevant measures of an emitter placed in the model layered system as a function of the distance of the emitter to the metal cathode are shown for some representative q-values: (a) the relative lifetime, (b) the effect due to the layered system, and (c) the emitted radiance. For the sake of conciseness, only the emission in forward direction is regarded: (b) $I^{cav}(0°, 550\,\text{nm})$, and (c) $I(0°, 550\,\text{nm})$. For low-q emitters ($q \to 0$), the lifetime is identical to the one in the infinite medium ($\tau_{rel} \to 1$), the effect due to the layered system is readily given by the dipole pattern ($I^{cav} \to I^{dipole}$), and the overall emission is very low ($I \to 0$). By contrast, high-q emitters ($q \to 1$) close to the metal cathode couple very efficiently to the surface plasmon. Thus, the radiative rate is enhanced and the emission from the layered system is reduced. Of course, the overall emission is enhanced. (For the sake of conciseness, only parallel emitters are considered.)

Some further aspects should be noted: The suggested approach is valid only if the electrical device characteristics as well as the *active* optical properties of the emissive system remain unchanged upon varying the emitter-cathode distance. Otherwise, a quantitative comparison of different devices from an optical point-of-view is debatable. Furthermore, there is a certain interrelation between the q-value and the other *active* emitter properties: e.g. the different relative transition rates for parallel and perpendicular emitters have to be considered for the emitter orientation determination. However, the position of a $V_\perp(d)$-maximum corresponds to emitter-cathode distances where the transition rate is nearly unchanged compared to the homogeneous medium (compare Fig. 4.6 and Fig. 4.7). Hence, the expected effect is of minor importance. In the end, the quantitative analyses of *active* emitter properties is an iterative procedure anyway, as discussed in detail in Sec. 5.4.

4.7   A routine for a complete *in situ* emitter characterization

In summary, general strategies for accessing OLED emitter properties by radiation pattern analyses have been proposed in this chapter. Taking advantage of the fact that perpendicular dipoles contribute to TM polarized light emission only, one should analyze TE polarized radiation only if an investigation of the internal spectrum or the emission zone is intended. Provided the OLED layered stack is designed carefully, subsequently analyzing TM polarized radiation yields information about the orientation of the emissive sites.

The outlined considerations clearly demonstrate that optically optimized OLED stacks are rather useless if an investigation of the emission zone or the emitter orientation is intended - no matter of an attached glass-hemisphere. Radiation patterns in air should be investigated and well-adapted devices have to be utilized in order to enable an accurate determination of the *active* optical properties of emissive materials used in OLEDs. In this context, the distance from the emissive sites to the metal cathode plays a decisive role as it strongly affects interference conditions in the device.

Consider the emitter–cathode distance to illustrate the optical efficiency of a device. Then, placing the emissive sites at a position

(i) around the emission maximum ($k \cdot d \approx \pi/2$) and analyzing TE polarized radiation allows a determination of the internal EL spectrum $S(\lambda)$,

(ii) around the emission minimum ($k \cdot d \approx \pi$) and analyzing TE polarized radiation allows an accurate determination of the emission zone $N(z)$, and

(iii) around the emission minimum ($k \cdot d \approx \pi$) and analyzing TM polarized radiation allows a determination of the orientation of the emissive dipoles $g(\varphi)$ or rather $(p_\parallel : p_\perp)$,

almost independent of the other active optical properties, respectively. Once the other *active* emitter properties are known,

(iv) a quantitative comparison of emission from several devices with different emitter-cathode distances allows a conclusion to internal luminescence quantum efficiency q.

(v) Repeating the analysis is important to ensure no q-dependent effect in the steps (i)-(iii) and vice versa as discussed in detail in the following chapter.

Chapter 5

Methods and investigated OLEDs

Before proceeding to a detailed discussion of the experimental data and results in Chapter 6, the radiation pattern measurement setup is introduced in the following. Furthermore, the fabrication and stack architecture of the OLED systems under study is explained briefly. The investigated OLEDs comprise three emitter materials: a blue spiro-fluorene polymer as well as a green $(Ir(ppy)_3)$ and a red $(Ir(MDQ)_2(acac))$ small-molecular material. Finally, the characterization of the passive layered systems is touched and the data analysis and fitting methods are outlined.

5.1 Radiation pattern measurement

During all measurements, the OLEDs are driven at a constant current density using a constant current source (GS610, Yokogawa). By this means, the number of charge carriers in the devices is controlled and stabilized. Unless stated differently, the applied current densities are $j = 2.5 \, \mathrm{mA/cm^2}$ for the polymeric and $j = 50 \, \mathrm{mA/cm^2}$ for the small-molecular OLEDs. The OLEDs are mounted in a specially built fixture, to ensure a good and reproducible contacting. Furthermore, side or scattered substrate emission is blocked by the fixture. All measurements are performed at room temperature.

The polarized angular radiation patterns are recorded utilizing a rotational stage (CR1/M-Z7E, Thorlabs) where the OLED is mounted. The optical detection system consists of a wire grid linear polarizer (NT47-101, Edmund Optics) with attached achromatic waveplate
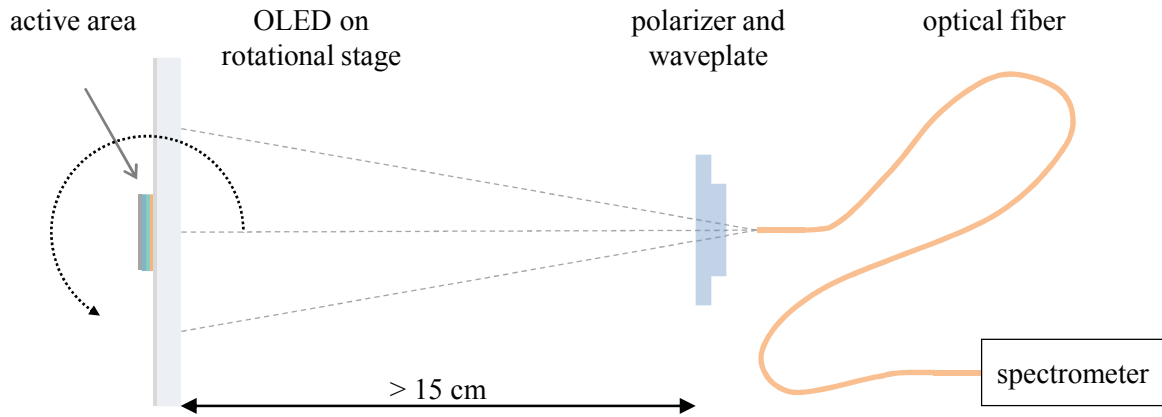
Figure 5.1. Radiation pattern measurement setup. Schematic illustration (not to scale) of the experimental setup to measure the OLED radiation patterns. The OLED is mounted on a rotational stage. The detection system consists of a polarizer, a retarder, and a fiber coupled spectrometer. The retarder converts the linearly polarized light into circularly polarized radiation in order to avoid any polarization dependent effects in the optical fiber.

(AQWP05M-630, Thorlabs), combined with a calibrated, fiber coupled spectrometer (SD2000, Ocean Optics). Fig. 5.1 shows a sketch of the experimental setup. Two linear stages are additionally mounted on the rotational stage to enable a precise adjustment of the OLED in the rotational axis. The spectrometer is used in combination with an optical fiber (M17L02, Thorlabs) with numerical aperture of 0.22 and $200\,\mu$m core diameter. Thus, the wavelength resolution of the spectrometer is $\Delta\lambda < 5\,$nm and an intensity uncertainty below 2 percent is achieved. The circular emissive area of all OLEDs under investigation is smaller than $5\,$mm in diameter. The distance of the optical fiber to the OLED is larger than $15\,$cm during all measurements to ensure an angular resolution of $\Delta\theta < 1°$.

Due to the rotational symmetry of OLEDs, the emission pattern from OLEDs is symmetric to the forward direction of $0°$: $I(-\theta) = I(\theta)$. This symmetry is exploited to check the quality of the experimental adjustment with respect to the angular measurement. If the OLED is e.g. not perfectly adjusted in the rotational axis of the rotational stage, the measured radiation pattern will not exhibit sufficient symmetry with respect to $0°$. On the other hand, if the acquired radiation pattern for $-90° \leq \theta \leq 0°$ and $0° \leq \theta \leq 90°$ are identical, a perfect adjustment with respect to the rotational axis is proven. Finally, the data for positive and negative emission angles are averaged, simultaneously improving the signal-to-noise ratio.

5.2   OLED systems and emitters under study

5.2.1   Polymer: Blue fluorescent emitter

A sketch of the layered system of the polymeric OLEDs (PLEDs) used is depicted in Fig. 5.2(a). In order to fabricate multilayer PLEDs, the approach of crosslinkable materials was utilized [67]. The organic layers poly(3,4–ethylenedioxythiophene) poly(styrenesulfonate) (PEDOT:PSS, 35 nm), hole transport layer (HTL, 24 nm), and blue light-emitting conjugated polymer (LEP, introduced as emitter B1 in Ref. [26]) were deposited by spin-coating on commercial glass substrates coated with indium tin oxide (ITO, 129 nm). The HTL was crosslinked to immobilize the material prior to the deposition of the LEP [67]. All stacks were capped by a thermally evaporated cathode of barium (Ba, 4 nm) and silver (Ag, 200 nm). In total, 14 devices with varying LEP thicknesses (10 nm-264 nm) with an active area of $1/12.5\,\mathrm{cm}^2 = 8\,\mathrm{mm}^2$ were fabricated by Dr. Malte C. Gather (Prof. Klaus Meerholz Group, Univ. Cologne).

The emissive material is electron dominated and a confined emission zone at the anode-sided interface of the LEP is expected [26], indicated by the color gradient in Fig. 5.2(a). Consequently, changing the LEP thickness corresponds to a variation of emitter-cathode distance in this case. Fig. 5.2(b) shows the system's parameters $V_\theta(d)$ and $V_\perp(d)$ for the sensitivity to the emission zone and emitter orientation, respectively. These parameters are calculated at the mean wavelength of the emitter spectrum $\lambda = 480\,\mathrm{nm}$ [26] and for emitters that are located exactly at the HTL-LEP interface for simplicity.
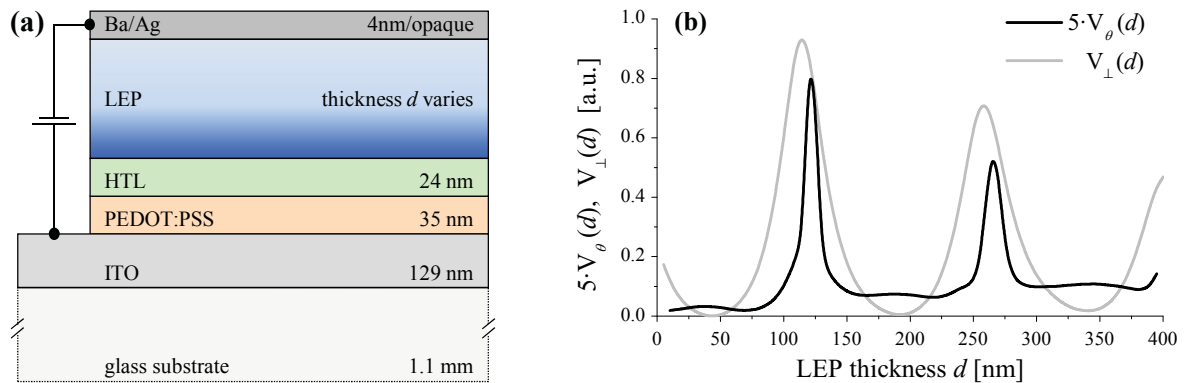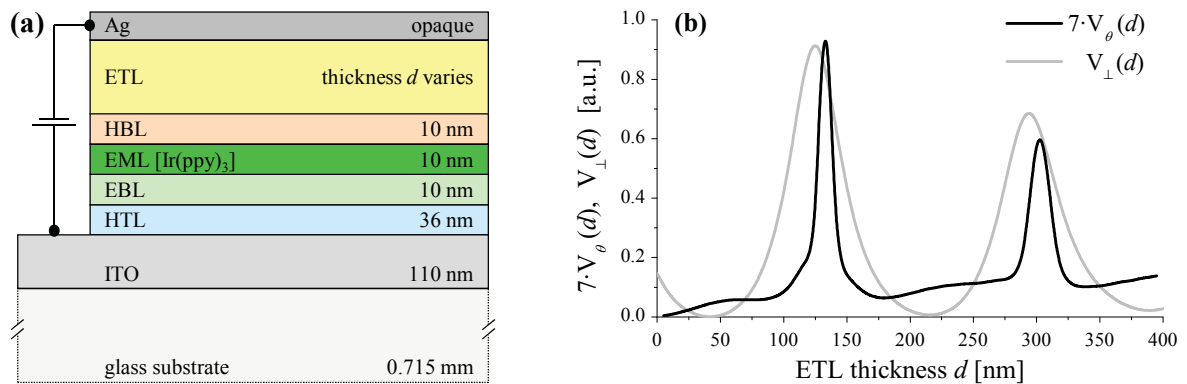

Figure 5.2. Blue PLED: Stack architecture and sensitivity parameters. The layered system of the blue PLEDs is shown (a). Sensitivity parameters $V_\theta(d)$ and $V_\perp(d)$ were calculated (b). An LEP thickness of $d \approx 125\,\mathrm{nm}$ enables a precise determination of emission zone and emitter orientation.

5.2.2   Small molecule: Green and red phosphorescent emitters

The phosphorescent OLED (PhOLED) samples, comprising several individually addressable circular pixels of $1/25\,\mathrm{cm}^2 = 4\,\mathrm{mm}^2$ area, were prepared at OSRAM Opto Semiconductors GmbH, Regensburg, by thermal evaporation of organic materials onto commercial ITO coated substrates. The layered structure was fabricated using standard evaporation techniques at a base pressure of $10^{-7}\,\mathrm{mbar}$ and an evaporation rate of $0.05\,\mathrm{nm/s}$. Doped ETL and HTL were used to improve electron and hole transport, respectively, introducing the dopant by co-evaporation. This technique was also used for incorporating the emitters into the respective EML matrix. Electron-blocking layers (EBL) and hole-blocking layers (HBL) were utilized to confine the charge carrier recombination zone within the EML. After cathode evaporation all devices were encapsulated with a glass lid containing a getter.

Figure 5.3(a) shows the stack architecture of the green PhOLEDs. The EML consists of an electron conductive host and the green phosphorescent dye fac-tris(2-phenyl-pyridine)-iridium(III) (Ir(ppy)$_3$. It is known as an efficient phosphorescent OLED emitter material (see e.g. Ref. [73]) and its chemical structure is given in Fig. 2.3(c)). A series of 8 devices with ETL thicknesses between about $30\,\mathrm{nm}$ and $300\,\mathrm{nm}$ was fabricated. Figure 5.3(b) shows the parameters $V_\theta(d)$ and $V_\perp(d)$ for the sensitivity to the emission zone and emitter orientation, respectively, for this particular OLED system, calculated at the mean wavelength $\lambda = 550\,\mathrm{nm}$ of the Ir(ppy)$_3$ emission spectrum [149] and assuming a constant spatial distribution of the
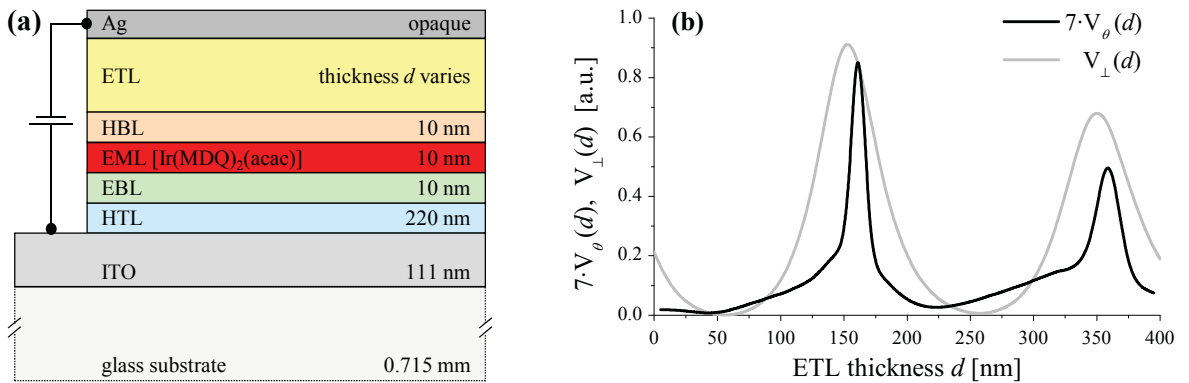

Figure 5.3. Green PhOLED: Stack architecture and sensitivity parameters. The layered system of the green PhOLEDs containing Ir(ppy)$_3$ as emissive material is shown (a). The sensitivity parameters $V_\theta(d)$ and $V_\perp(d)$ were calculated (b), indicating that an ETL thickness of $d \approx 130\,\mathrm{nm}$ enables a precise determination of emission zone and emitter orientation in Ir(ppy)$_3$.

emissive sites for simplicity. It can be seen that an ETL thickness of $d \approx 130\,\text{nm}$ allows for an accurate determination of both, the emission zone and emitter orientation in Ir(ppy)$_3$.

The stack architecture of the red emitting PhOLEDs is depicted in Fig. 5.4(a). The EML consists of the red triplet-emitting material iridium(III)bis(2-methyldibenzo-[f,h]quinoxaline)-(acetylacetonate) (Ir(MDQ)$_2$(acac), 8 wt%) in a N,N'-bis(naphthalen-1-yl)-N,N'-bis(phenyl)-2,2'-dimethylbenzidine (α-NPD) matrix. Ir(MDQ)$_2$(acac) is a typical emitter in today's high efficiency OLEDs and the mean wavelength of the emission spectrum is $\lambda = 630\,\text{nm}$ [11, 13]; its chemical structure is shown in Fig. 2.3(d). A series of 9 devices with ETL thicknesses between about 40 nm and 380 nm was fabricated. Figure 5.4(b) shows the parameters V$_\theta(d)$ and V$_\perp(d)$ for the sensitivity to the emission zone and emitter orientation, respectively, for this particular OLED system, assuming a constant spatial distribution of the emissive sites for simplicity. It can be seen that an ETL thickness of $d \approx 160\,\text{nm}$ allows for an accurate determination of both, the emission zone and emitter orientation in Ir(MDQ)$_2$(acac).

The current–voltage characteristics of all PhOLEDs were also investigated to ensure similar electrical behavior of the devices in spite of the different ETL thicknesses. Fortunately, the current-voltage curves revealed no significant difference between the devices with varying ETL thicknesses; a fact that is attributed to appropriate n-doping of the ETL [127]. As a favorable consequence, only optical effects need to be considered in forthcoming analyses, allowing a relative comparison of the performance of the devices from an optical point of view.

Figure 5.4. Red PhOLED: Stack architecture and sensitivity parameters. The layered system of the red PhOLEDs containing Ir(MDQ)$_2$(acac) as emissive material is shown (a). The sensitivity parameters V$_\theta(d)$ and V$_\perp(d)$ were calculated (b), indicating that an ETL thickness of $d \approx$ 160 nm enables a precise determination of emission zone and emitter orientation in Ir(MDQ)$_2$(acac).

5.3   Characterization of the passive layered systems

The prerequisite for any optical simulation of OLEDs is the knowledge of the *passive* optical properties of the layered system, i.e. the materials complex refractive indices and layer thicknesses. The complex refractive indices of all utilized thin film materials are measured by a dispersion-model-free approach utilizing reflection-transmission-spectroscopy of single supported films [15]. This technique is perfectly suited for organic thin film materials due to several reasons: The measured quantities reflection and transmission are easily accessible with common spectrophotometers (in this study: Lambda 900, Perkin Elmer). Furthermore, the need of assuming a more or less suitable and complex dispersion model is omitted because the calculation of the thin film material constants $n(\lambda)$ and $\kappa(\lambda)$ is carried out by direct inversion. The accuracy reached ($\Delta n \approx 10^{-2}, \Delta \kappa \approx 10^{-3}$) is in excellent agreement with the demands of thin film optical simulations. Due to the thickness of the supported film needed ($100\,\mathrm{nm} < d < 250\,\mathrm{nm}$), common preparation techniques can be applied without significant changes. A detailed discussion of the method can be found in Ref. [15]. By this means, all organic materials, ITO layers, and substrates are characterized (data not shown). The optical properties of the silver cathodes are taken from Ref. [146].

The approach to determine the layer thicknesses is different for the PLED and the PhOLED systems. For the POLED structures spincoated from solution, several additional reference stacks were fabricated, consisting of single- and multi-layer fragments of the OLED stack. These reference stacks are analyzed by profilometry as well as by reflection-transmission spectroscopy and the thickness of each layer is determined with an accuracy of $\pm 2\,\mathrm{nm}$ (data not shown). Regarding the evaporated PhOLED structures, the complete series was produced on one substrate for the green and red PhOLEDs, respectively, using one shadow mask for all layers except the ETL. For the deposition of the ETL, different shadow masks were used in order to realize different ETL thickness. Hence, it was ensured that the thickness of all layers in the stack apart from the ETL are identical for all devices of one series. The thickness of each layer is determined by analyzing device reflection spectra of all devices simultaneously and taking the specified thicknesses for the fabrication process into account (data not shown).

5.4 Data analysis and fitting methods

The radiation pattern of the OLEDs $I_{\text{TE,TM}}^{\text{meas}}(\theta, \lambda)$ is measured at a number of M_θ discrete angles ($0° \leq \theta \leq 90°$) and M_λ discrete wavelengths ($380\,\text{nm} \leq \lambda \leq 780\,\text{nm}$) for both polarization states TE and TM. As a first step, $I_{\text{TE,TM}}^{\text{meas}}(\theta, \lambda)$ is normalized with respect to the angle-averaged spectral TE polarized intensity observed at each wavelength:

$$\hat{I}_{\text{TE,TM}}^{\exp}(\theta, \lambda) = \frac{I_{\text{TE,TM}}^{\text{meas}}(\theta, \lambda)}{S_{\text{TE}}^{\text{meas}}(\lambda)}, \quad \text{with} \quad S_{\text{TE}}^{\text{meas}}(\lambda) = \frac{1}{M_\theta} \sum_{m=1}^{M_\theta} I_{\text{TE}}^{\text{meas}}(\theta_m, \lambda). \tag{5.1}$$

This normalization procedure conveniently eliminates the influence of the spectral magnitude of the particular emissive spectrum on any forthcoming analysis. However, it requires to limit the analysis to a spectral region where the emission from the device is sufficiently large. Otherwise the denominator in Eq. (5.1) becomes very small and the resultant insufficient signal-to-noise ratio frustrates a usable normalization.

For a given OLED system, the angular and spectral radiance $I^{dipole}(\theta, \lambda, z, \varphi)$ according to Eq. (3.21) is calculated for several discrete emitter positions z within the emissive layers. An emitter position discretization of $\Delta z = 4\,\text{nm}$ is chosen for simulations of the PLED structures with rather thick LEPs, whereas for the simulation of the PhOLEDs employing only $10\,\text{nm}$ thin EMLs, an emitter position discretization of $\Delta z = 2\,\text{nm}$ is applied.

With an initial guess for the emission zone $N(z)$ and a constant internal spectrum $S(\lambda) \equiv 1$, the TE polarized emission pattern from the OLED $I_{\text{TE}}^{cav}(\theta, \lambda)$ is calculated from Eq. (3.28) as a superposition of radiation pattern contributions from different discrete positions z. $I_{\text{TE}}^{cav}(\theta, \lambda)$ is normalized with respect to the angle-averaged spectral effect of the layered system

$$\hat{I}_{\text{TE}}^{\text{sim}}(\theta, \lambda) = \frac{I_{\text{TE}}^{cav}(\theta, \lambda)}{S_{\text{TE}}^{cav}(\lambda)}, \quad \text{with} \quad S_{\text{TE}}^{cav}(\lambda) = \frac{1}{M_\theta} \sum_{m=1}^{M_\theta} I_{\text{TE}}^{cav}(\theta_m, \lambda). \tag{5.2}$$

The real profile of the emission zone $N(z)$ is evaluated by minimizing the error function

$$(\text{RMS}_{\text{TE}})^2 = (\chi_{\text{TE}})^2 = \frac{1}{M_\theta \cdot M_\lambda} \sum_{m=1}^{M_\theta} \sum_{n=1}^{M_\lambda} \left(\hat{I}_{\text{TE}}^{\text{sim}}(\theta_m, \lambda_n) - \hat{I}_{\text{TE}}^{\exp}(\theta_m, \lambda_n) \right)^2. \tag{5.3}$$

Once the profile of the emission zone $N(z)$ is known, $I_{\text{TE}}^{cav}(\theta, \lambda)$ can be refined, and the internal EL spectrum of the emissive material is found in a straight-forward manner:

$$S(\lambda) = S_{\text{TE}}^{\text{meas}}(\lambda) / S_{\text{TE}}^{cav}(\lambda). \tag{5.4}$$

Subsequently, the normalization of the spectral distribution $\hat{s}(\lambda)$ according to Sec. 3.5 has to be ensured. By this means, the internal EL spectrum $S(\lambda)$ and the profile of the emission zone $N(z)$ are determined by analysis of measured and simulated TE polarized emission patterns. Both values are kept fixed for the analysis of TM polarized emission.

As a next step, the orientation of the emissive sites is evaluated from the TM polarized emission pattern from the OLED. As discussed in Sec. 4.3, it is impossible to measure the detailed orientation distribution $g(\varphi)$ but rather the fraction of parallel $p_\parallel$ and perpendicular $p_\perp$ dipole contributions generating the radiation pattern (see Eq. (3.24)). The absolute amount of parallel dipoles that contribute to the radiation pattern is known from the scaling of the TE analysis, and only the fraction of perpendicular moments is adjusted at this stage. The TM polarized emission pattern from the OLED $I_{TM}^{cav}(\theta, \lambda)$ is calculated according to Eq. (3.28), assuming fixed $S(\lambda)$ and $N(z)$ as found from the TE analysis. Again, $I_{TM}^{cav}(\theta, \lambda)$ is normalized, but still with respect to the TE angle-averaged spectral effect of the layered system $S_{TE}^{cav}(\lambda)$

$$\hat{I}_{TM}^{sim}(\theta, \lambda) = \frac{I_{TM}^{cav}(\theta, \lambda)}{S_{TE}^{cav}(\lambda)} . \tag{5.5}$$

Using $S_{TE}^{cav}(\lambda)$ again ensures a constant scaling factor between TE and TM polarized emission and at the same time a constant contribution of parallel dipoles. The contribution from perpendicular dipole moments $p_\perp$ is evaluated by minimizing the TM error function

$$(\text{RMS}_{TM})^2 = (\chi_{TM})^2 = \frac{1}{M_\theta \cdot M_\lambda} \sum_{m=1}^{M_\theta} \sum_{n=1}^{M_\lambda} \left(\hat{I}_{TM}^{sim}(\theta_m, \lambda_n) - \hat{I}_{TM}^{exp}(\theta_m, \lambda_n) \right)^2 . \tag{5.6}$$

By this means, the emitter orientation $g(\varphi)$ in the emissive material is determined by analysis of measured and simulated TM polarized OLED radiation patterns.

Knowing spectrum $S(\lambda)$, emission zone $N(z)$, and emitter orientation $g(\varphi)$ in the emissive material, the influence of the surrounding layered system on the emissive process (see Eq. (3.27)) due to the variation of the emission rate Γ_{rel} according to Eq. (3.19) can be evaluated by the optical simulation. A relative comparison of measured and calculated emission data (e.g. radiance at a certain angle and wavelength, or an integral measure like radiant flux, radiant intensity, or EQE) of a series of OLEDs with different emitter-cathode distances enables a determination of the q-value.

At this point it is worth noting that the determination of the *active* optical properties of an emissive material is necessarily an iterative process. First, emission zone, internal EL spectrum, and dipole orientation are determined by radiation pattern analyses assuming $q \rightarrow 0$ (or another reasonable guess) as an initial approximation. These first approximate values subsequently enter the simulation when the q-value is analyzed. Now, with the knowledge of an approximate q-value, the simulated radiation pattern according to Eq. (3.28) accounts for a modified excited state lifetime and more exact internal EL spectrum, emission zone, and emitter orientation are obtained. With these, the q-value is refined etc., resulting in an iterative procedure. Fortunately, the resultant values usually converge well below their respective confidence intervals within two or at most three iteration loops. For the sake of simplicity, only the final most accurate results are given in the following.

Finally it has to be noted that the introduced values $\hat{I}(\theta, \lambda)$, that are normalized with respect to the angle-averaged spectral intensity, are perfectly suitable for analysis purposes. Unfortunately, these values are little descriptive in the end. For the purpose of data display, $I_{\text{TE,TM}}^{\text{meas}}(\theta, \lambda)$ will be normalized to the largest measured intensity in the following:

$$I_{\text{TE,TM}}^{\text{exp}}(\theta, \lambda) = \frac{I_{\text{TE,TM}}^{\text{meas}}(\theta, \lambda)}{max(I_{\text{TE,TM}}^{\text{meas}}(\theta, \lambda))} \,, \tag{5.7}$$

ensuring a proper comparability of all 'experimental' radiation patterns $I_{\text{TE,TM}}^{\text{exp}}(\theta, \lambda)$. The emission pattern $I_{\text{TE,TM}}^{cav}(\theta, \lambda)$ is calculated according to Eq. (3.28), but assuming a constant spectrum; a proper spectral weighting of the 'simulated' radiation patterns $I_{\text{TE,TM}}^{\text{sim}}(\theta, \lambda)$ will be achieved by

$$I_{\text{TE,TM}}^{\text{sim}}(\theta, \lambda) = S_{\text{TE}}^{\text{meas}}(\lambda)/S_{\text{TE}}^{cav}(\lambda) \cdot I_{\text{TE,TM}}^{cav}(\theta, \lambda) \,, \tag{5.8}$$

where $S_{\text{TE}}^{\text{meas}}(\lambda)/S_{\text{TE}}^{cav}(\lambda)$ is used as a scaling factor that connects experiment and simulation, but solely for the purpose of plotting and presenting the data in a well-arranged manner.

Chapter 6

Experiments and discussion

Based on the concepts introduced in Chapter 4, a complete characterization of the *active* optical properties of all three OLED emitter materials (introduced in Section 5.2) is carried out from radiation patterns measured in air. In oder to avoid tedious repetitions, only some selected, representative, and meaningful experiments that yield noteworthy results will be discussed in detail in this chapter. Of specific interest is the experimental verification of the hypothesis that the OLED stack design is crucial to emitter characterization by radiation pattern analyses. Furthermore, the spatial distribution of the emissive sites in the $10\,\mathrm{nm}$ thin EML of the PhOLEDs and the presumably isotropic emitter orientation in the phosphorescent emissive materials $\mathrm{Ir(ppy)_3}$ and $\mathrm{Ir(MDQ)_2(acac)}$ are worth a closer look. A more precise investigation of the electron dominated current in the polymeric emissive material is desirable, as well as to gain some insight into the q-value of the emissive systems in electrical operation and its potential current density dependence. Finally, important findings concerning the emitter orientation will be discussed with special focus on their capability to improve the overall efficiency of OLEDs considerably.

In the following Chapter, all false color plots of the radiation patterns exhibit a logarithmic intensity scale to better visualize low intensity data. The RMS errors are calculated according to Eqs. (5.3) and (5.6). In contrast to some publications that show device emission patterns within a limited angular range only (see e.g. Ref. [27]), the full angular spectrum $0° \leq \theta \leq 90°$ of the radiation patterns will be analyzed because particularly oblique emission angles may contain valuable information.

6.1   The importance of well-adapted devices: Emission zone and dipole emitter orientation in Ir(ppy)$_3$ PhOLEDs

This section is intended to highlight the importance of a specific layered system design that is conceived in order to enhance the particular internal dipole feature of interest. For this purpose, two devices of the green Ir(ppy)$_3$ PhOLED series (see Fig. 5.3) with two different stack architectures or rather emitter-cathode distances are analyzed. The first device represents a conventional OLED structure that is optimized for maximum performance: device [A], comprising an ETL thickness of $d = 59$ nm that corresponds to $k \cdot d \approx \pi/2$. The second device operates at a weak overall efficiency and is supposed to be well-adapted to accurately measure emission zone and emitter orientation in Ir(ppy)$_3$: device [B], with $d = 125$ nm and $k \cdot d \approx \pi$. In the following analyses, the wavelength-region 480 nm $\leq \lambda \leq 700$ nm of significant Ir(ppy)$_3$ emission is used to evaluate the RMS errors according to Eqs. (5.3) and (5.6).
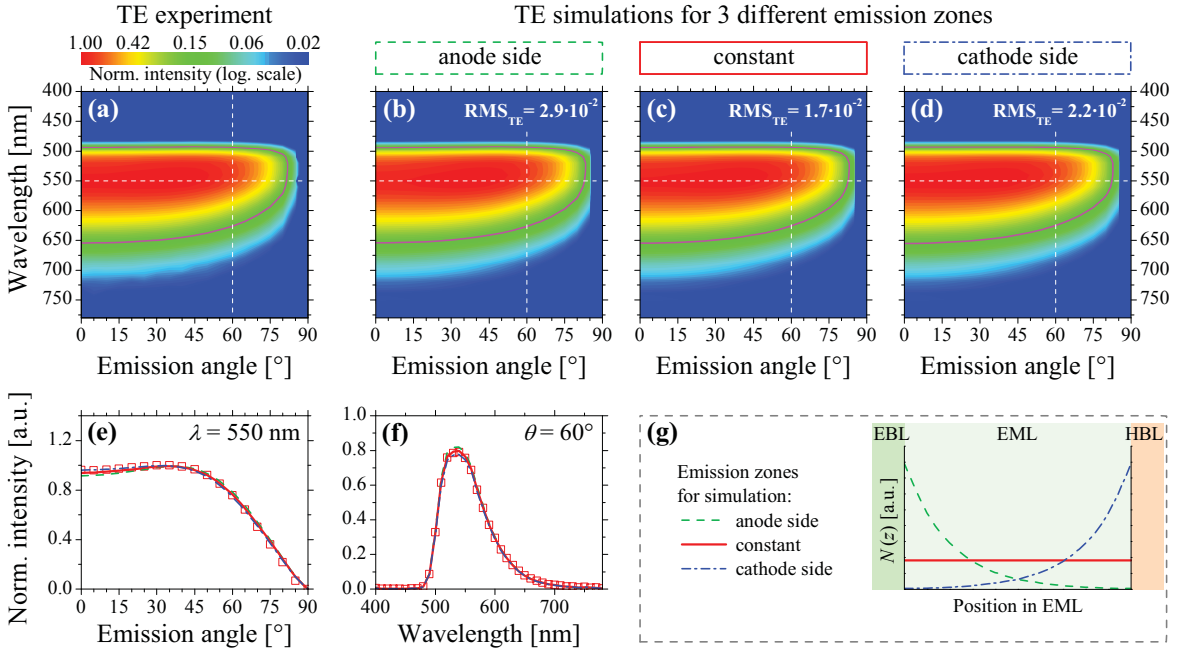
Figure 6.1. Emission zone in Ir(ppy)$_3$ PhOLED [A]. Experimental and theoretical TE polarized emission pattern of the Ir(ppy)$_3$ PhOLED [A] comprising 59 nm ETL. False color plots (a)-(d) exhibit a logarithmic intensity scale, the value 0.15 is accentuated by a magenta line, cross sections at $\theta = 60°$ and $\lambda = 550$ nm are indicated by white dashed lines. Cross section data for $\lambda = 550$ nm (e) and $\theta = 60°$ (f) are plotted: experimental data (squares) and theoretical predictions (lines). Simulation results for three different emission zones (g) are shown: anode-sided [(b), green dashed line in (e)-(f)], constant [(c), red solid line in (e)-(f)], and cathode-sided [(d), blue dash-dotted line in (e)-(f)]. All assumptions yield a good match to the experimental data, indicated by the similar and low RMS$_{\text{TE}}$.

Figure 6.1 shows the measured and calculated TE radiation patterns of the Ir(ppy)$_3$ PhOLED [A]. As expected from a device in the first optical optimum in terms of emitter-cathode distance, the radiation pattern is rather Lambertian-like. Three very different emission zones, sketched in Fig. 6.1(g), are assumed for the simulation: a constant emission zone and two exponential emission zones with 2 nm 1/e-width centered at the EML-EBL interface (anode side) and EML-HBL interface (cathode side), respectively. The corresponding formula are (i) constant: $N(z) = 1/10\,\text{nm}$; (ii) anode side: $N(z) = (1/2\,\text{nm})\exp[-z/2\,\text{nm}]$; (iii) cathode side: $N(z) = (1/2\,\text{nm})\exp[-(10\,\text{nm} - z)/2\,\text{nm}]$. All three emission zones yield an excellent match between measured and simulated radiation pattern, as indicated by the low RMS deviation. In other words, this device structure is insensitive to the exact emission origin and is, thus, unsuitable for measuring the emission zone.

By contrast, the device structure of the Ir(ppy)$_3$ PhOLED [B] is perfectly adapted for an emission zone measurement. According to Fig. 6.2, the angular and spectral location of
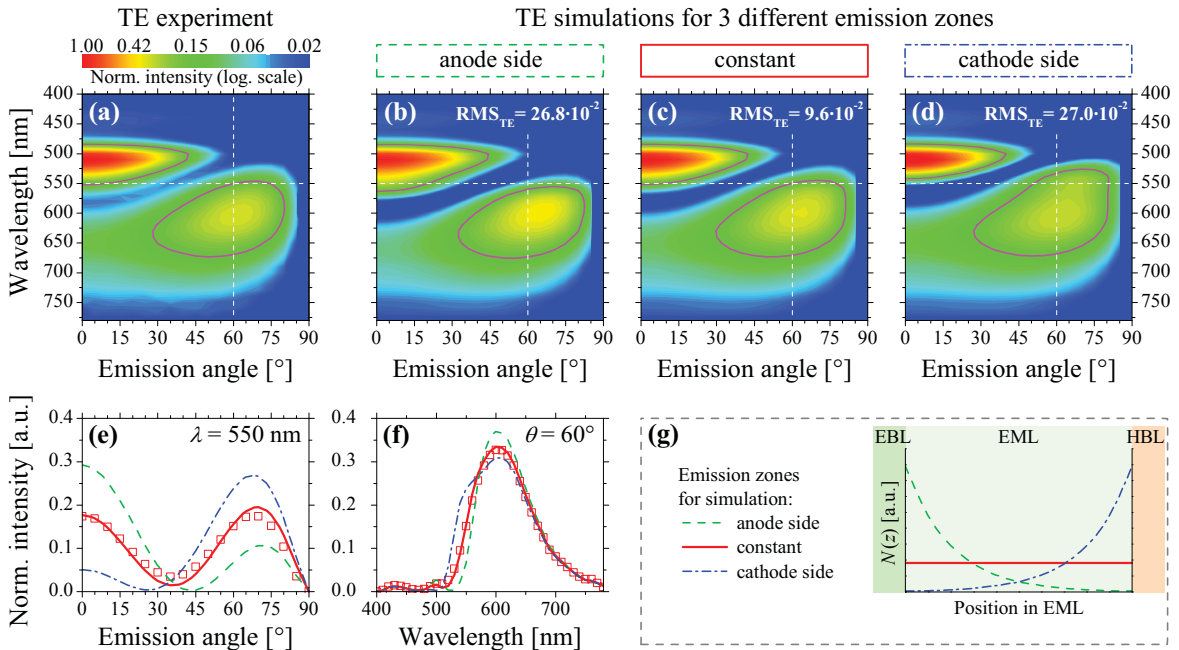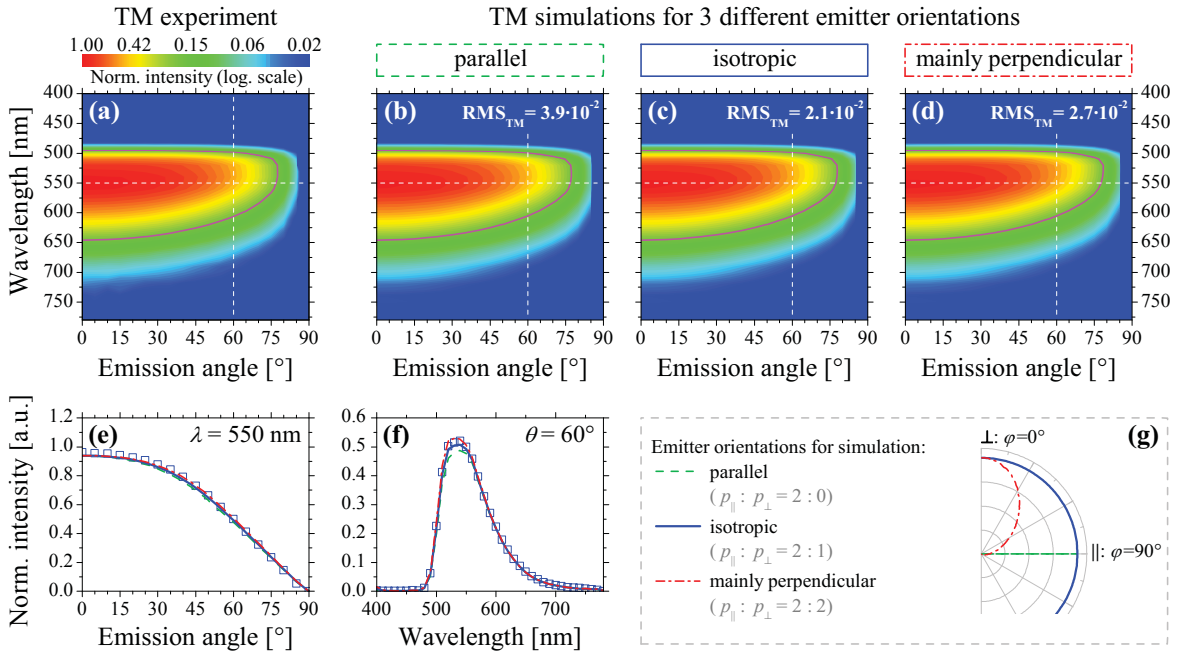

Figure 6.2. Emission zone in Ir(ppy)$_3$ PhOLED [B]. Experimental and theoretical TE polarized emission patterns of the Ir(ppy)$_3$ PhOLED [B] comprising 125 nm ETL. False color plots (a)-(d) exhibit a logarithmic intensity scale, the value 0.15 is accentuated by a magenta line, cross sections at $\theta = 60°$ and $\lambda = 550\,\text{nm}$ are indicated by white dashed lines. Cross section data for $\lambda = 550\,\text{nm}$ (e) and $\theta = 60°$ (f) are plotted: experimental data (squares) and theoretical predictions (lines). Simulation results for three different emission zones (g) are shown: anode-sided [(b), green dashed line in (e)-(f)] and cathode-sided emission [(d), blue dash-dotted line in (e)-(f)] fail to yield a match to the experiment. A constant emission zone [(c), red solid line in (e)-(f)] gives the lowest RMS$_{\text{TE}}$.

the destructive interference condition significantly depends on the distance of the emissive sites to the cathode. In this context, Fig. 6.2(e) is most meaningful: the ratio of emission in forward direction and in oblique angles is significantly different for the three emission zones, and the angular position of destructive interference shifts considerably. Assuming a balanced, constant emission zone improves the overall agreement between experiment and simulation approximately threefold compared to an exponential emission zone at either interface of the EML. This result seems reasonable regarding the 10 nm EML thickness which is in the same order of magnitude as the exciton diffusion length in comparable emissive systems [109, 110].

In a subsequent analysis step, the emitter orientation in Ir(ppy)$_3$ is investigated. Figure 6.3 shows the TM polarized measured and simulated radiation patterns of the Ir(ppy)$_3$ PhOLED [A] that is optimized for maximum optical performance. The simulations have been carried out for three very different emitter orientations depicted schematically in Fig. 6.3(g):

Figure 6.3. Emitter orientation in Ir(ppy)$_3$ PhOLED [A]. Experimental and theoretical TM polarized emission patterns of the Ir(ppy)$_3$ PhOLED [A] comprising 59 nm ETL. False color plots (a)-(d) exhibit a logarithmic intensity scale, the value 0.2 is accentuated by a magenta line, cross sections at $\theta = 60°$ and $\lambda = 550$ nm are indicated by white dashed lines. Cross section data for $\lambda = 550$ nm (e) and $\theta = 60°$ (f) are plotted: experimental data (squares) and theoretical predictions (lines). Simulation results for three different emitter orientations [normalized polar-plots of $g(\varphi)$ are drawn in (g)] are shown: parallel [(b), green dashed line in (e)-(f)], isotropic [(c), blue solid line in (e)-(f)], and mainly perpendicular [(d), red dash-dotted line in (e)-(f)]. All assumptions yield a perfect match to the experiment, allowing no conclusion to the actual emitter orientation.

parallel, isotropic, and mainly perpendicular dipole orientation, with a ratio of 2:0, 2:1, and 2:2 contributions from parallel to perpendicular emitters, respectively. Notice that the distributions shown in Fig. 6.3(g) are normalized to the maximum value. The corresponding formula are (i) parallel: $g(\varphi) = \delta(\varphi - \pi/2)$; (ii) isotropic: $g(\varphi) = 0.5$; (iii) mainly perpendicular: $g(\varphi) = \exp[-(\varphi^2/(0.32\pi)^2)]$. Although these three emitter orientations are significantly different, all assumptions yield a perfect match between experiment and simulation. This is due to the fact that perpendicular dipole components are "invisible" in the optical far field relative to the rather intense emission from parallel ones (see Fig. 4.2 for $k \cdot d \approx \pi/2$). As a consequence, no information about the emitter orientation can be obtained from the radiation pattern of this conventional OLED stack that is optimized for maximum performance.

By contrast, the optical far field of an OLED is very sensitive to the contribution of perpendicular emitters if the layered system is designed to yield a weak outcoupling of radiation from
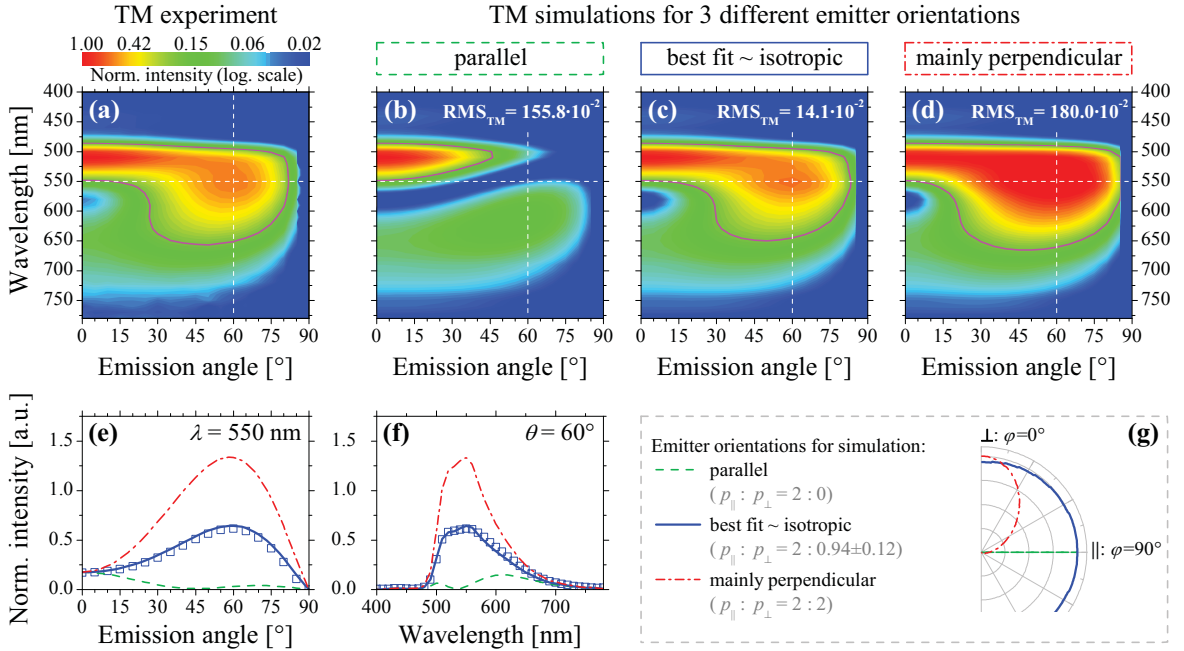

Figure 6.4. Emitter orientation in Ir(ppy)$_3$ PhOLED [B]. Experimental and theoretical TM polarized emission patterns of the Ir(ppy)$_3$ PhOLED [B] comprising 125 nm ETL. False color plots (a)-(d) exhibit a logarithmic intensity scale, the value 0.2 is accentuated by a magenta line, cross sections at $\theta = 60°$ and $\lambda = 550$ nm are indicated by white dashed lines. Cross section data for $\lambda = 550$ nm (e) and $\theta = 60°$ (f) are plotted: experimental data (squares) and theoretical predictions (lines). Simulation results for three different emitter orientations [normalized polar-plots of $g(\varphi)$ are drawn in (g)] are shown: parallel [(b), green dashed line in (e)-(f)] and mainly perpendicular [(d), red dash-dotted line in (e)-(f)] fail to yield a match to the experiment. A rather isotropic emitter orientation with $p_{\parallel}:p_{\perp} \approx 2:1$ [(c), blue solid line in (e)-(f)] gives a perfect fit to the experiment, and yields by far the lowest RMS$_{\mathrm{TM}}$. The expected isotropic emitter orientation in Ir(ppy)$_3$ is proven.

parallel dipole moments. This is realized for the $Ir(ppy)_3$ PhOLED [B], whose TM polarized measured and simulated radiation patterns are shown in Fig. 6.4. The destructive interference condition for radiation from parallel dipoles is well illustrated in Fig. 6.4(b): assuming only parallel dipoles significantly underestimates the TM emission obtained experimentally, and clearly indicates missing contributions from perpendicular dipole moments in the calculation. The measured TM polarized emission pattern can be modeled accurately across the whole spectral and angular range by including perpendicular dipole moments into the simulation (see Fig. 6.4(c)). A rather isotropic emitter orientation with $p_{\parallel} : p_{\perp} = 2 : (0.94 \pm 0.12)$ yields a perfect fit to the experimental data, confirming the expected isotropic emitter orientation in $Ir(ppy)_3$. The uncertainty of 0.12 is estimated from a doubling of the error function in the part of the radiation pattern that is highly sensitive to the exact emitter orientation.

These examples underline the importance of well-adapted OLED stacks in radiation pattern analyses. Performing experiments with conventional devices that are insensitive to the particular feature of interest is tenuous and might lead to wrong conclusions. On the other hand, devices with a well-adapted emitter-cathode distance allow for an accurate determination of e.g. the emission zone and emitter orientation. Notice that the constant emission zone and isotropic emitter orientation was confirmed by analyzing the radiation pattern of another suitable PhOLED of the fabricated series comprising 287 nm ETL thickness ($k \cdot d \approx 2\pi$, data not shown), indicating that these *active* optical properties of $Ir(ppy)_3$ do not depend on the emitter-cathode distance.

6.2 The internal electroluminescence spectrum of $Ir(ppy)_3$

The internal EL spectrum of $Ir(ppy)_3$ is simultaneously determined from the analysis discussed in the previous Sec. 6.1. According to Eq. (5.4), the spectrum is found by eliminating the spectral effects produced by the layered system from the TE polarized measured radiation pattern. For the three different emission zones assumed, the internal EL spectra that result from the analysis of the $Ir(ppy)_3$ PhOLEDs [A] and [B] are shown in Fig. 6.5(a) and (b), respectively. The $Ir(ppy)_3$ PhOLED [A] is optimized for maximum optical performance
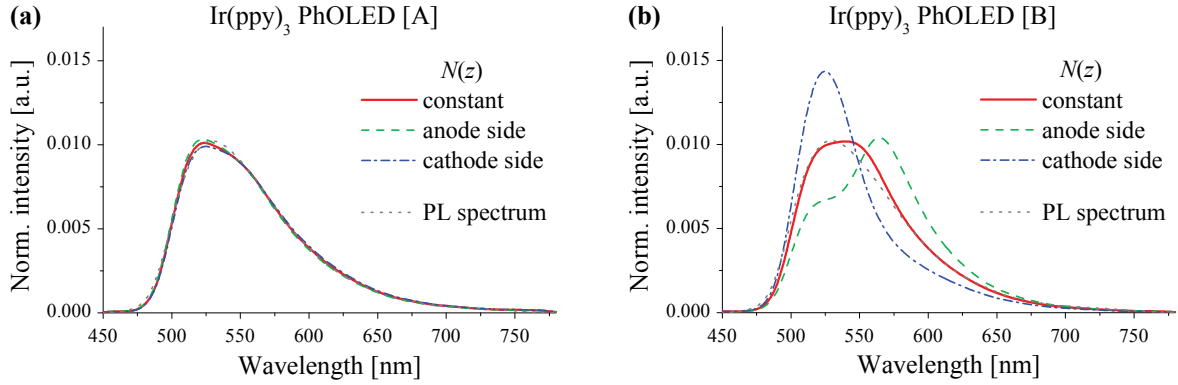
Figure 6.5. Internal EL spectrum of Ir(ppy)$_3$. Normalized internal EL spectra that result from the analysis of Ir(ppy)$_3$ PhOLEDs [A] (a) and [B] (b) are shown as well as the PL spectrum of Ir(ppy)$_3$. Three different emission zones (discussed in Sec. 6.1) were assumed for the analysis.

and induces relatively weak changes of the interference conditions for different emitter positions in the EML. Hence, all three resultant spectra shown in Fig. 6.5(a) are very similar to each other, no matter which emission zone is assumed for the calculation. Furthermore, the determined internal EL spectra are virtually identical to the PL spectrum of Ir(ppy)$_3$ from Ref. [150]. By contrast, the internal EL spectra that were determined during analysis of the Ir(ppy)$_3$ PhOLED [B] differ considerably (see Fig. 6.5(b)). This is due to the fact that the angular and spectral position of the destructive interference condition depends strongly on the exact position of the emissive sites in the EML (compare Figs. 6.2(b)-(d)). In the case of a cathode-sided emission zone, the destructive interference condition and resultant weak optical outcoupling efficiency is shifted toward shorter wavelengths compared to the constant emission zone (compare Figs. 6.2(c)-(d)). As a counter-mechanism, the resultant internal EL spectrum compensates this by an enhancement in this short-wavelength regime in order to fit the measured radiation pattern. However, assuming the correct emission zone, the resultant internal EL spectrum is again identical to the PL spectrum; a fact that confirms the quality of the experimental data and the simulation procedure for this multilayer stack.

These experiments demonstrate that the internal EL spectrum should be determined from an optically optimized device where the interference conditions are robust with respect to the actual position of the emissive site. However, it is worth to point out that an internal EL spectrum, which is determined by this procedure, is perfectly useful for "forward" simulations e.g. in optical device engineering. For radiation pattern analyses of single devices ("backward"

or reverse simulations) it is important to work with the spectrum that is delivered by the particular analysis (following Eq. (5.4)). To impose a spectrum that has been determined in a different way (e.g. in PL excitation, or with a different spectrometer) might induce slight spectral deviations that would probably lead to erroneous results.

6.3 The emission zone in the electron dominated polymer

In Section 6.1, the emission zone in $Ir(ppy)_3$ based PhOLEDs with a very thin EML (10 nm thickness) has been investigated. In the following, the emission zone in the PLED structure (see Fig. 5.2) is analyzed in order to demonstrate the applicability of the introduced concepts to polymeric devices. As reported recently, the current in this emissive (spirofluorene polymer) material is dominated by electron transport [26]. In a polymer similar to the present one, the electron mobility was found to be two to three orders of magnitude larger than the hole mobility, presumably due to significant hole trapping on the hole transporting sites that are present in low concentration [151].

The TE polarized radiation pattern of the PLED comprising 133 nm LEP thickness ($k{\cdot}d\approx \pi$) is depicted in Fig. 6.6. For spectral components around $\lambda = 500$ nm, the spectral emission in forward direction and into oblique emission angles is considerably suppressed due to the desired destructive interference of parallel dipole contributions. Furthermore, as a result of the pronounced interference conditions at the position of the emissive sites, the angular radiation pattern deviate from a Lambertian-like emission significantly. This pronounced angular characteristics allows for an accurate determination of the emission zone.

For the following analysis of the radiation pattern, the wavelength-region 400 nm $\leq \lambda \leq$ 600 nm of significant internal LEP emission is used to evaluate the RMS errors. Exponential shaped emission zones centered at the HTL-LEP interface ($N(z) = (1/w)\exp[-z/w]$) with three different (exemplary) 1/e-widths are assumed for the simulations shown in Fig. 6.6. Since the device structure is most sensitive to the emission zone for $\lambda \approx 500$ nm, Fig. 6.6(e) is most descriptive. Assuming a very narrow emission zone (w = 5 nm), the mean position of the emissive sites is too far away from the cathode, leading to an overestimation of emission

in the forward direction. In the case of a broader emission zone (w = 15 nm) with a mean position closer to the cathode, the emission in forward direction is underestimated and emission into oblique angles is more pronounced. Likewise, the position and depth of the destructive interference condition in the 60°-spectrum (Fig. 6.6(f)) varies for the different 1/e-widths: a narrow emission zone (w = 5 nm) yields rather sharp destructive interference, whereas on the other hand for a wider distribution (w = 15 nm) this condition cannot be met for all emissive sites and the destructive interference is smeared. It is found that a 1/e-width of (10±2) nm perfectly matches the experimental data. The uncertainty of ±2 nm is estimated from a doubling of the error-function in the part of the radiation pattern that is sensitive to the emission zone. Two other PLEDs of the fabricated series (comprising 109 nm and 168 nm LEP thickness) are suitable for an emission zone analysis. Within the precision of the experiment, both TE radiation patterns yield an emission zone identical to the above mentioned (data not shown), indicating that the emission zone is independent from the LEP thickness.
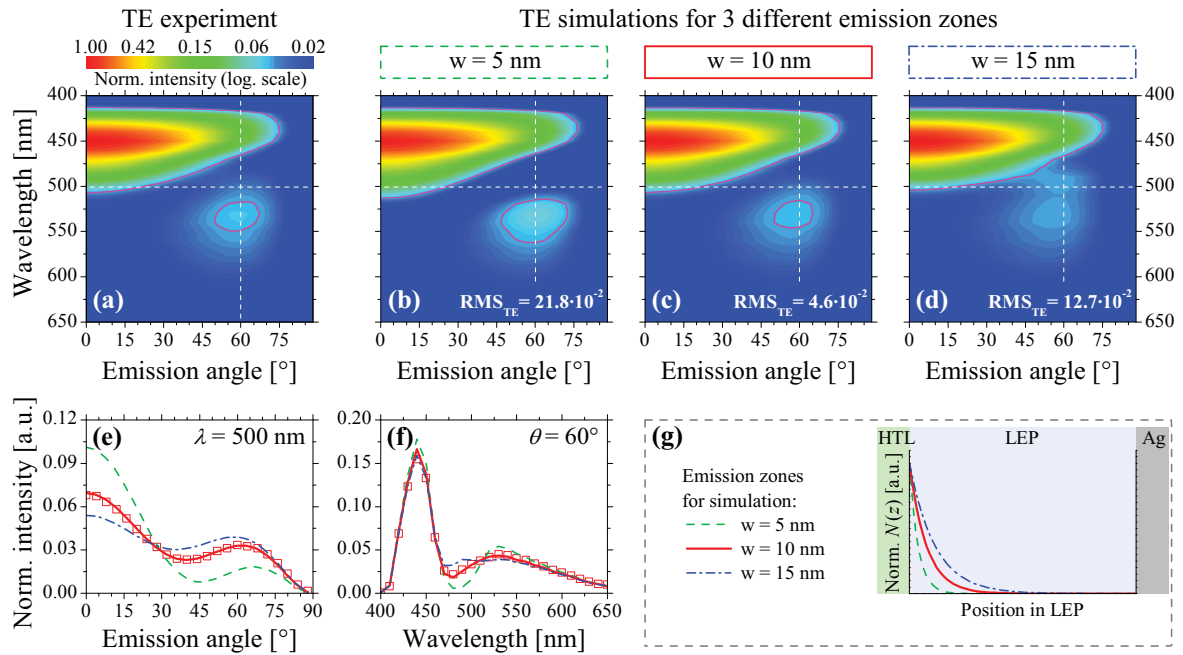
Figure 6.6. Emission zone in the blue PLED. Experimental and theoretical TE polarized emission patterns of the PLED comprising 133 nm LEP. False color plots (a)-(d) exhibit a logarithmic intensity scale, the value 0.04 is accentuated by a magenta line, cross sections at $\theta = 60°$ and $\lambda = 500$ nm are indicated by white dashed lines. Cross section data for $\lambda = 500$ nm (e) and $\theta = 60°$ (f) are plotted: experimental data (squares) and theoretical predictions (lines). Simulation results for three different exponential emission zones pinned at the HTL-LEP interface (g) are shown: 1/e-width of 5 nm [(b), green dashed line in (e)-(f)] and 15 nm [(d), blue dash-dotted line in (e)-(f)] fail to match the experimental data, whereas a 1/e-width of 10 nm [(c), red solid line in (e)-(f)] give a perfect fit.

Although the present study is *not* intended to develop models for the profile of the emission zone with an undisputable meaning to electrical device physics, some sanity check of the deduced exponential shape seems appropriate at this point. In fact, there are (at least) two possible causes that lead to an exponential shaped emission zone profile in this electron-dominated material [152]. First, since the electron-mobility is orders of magnitude larger than the hole-mobility [151], the excitons might be formed solely at the HTL-LEP interface. Provided that the excitons are not quenched at this interface, exciton diffusion into the LEP generates an exponential profile and the 1/e-width corresponds to the exciton diffusion length in the LEP. Second, the electrons might accumulate at the HTL-LEP interface forming a nearly homogeneous spatial electron distribution. A recombination with diffusive holes yields an exponential exciton profile and, provided that there is no exciton diffusion, the 1/e-width corresponds to the penetration depth of holes into the LEP. However, both scenarios might coincide in reality [152].

The angular emission characteristics cannot be modeled accurately assuming another emission zone of a different qualitative shape. A Gaussian profile centered at the HTL-LEP interface might still be physically meaningful. The fitting procedure converges to a center that is far outside the LEP toward the substrate when assuming a Gauss-shaped emission zone with a free center parameter. By this means, only the far-off tail of the Gauss profile is in the LEP region, which is virtually identical to an exponential profile. Likewise, the assumption of emission zone models with vanishing emission from the LEP interfaces, as demanded in Ref. [27], fail to deliver a sufficient match to the experiment. Solely an exponential profile leads to a satisfactorily agreement between simulated and experimental data.

6.4   The dipole emitter orientation in Ir(MDQ)$_2$(acac)

In Section 6.1, the dipole emitter orientation in Ir(ppy)$_3$ has been investigated and the commonly assumed isotropic orientation distribution for this small-molecular material was confirmed. In this section, the emitter orientation in the well-known red triplet-emitting material Ir(MDQ)$_2$(acac) is studied. For the Ir(MDQ)$_2$(acac) PhOLED system depicted in Fig. 5.3,

a 165 nm thick ETL induces destructive interference for emitters aligned parallel to the layers, while enhancing the emission of perpendicularly oriented emitters into the air half space, thus being a particularly sensitive probe for studying the presence of perpendicular dipoles. At first, the TE polarized emission pattern of this device is investigated (data not shown) and, like for the Ir(ppy)$_3$ PhOLEDs, a constant emission zone is found. Still, this result seems reasonable regarding the 10 nm EML thickness which is in the same order of magnitude as the exciton diffusion length in a comparable emissive system [153]. Figure 6.7 shows the experimentally observed radiation pattern for TM polarized emission accompanied by representative simulation results. The destructive interference condition for radiation from parallel dipoles is perfectly illustrated in Fig. 6.7(b). The experimental TM emission obtained in oblique angles is significantly underestimated when assuming parallel dipoles only. This clearly indicates missing contributions from perpendicular dipole moments in the calculation.
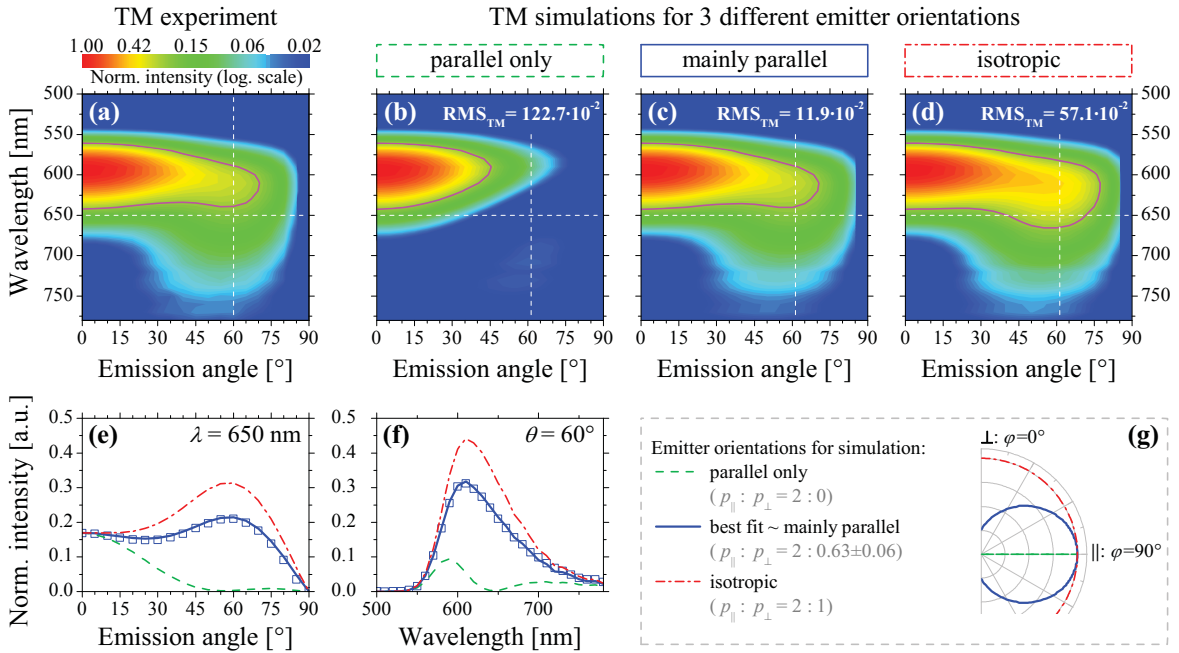
Figure 6.7. Emitter orientation in Ir(MDQ)$_2$(acac). Experimental and theoretical TM polarized emission patterns of the Ir(MDQ)$_2$(acac) PhOLED comprising 165 nm ETL. False color plots (a)-(d) exhibit a logarithmic intensity scale, the value 0.25 is accentuated by a magenta line, cross sections at $\theta = 60°$ and $\lambda = 650$ nm are indicated by white dashed lines. Cross section data for $\lambda = 650$ nm (e) and $\theta = 60°$ (f) are plotted: experimental data (squares) and theoretical predictions (lines). Simulation results for three different emitter orientations [normalized polar-plots of $g(\varphi)$ are drawn in (g)] are shown: parallel [(b), green dashed line in (e)-(f)] and isotropic [(d), red dash-dotted line in (e)-(f)] fail to yield a match to the experiment. A mainly parallel emitter orientation with $p_{||} : p_\perp = 2 : 0.63$ [(c), blue solid line in (e)-(f)] gives a perfect fit to the experiment.

Including perpendicular dipole moments into the simulation enables for accurately modeling the measured TM polarized emission pattern across the whole spectral and angular range (see Fig. 6.7(c)). Interestingly, the expected isotropic emitter orientation clearly overestimates the measured radiation pattern (see Fig. 6.7(d)), indicating that less perpendicular dipoles contribute to the device emission. Surprisingly, a mainly parallel emitter orientation with $p_{||}:p_{\perp}=2:(0.63\pm0.06)$ yields a perfect fit to the experimental data. The uncertainty of 0.06 is estimated from a doubling of the error function in the part of the radiation pattern that is highly sensitive to the exact emitter orientation.

This truly surprising result is obtained in an operating OLED with the only difference to an optimized stack being a thicker ETL. It is the first notification of a phosphorescent emissive material with non-isotropic, mainly parallel aligned emissive dipole transition moments. This feature is probably related to the morphology of the α-NPD matrix blended with the $Ir(MDQ)_2(acac)$ chromophore. However, the interaction of the asymmetric molecules during co-evaporation and the resultant predominantly parallel orientation of the dipole transition moments are not fully understood yet. Additional investigations potentially utilizing more sophisticated spectroscopic techniques are needed in order to further exploit this effect.

As elaborated in Sec. 3.4, the radiation pattern of OLEDs is generated by an ensemble of emissive sites. Assuming that the orientation of the emissive dipole moments $g(\varphi)$ follows e.g. a Gaussian distribution, the result $p_{||}:p_{\perp}=2:0.63$ means that the dipoles stagger around the preferred parallel direction with a 1/e-angle of about $\pm67°$. Notice that the mainly parallel emitter orientation (and constant emission zone) was confirmed by analyzing the radiation pattern of another suitable $Ir(MDQ)_2(acac)$ PhOLED of the fabricated series comprising 334 nm ETL thickness ($k \cdot d \approx 2\pi$, data not shown), indicating that these *active* optical properties of $Ir(MDQ)_2(acac)$ do not depend on the emitter-cathode distance. Furthermore, the mainly parallel emitter orientation of $Ir(MDQ)_2(acac)$ has been confirmed independently using optically excited luminescence (see Ref. [36] and references therein).

6.5   Internal luminescence quantum efficiencies q

In the following, the internal luminescence quantum efficiencies of the three emissive systems under study is determined from devices in electrical operation following the approach introduced in Sec. 4.6. For this analysis it is necessary to recapitulate the *active* optical properties of the emitters that are known until here because these enable to calculate a q-dependent relative excited state lifetime or transition rate $\tau_{rel} = 1/\Gamma_{rel}$.

For the blue polymeric emitter, an exponential emission zone at the HTL-LEP interface with an $1/e$-width of (10 ± 2) nm was measured in Sec. 6.3. The internal EL spectrum is found in Ref. [26] and the dipole emitter orientation has been measured to $p_{||}:p_{\perp}=2:(0.14\pm0.04)$ with the methods provided in this thesis (data not shown; see Ref. [34] for details), corresponding to the expected, nearly parallel orientation for this polymeric emitter.

The Ir(ppy)$_3$ emitter has been characterized systematically in this chapter, showing a constant emission zone and an isotropic dipole orientation (see Sec. 6.1) as well as an internal EL spectrum that is identical to the PL spectrum (see Sec. 6.2).

The Ir(MDQ)$_2$(acac) emissive system exhibits a constant emission zone (data not shown); the internal EL spectrum and the mainly parallel emitter orientation of $p_{||}:p_{\perp}=2:(0.63\pm0.06)$ was measured in Sec. 6.4.

In Sec. 4.6 it was claimed that any emission measure, that is related to the emitted power from a device, is suitable to sense the q-value from OLEDs with a varied emitter-cathode distance. In order to demonstrate this hypothesis, the following investigations utilize (i) the forward current efficiency for the PLED series, (ii) the forward radiance at the mean wavelength of the internal EL spectrum for the Ir(ppy)$_3$ PhOLED series, and (iii) the forward radiant intensity for the Ir(MDQ)$_2$(acac) PhOLED series. The current efficiencies of the PLEDs were measured with a calibrated photodiode[a] and the latter two values can easily be deduced from the measured radiation patterns of all devices, provided that these are relatively comparable (e.g. identical OLED-detector distance during all measurements).

---

[a]These values have been measured by Dr. Malte C. Gather, former member of Prof. Klaus Meerholz Group (University of Cologne).

First, the q-value of the polymeric emissive material is studied. Figure 6.8(a) illustrates
that the radiative lifetime of the emitter will be significantly lowered close to the cathode due
to the strong coupling to the surface plasmon polariton mode. Correspondingly, the radiative
rate will be enhanced. As expected from Eq. (3.19), the effect on the lifetime/transition rate
is more pronounced for high-q emitters whereas the lifetime/transition rate remains almost
unaffected for low values of q. For distances to the cathode $> 100\,\mathrm{nm}$, variations in the ra-
diative decay rate remain rather small. Figure 6.8(b) shows the normal incidence current
efficiencies of all PLEDs at a constant current density of $5\,\mathrm{mA/cm^2}$. The data for the two
thinnest devices (LEP thicknesses $10\,\mathrm{nm}$ and $18\,\mathrm{nm}$) are shown for completeness only. Since
they were electrically fairly unstable and suffered from large dark current they were not in-
cluded in the analysis. However, the measured forward efficiency is considerably modulated
with increasing LEP thickness, exhibiting peak efficiencies of nearly $5\,\mathrm{cd/A}$. Figure 6.8(b)
also shows the the simulated forward luminous intensity $I_V = \int I^{cav}(0°, \lambda) \cdot V(\lambda)\,\mathrm{d}\lambda$ for some
representative values of q, where $V(\lambda)$ is the spectral luminous efficiency function for pho-
topic vision of the human eye. Since this calculation according to Eq. (3.28) yields relative
values, the theoretical curves are scaled with a single constant factor to match the absolute
experimental data. In Fig. 6.8(b), the separation of the curves for different values of q arises
from the $\tau_{rel} = 1/\Gamma_{rel}$ factor in Eq. (3.28) and vanishes at positions where $\Gamma_{rel} = 1$ as well as
for large LEP thicknesses, where the coupling to the surface plasmon is less pronounced. An
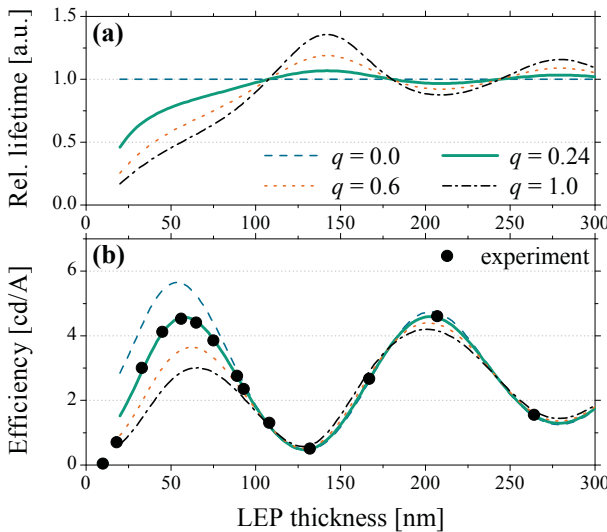
Figure 6.8. Measuring the q-value of the blue polymer. For the values $q = 0$ (blue, dashed), $q = 0.27$ (green, solid), $q = 0.6$ (orange, dotted), and $q = 1$ (black, dashed-dotted) are shown: (a) relative excited state lifetime of a representative emitter embedded $10\,\mathrm{nm}$ from the HTL-LEP interface (corresponding to the $1/e$-width of the emission zone) in the PLED stack shown in Fig. 5.2; (b) simulated $0°$-luminous intensity I_V and measured $0°$-current efficiencies at a current density of $5\,\mathrm{mA/cm^2}$ of blue PLEDs with different LEP thicknesses ($\bullet$, with confidence intervals smaller than the dot size).

internal luminescence quantum efficiency $q=0.24\pm0.07$ yields the best match between experimental and theoretical data. The slight difference to the result presented in Ref. [37], $q=0.27$, is due to the fact that the birefringence of the polymeric emissive material is neglected in the present study. This result indicates that only about a quarter of all excited singlet states in the device generate a photon. Provided that the singlet triplet factor is $\eta_{S/T}=0.25$ in this polymer, only 1/16 of all electron-hole pairs generate a photon, illustrating the tremendous optimization potential that results from the luminescent material utilized in these PLEDs.

A similar analysis is performed for the Ir(ppy)$_3$ PhOLED series. The modulation of the excited state lifetime with varying ETL thickness (Fig. 6.9(a)) is somewhat less pronounced compared to the PLED system (Fig. 6.8(a)) because the isotropic emitter orientation in Ir(ppy)$_3$ yields an averaged lifetime resulting from both, parallel and perpendicular dipole components. Figure 6.9(b) shows the measured forward radiance at the mean wavelength of the Ir(ppy)$_3$ internal EL spectrum and the corresponding calculated values $I^{air}(0°, 560\,\mathrm{nm})$ according to Eq. (3.28) for some representative q-values. An internal luminescence quantum efficiency of $q=0.26\pm0.1$ yields the best fit between experiment and simulation. Note that in Ref. [66], the current dependent Ir(ppy)$_3$ q-value has been determined by measuring the EQE of the same series of devices at different driving currents and subsequent reverse simulation. For this analysis, the scaling factors to the EQE-Eq. (3.31) (the charge balance factor γ and the singlet triplet factor $\eta_{S/T}$) were set to unity. However, the q-value from the present
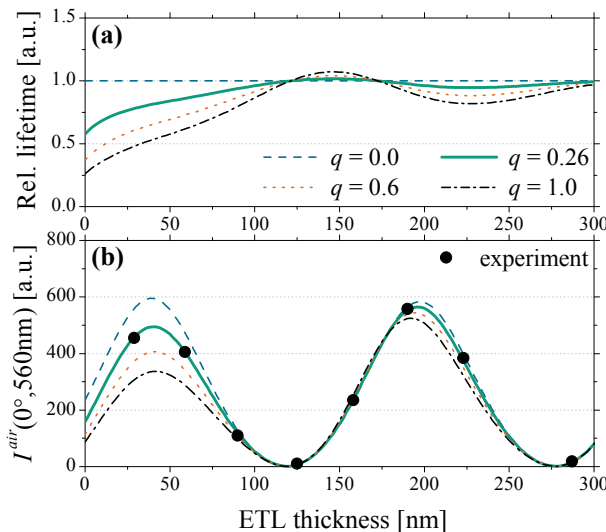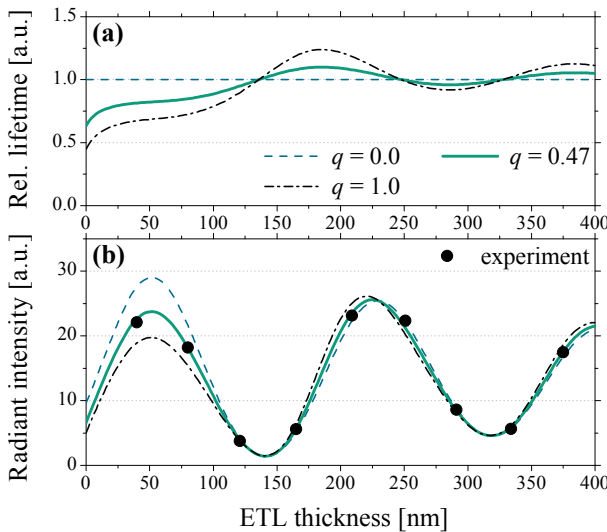

Figure 6.9. **Measuring the internal luminescence quantum efficiency q of Ir(ppy)$_3$.** For the values $q=0$ (blue, dashed), $q=0.26$ (green, solid), $q=0.6$ (orange, dotted), and $q=1$ (black, dashed-dotted) are shown: (a) relative excited state lifetime of a representative emitter embedded in the middle of the EML in the Ir(ppy)$_3$ PhOLED stack shown in Fig. 5.3; (b) simulated 0°-radiance $I^{air}(0°, 560\,\mathrm{nm})$ according to Eq. (3.28) and measured 0°-radiances at $j = 50\,\mathrm{mA/cm^2}$ of Ir(ppy)$_3$ PhOLEDs with different ETL thicknesses (●, with confidence intervals smaller than the dot size).

(relative) determination at a current density of $50\,\mathrm{mA/cm^2}$ shown in Fig. 6.9 fits perfectly to the results given in Ref. [66]. As a consequence, the two assumptions $\gamma \equiv 1$ and $\eta_{S/T} \equiv 1$ are justified for this current density.

By this means, a series of PhOLEDs with dramatically different layered systems is precisely described by optical simulations. Based on such successful quantitative optical analyses, reliable conclusions to other device parameters (γ, $\eta_{S/T}$) are feasible.

Finally, the q-value of $\mathrm{Ir(MDQ)_2(acac)}$ incorporated in the PhOLED system shown in Fig. 5.4 is determined. The measured forward radiant intensity at $j = 50\,\mathrm{mA/cm^2}$ and the simulated radiant intensity $I_e = \int I^{air}(0°,\lambda)\mathrm{d}\lambda$ is plotted in Fig. 6.10(b) for some representative values of q. An internal luminescence quantum efficiency of $q = 0.47 \pm 0.1$ yields the best fit between experimental and simulated values. For this phosphorescent material ($\eta_{S/T} \equiv 1$), at least about half of all generated electron-hole pairs generate a photon, still leaving some significant optimization potential on the luminescent material side.

All uncertainties to the q-values given in this section are estimated from a doubling of the respective deviation between experiment and simulation. Changing the input values mentioned at the beginning of this section within their confidence intervals, results in q-value changes well within the given error estimates. Notice that assuming different parameters for the systems properties cannot be compensated by an adapted q-value and vice versa – it would result in qualitative discrepancies between simulation and experiment.


Figure 6.10. Measuring the internal luminescence quantum efficiency q of $\mathrm{Ir(MDQ)_2(acac)}$. For the representative values $q = 0$ (blue, dashed), $q = 0.47$ (green, solid), and $q = 1$ (black, dashed-dotted) are shown: (a) relative excited state lifetime of a representative emitter embedded in the middle of the EML in the $\mathrm{Ir(MDQ)_2(acac)}$ PhOLED stack shown in Fig. 5.4; (b) simulated 0°-radiant intensity and measured 0°-radiant intensity at a current density of $50\,\mathrm{mA/cm^2}$ of $\mathrm{Ir(MDQ)_2(acac)}$ PhOLEDs with different ETL thicknesses (●, with confidence intervals smaller than the dot size).

Figures 6.8-6.10(b) show simulated optical forward efficiency curves for different bottom-emitting blue, green, and red OLED structures for some representative values of q. In consistence with Ref. [127] it is observed that the position of the first optical maximum shifts toward larger emitter-cathode distances for larger values of q. This is due to the enhanced energy loss into the surface plasmon mode (when the emitter is placed close to the cathode) with increasing q. For practical applications, the efficiencies at the first and the second optical maximum should be compared. It is evident that the global optimum depends on q. Low-q emitters should preferably be placed near the cathode. As proposed in Ref. [130], very efficient emissive materials ($q \rightarrow 1$) should be positioned at the second antinode of the reflective cathode, since the second optical maximum yields significantly higher efficiencies than the first. According to the presented considerations this rule is quite general for bottom emitting OLED structures with metal cathodes and rather independent of the detailed stack; the only limitation is a sufficient large q.

6.6 Current dependent device efficiency roll-off

The investigations of the q-value in the previous section are limited to a single current density for each device series. With increasing driving currents, however, the efficiency of OLEDs typically drops [49] which is disadvantageous for lighting applications at elevated brightness levels. This so-called 'efficiency roll-off' is typically attributed to annihilation processes that are particularly important for the longliving triplet excited states in phosphorescent materials [154]. Since numerous interactions between the excited states and/or the charge carriers can lead to additional non-radiative excited state depopulation, a detailed discussion on the underlying mechanisms is beyond the scope of the present work. However, the method presented in Sec. 4.6 provides a tool to measure the q-value in electrically operating devices by relative means and, thus, independent from other absolute factors like e.g. the charge recombination factor γ that might depend on the current density as well.

In the following, the efficiency roll-off of the Ir(MDQ)$_2$(acac) PhOLEDs is investigated. Because all other *active* optical properties of Ir(MDQ)$_2$(acac) enter the calculations, full
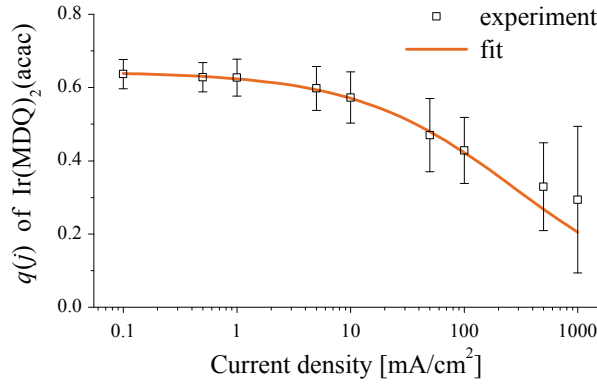
Figure 6.11. $q(j)$ of Ir(MDQ)$_2$(acac). Measured q-values of Ir(MDQ)$_2$(acac) plotted versus current density on a log scale. The value at $50\,\mathrm{mA/cm^2}$ corresponds to the analysis depicted in Fig. 6.10. Error bars are estimated as described in Sec. 6.5. The line is a least square fit of the function $q(j) = q_0/(1+(a \cdot j)^m)$ to the data (allowing a *qualitative* description only; see text). One meaningful parameter is extracted: $q_0 = 0.64$.

radiation patterns acquired at $j = 1\,\mathrm{mA/cm^2}$ and $j = 100\,\mathrm{mA/cm^2}$ were analyzed in advance (data not shown). It was found that neither the internal EL spectrum, nor the emission zone or emitter orientation of Ir(MDQ)$_2$(acac) vary in this current density range.

The forward radiant intensity of the Ir(MDQ)$_2$(acac) PhOLEDs was measured at different driving current densities ranging from $0.1\,\mathrm{mA/cm^2}$ to $1000\,\mathrm{mA/cm^2}$. Extracting the q-value (as explained in detail in the previous section) yields the data shown in Fig. 6.11. The experimental q-values are almost constant at low driving currents $j < 10\,\mathrm{mA/cm^2}$ and drop considerably for $j > 10\,\mathrm{mA/cm^2}$. At current densities above $100\,\mathrm{mA/cm^2}$, the error bars increase considerably indicating that the determined q-values are less reliable. This is possibly due to thermal effects or irreversible device modifications at these high driving currents. Thus, these values are excluded from further analysis.

A largely simplified function is fitted to describe the q-value roll-off versus current in a *qualitative* manner: $q(j) = q_0/(1+(a \cdot j)^m)$. This relation accounts for additional excited state depopulation due to current induced quenching and neglects annihilation due to an increased excited state density[b]. Nevertheless, one meaningful quantity is extracted from the fit: $q_0 = 0.64$, representing the low current limit ($j \to 0$) of q. It is the material parameter that would be measured in an infinite medium without interfaces and charge carriers present. Note

---

[b]The internal luminescence quantum efficiency is defined as the ratio of the radiative decay rate relative to the sum of all rates depopulating the excited state: $q(j) = \Gamma_r/(\Gamma_r + \Gamma_{nr} + \Gamma_{ad}(j))$. $\Gamma_{ad}(j)$ accounts for additional non-radiative excited state decay that might be current induced (depending on the charge density $\rho(j)$ with the rate Γ_ρ): $\Gamma_{ad}(j) \equiv \Gamma_\rho \cdot \rho(j)$. For the sake of simplicity and to omit tedious manipulations, excited state density dependent depopulation processes are neglected. It has been treated in detail elsewhere [155, 156] and does not improve the description of the experimental data. Assuming a power law dependence of the current dependent charge carrier density yields $q(j) = q_0/(1+(a \cdot j)^m)$.

that the fit-equation above intends to illustrate the characteristic efficiency roll-off *qualitatively* only. It is not intended to derive quantities for any, current or excited state related, quenching effects. A purely excited state associated quenching model (results not shown) fits the data similarly well. Thus, a detailed determination of the corresponding molecular parameters and effects requires more extensive experimental investigations as e.g. presented in Refs. [155, 156].

6.7   Oriented phosphorescent emitters boost OLED efficiency

The truly surprising result of a mainly parallel dipole emitter orientation in the phosphorescent small-molecular OLED emitter system of $Ir(MDQ)_2(acac)$ in α-NPD reveals: The orientation distribution of active sites in phosphorescent small molecule guest-host systems is not necessarily isotropic. Although the common assumption of isotropy yields a fraction of $p_{||} : p_\perp = 2 : 1$, a ratio of $p_{||} : p_\perp = 2 : 0.63$ has been determined here, corresponding to a predominantly parallel orientation. Consequently, one generally accepted argument applied to discussions of triplet emitting OLED devices must be revised. Beyond doubt, there are triplet emitters with isotropic orientation, as confirmed by the presented results on the $Ir(ppy)_3$ PhOLEDs in Sec. 6.1, but this attribute cannot be assumed generally.

By contrast, emitter orientation based optimization of OLED seems to be within reach, since parallel emitters preferably emit into air (see e.g. Fig. 4.2) and reduce the effect of surface plasmon polariton excitation at the cathode as optical loss channel. This optimization potential is illustrated in Fig. 6.12 that shows calculated EQE-values (according to Eq. (3.31))
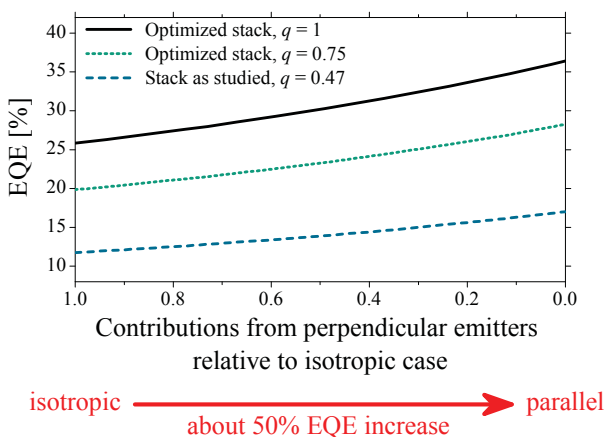
Figure 6.12. Emitter orientation potential to EQE improvement. Calculated EQE (for $Ir(MDQ)_2(acac)$ PhOLED stack shown in Fig. 5.4 with ETL thickness of 250 nm) vs. relative amount x of perpendicular emitters ($p_{||} : p_\perp = 2 : \nu$). Adjusting the HTL thicknesses to 65 nm and using $q = 0.75$ emitters yields potential device efficiencies of 20..30% (green, dotted). Extending the simulation towards ideal emitters ($q = 1$, black line) provides planar devices with efficiencies exceeding 35% EQE.

versus the emitter orientation. Considering the Ir(MDQ)$_2$(acac) PhOLED stack depicted in Fig. 5.4 with an optimal ELT thickness of 250 nm, together with the Ir(MDQ)$_2$(acac) emitter properties, yields an EQE of about 13%. Assuming an optimized stack (HTL thickness of 65 nm) and a more efficient, still realistic emitter ($q = 0.75$) yields efficiencies of 20..30% (green curve in Fig. 6.12). A further emitter based optimization toward an ideal quantum efficiency ($q = 1$) and an improved, predominantly parallel emitter orientation (with a ratio of $p_{||} : p_{\perp} = 2 : 0.14$ according to a realistic angular distribution with $\pm 22°$ total width) could increase this efficiency to reach EQE values $\approx 35\%$ (black curve in Fig. 6.12). Note that these efficiency values are given for the planar OLED system according to Fig. 5.4, avoiding more or less expensive internal or external outcoupling structures. A rough comparison of achievable EQE values according to Fig. 6.12 proves that a parallel orientation of the dipole transition moments boosts the efficiency of OLEDs by a factor of 1.5 compared to the commonly accepted belief of isotropic emitter orientation in phosphorescent materials.

Interestingly, EQE-values in excess of 30% – definitely not reachable with isotropic emitters (see Fig. 6.12) – have been reported recently for phosphorescent small-molecular emissive systems [157, 158], but without giving a sound explanation for this unexpected large number. The results presented in this section clearly demonstrate that an EQE-value in this range is feasible – without any outcoupling enhancement structures – by using phosphorescent emitters with their transition dipole moments being mainly oriented in the substrate plane. This finding opens up unforeseen possibilities for OLED improvement by controlling the molecular orientation of the emissive material.

Chapter 7

Conclusions and outlook

The *active* optical properties of the emitter materials are essential input parameters for quantitative optical analyses of OLEDs that already pave the way for optically optimized stack architectures in highly efficient lighting prototypes and applications. Researches in both, academia *and* industry are investigating optical loss channels in the OLED's layered system by means of optical simulation tools in order to derive promising concepts for a further enhancement of the overall device performance. Besides other factors, the prospects of success of such optimization strategies rely severely on the credibility of the optical input data.

An *in situ* characterization of OLEDs by radiation pattern measurements and corresponding optical reverse simulation is commonly performed by several research groups. Experiments under electrical excitation provide the inherent advantage over PL experiments that all possibly arising electrical side-effects are automatically included by the experiment. However, the strategic visualization of the particular internal feature of interest is absolutely essential to such analyses in order to obtain meaningful, precise, and indisputable results. Based on this idea, the present thesis provides a guideline to measure the *active* optical properties of OLED emitter materials *in situ* by radiation pattern analyses. Reliable and widely applicable methods are introduced to determine the internal EL spectrum, the profile of the emission zone, the dipole emitter orientation, and the internal luminescence quantum efficiency of emissive materials from the optical far field emission of OLEDs in electrical operation. For this purpose the layered system has to be well adapted to optically enhance the sensitivity of the emitter features in the OLED far field [39, 40]. Due to basic characteristics of the internal dipole

radiation, polarization dependent measurements allow to separate the contributions from differently oriented dipoles during the analysis. Thus, the particular properties of the emissive material can be investigated almost independently from each other by applying the outlined characterization strategies. Furthermore it is reasoned that the common use of an index-matched glass-hemisphere in order to access the substrate emission is actually not advisable for OLED emitter characterization by radiation pattern analyses [39].

The proposed characterization procedures are applied to sets of OLEDs containing a blue fluorescent polymeric material as well as a green $(Ir(ppy)_3)$ and a red $(Ir(MDQ)_2(acac))$ phosphorescent small-molecular emitter. On the one hand, quite expected results are obtained such as the isotropic dipole emitter orientation in $Ir(ppy)_3$, the constant emission zone in the $10\,nm$ thin small-molecular emissive layers, and the drop of the internal luminescence quantum efficiency with increasing current density. These commonly accepted findings confirm the introduced approaches in terms of their strategy as well as the way of performing the experiments and simulations. On the other hand, several novel and truly surprising results are found: The studies on the PLED system give the first direct optical evidence for electron-dominated current in the emissive layer of polymeric OLEDs [26]. The application of the emitter orientation measurement approach to the PLED system provides the first proof of the existence of perpendicular dipole moments even in polymeric emissive materials [34, 35].[a] Most importantly, this thesis contains the first report of a non-isotropic, mainly parallel emitter orientation in a phosphorescent small-molecular guest-host system [36].

Especially the latter result, that the well-known phosphorescent OLED emitter material $Ir(MDQ)_2(acac)$ shows a mainly parallel emitter orientation in an α-NPD matrix [36], holds tremendous impact on future OLED research activities. One generally accepted argument applied to discussions of triplet emitting devices must be revised and emitter orientation based optimization of phosphorescent OLEDs seems to be within reach. Since parallel dipoles emit preferably into air, the utilization of smart emissive materials with advantageous molecular orientation is capable to boost the efficiency of phosphorescent OLEDs by the factor 1.5.

---

[a]This data is not shown in the present work for reasons of conciseness.

Homogeneous systems without any presumably expensive internal or external outcoupling structure might deliver external quantum efficiencies in excess of 35%. Materials design, the influence of the matrix material and the substrate, as well as film deposition conditions are just a few parameters that need to be studied further in order to exploit the huge potential of the dipole emitter orientation in phosphorescent OLEDs.

The discovery of oriented phosphorescent emitters perfectly demonstrates how precise quantitative optical studies can provide an explanation of certain effects that were not understood before – such as an EQE in excess of 30% of planar systems. The methods presented in this thesis will provide a significant contribution to the advancement of OLEDs toward the lighting solution of tomorrow. These novel optical *in situ* investigation tools demand for an application on various scenarios of interest in future research and development activities. Analysis of white OLEDs (comprising blue, green and red emissive sites in one device) at various driving currents migth provide interesting results concerning the interaction of the different chromophores (e.g. 'triplet harvesting') in electrical operation. *In situ* measurements of the emission zone in electrically driven devices can yield valuable information about charge carrier behaviour and injection phenomena when combined with sophisticated electrical modeling tools. Other mechanisms like electron- or hole-trapping, the influence of a varied n- or p-doping concentration and the exactly required thickness of the electron- and hole-blocking layers might also be investigated by radiation pattern analyses of appropriate devices. Detailed studies on the internal luminescence quantum efficiency at different driving currents or device temperatures may provide valuable insight into the causes of the OLED efficiency drop at high current densities that is especially detrimental for high brigthnesses applications. A combination with other established PL spectroscopic methods might be usefull in some of these cases. For all mentioned future studies, a feedback loop with material manufacturers is desirable in order to actually transfer the results and derived concepts into tomorrows applications.

Bibliography

[1] C. W. Tang and S. A. VanSlyke, "Organic electroluminescent diodes", *Appl. Phys. Lett.* **51** (12), 913-915 (1987).

[2] B. W. D'Andrade and S. R. Forrest, "White Organic Light-Emitting Devices for Solid-State Lighting", *Adv. Mater.* **16** (18), 1585-1595 (2004).

[3] S. R. Forrest, "The path to ubiquitous and low-cost organic electronic appliances on plastic", *Nature* **428**, 911-918 (2004).

[4] R. U. A. Khan, C. Hunziker, and P. Günter, "Perspectives on organic light-emitting diodes for display applications", *J. Mater. Sci.: Mater. Electron.* **17**, 467-474 (2006).

[5] C. Adachi, M. A. Baldo, M. E. Thompson, and S. R. Forrest, "Nearly 100% internal phosphorescence efficiency in an organic light-emitting device", *J. Appl. Phys.* **90** (10), 5048-5051 (2001).

[6] J. H. Burroughes, D. D. C. Bradley, A. R. Brown, R. N. Marks, K. Mackay, R. H. Friend, P. L. Burn, and A. B. Holmes, "Light-emitting diodes based on conjugated polymers", *Nature* **347**, 539-541 (1990).

[7] K. Meerholz, "Device physics: Enlightening solutions", *Nature* **437**, 327-328 (2005).

[8] A. Köhnen, M. Irion, M. C. Gather, N. Rehmann, P. Zacharias, and K. Meerholz, "Highly color-stable solution-processed multilayer WOLEDs for lighting application", *J. Mater. Chem.* **20** (16), 3301-3306 (2010).

[9] M. C. Gather, R. Alle, H. Becker, and K. Meerholz, "On the Origin of the Color Shift in White-Emitting OLEDs", *Adv. Mater.* **19** (24), 4460-4465 (2007).

[10] M. C. Gather, A. Köhnen, and K. Meerholz, "White Organic Light-Emitting Diodes", *Adv. Mater.* **23** (2), 233-248 (2011).

[11] Y. Sun, N. C. Giebink, H. Kanno, B. Ma, M. E. Thompson, and S. R. Forrest, "Management of singlet and triplet excitons for efficient white organic light-emitting devices", *Nature* **440**, 908-912 (2006).

[12] G. Schwartz, M. Pfeiffer, S. Reineke, K. Walzer, and K. Leo, "Harvesting Triplet Excitons from Fluorescent Blue Emitters in White Organic Light-Emitting Diodes", *Adv. Mater.* **19** (21), 3672-3676 (2007).

[13] S. Reineke, F. Lindner, G. Schwartz, N. Seidler, K. Walzer, B. Lüssem, and K. Leo, "White organic light-emitting diodes with fluorescent tube efficiency", *Nature* **459**, 234-238 (2009).

[14] C. M. Ramsdale and N. C. Greenham, "The optical constants of emitter and electrode materials in polymer light-emitting diodes", *J. Phys. D: Appl. Phys.* **36** (4), L29-L34 (2003).

[15] M. Flämmich, N. Danz, D. Michaelis, A. Bräuer, M. C. Gather, J. H.-W. M. Kremer, and K. Meerholz, "Dispersion-model-free determination of optical constants: application to materials for organic thin film devices", *Appl. Optics* **48** (8), 1507-1513 (2009).

[16] J. A. E. Wasey, A. Safonov, I. D. W. Samuel, and W. L. Barnes, "Efficiency of radiative emission from thin films of a light-emitting conjugated polymer", *Phys. Rev. B* **64** (20), 205201 (2001).

[17] D. Yokoyama, M. Moriwake, and C. Adachi, "Spectrally narrow emissions at cutoff wavelength from edges of optically and electrically pumped anisotropic organic films", *J. Appl. Phys.* **103** (12), 123104 (2008).

[18] D. Yokoyama, A. Sakaguchi, M. Suzuki, and C. Adachi, "Horizontal orientation of linear-shaped organic molecules having bulky substituents in neat and doped vacuum-deposited amorphous films", *Org. Electron.* **10** (1), 127-137 (2009).

[19] J. Frischeisen, D. Yokoyama, C. Adachi, and W. Brütting, "Determination of molecular dipole orientation in doped fluorescent organic thin films by photoluminescence measurements", *Appl. Phys. Lett.* **96** (7), 073302 (2010).

[20] J. Frischeisen, D. Yokoyama, A. Endob, C. Adachi, and W. Brütting, "Increased light outcoupling efficiency in dye-doped small molecule organic light-emitting diodes with horizontally oriented emitters", *Org. Electron.* **12** (5), 809-817 (2011).

[21] H. Becker, S. E. Burns, and R. H. Friend, "Effect of metal films on the photoluminescence and electroluminescence of conjugated polymers", *Phys. Rev. B* **56** (4), 1893-1905 (1997).

[22] H.-W. Lin, C.-L. Lin, C.-C. Wu, T.-C. Chao, and K.-T. Wong, "Influences of molecular orientations on stimulated emission characteristics of oligofluorene films", *Org. Electron.* **8** (2-3), 189-197 (2007).

[23] J. Grüner, M. Remmers, and D. Neher, "Direct determination of the emission zone in a polymer light-emitting diode", *Adv. Mater.* **9** (12), 964-968 (1997).

[24] W. M. V. Wan, N. C. Greenham, and R. H. Friend, "Interference effects in anisotropic optoelectronic devices", *J. Appl. Phys.* **87** (5), 2542-2547 (2000).

[25] T. Granlund, L. A. A. Pettersson, and O. Inganäs, "Determination of the emission zone in a single-layer polymer light-emitting diode through optical measurements", *J. Appl. Phys.* **89** (11), 5897-5902 (2001).

[26] M. C. Gather, M. Flämmich, N. Danz, D. Michaelis, and K. Meerholz, "Measuring the profile of the emission zone in polymeric organic light-emitting diodes", *Appl. Phys. Lett.* **94** (26), 263301 (2009).

[27] S. L. M. van Mensfoort, M. Carvelli, M. Megens, D. Wehenkel, M. Bartyzel, H. Greiner, R. A. J. Janssen, and R. Coehoorn, "Measuring the light emission profile in organic light-emitting diodes with nanometre spatial resolution", *Nat. Photonics* **4**, 329-335 (2010).

[28] B. Perucco, N. A. Reinke, D. Rezzonico, M. Moos, and B. Ruhstaller, "Analysis of the emission profile in organic light-emitting devices", *Opt. Express* **18** (S2), A246-A260 (2010).

[29] S.-Y. Kim, D.-S. Leem, and J.-J. Kim, "Estimation of the mean emission zone in phosphorescent organic light-emitting diodes with a thin emitting layer", *Opt. Express* **18** (16), 16715-16721 (2010).

[30] A. Epstein, N. Tessler, and P. D. Einziger, "Analytical extraction of the recombination zone location in organic light-emitting diodes from emission pattern extrema", *Opt. Lett.* **35** (20), 3366-3368 (2010).

[31] B. Perucco, N. A. Reinke, F. Müller, D. Rezzonico, and B. Ruhstaller, "The influence of the optical environment on the shape of the emission profile and methods of its determination", *Proc. SPIE* **7722**, 77220F (2010).

[32] J.-S. Kim, P. K. H. Ho, N. C. Greenham, and R. H. Friend, "Electroluminescence emission pattern of organic light-emitting diodes: Implications for device efficiency calculations", *J. Appl. Phys.* **88** (2), 1073-1081 (2000).

[33] M.-H. Lu and J. C. Sturm, "Optimization of external coupling and light emission in organic light-emitting devices: modeling and experiment", *J. Appl. Phys.* **91** (2), 595-604 (2002).

[34] M. Flämmich, M. C. Gather, N. Danz, D. Michaelis, A. H. Bräuer, K. Meerholz, and A. Tünnermann, "Orientation of emissive dipoles in OLEDs: Quantitative in situ analysis", *Org. Electron.* **11** (6), 1039-1046 (2010).

[35] M. Flämmich, S. Roth, N. Danz, D. Michaelis, A. H. Bräuer, M. C. Gather, and K. Meerholz, "Measuring the dipole orientation in OLEDs", *Proc. SPIE* **7722**, 77220D (2010).

[36] M. Flämmich, J. Frischeisen, D. S. Setz, D. Michaelis, B. C. Krummacher, T. D. Schmidt, W. Brütting, and N. Danz, "Oriented phosphorescent emitters boost OLED efficiency", *Org. Electron.* **12** (10), 1663–1668 (2011).

[37] M. Flämmich, M. C. Gather, N. Danz, D. Michaelis, and K. Meerholz, "In situ measurement of the internal luminescence quantum efficiency in organic light-emitting diodes", *Appl. Phys. Lett.* **95** (26), 263306 (2009).

[38] M. Flämmich, N. Danz, D. Michaelis, C. A. Wächter, A. H. Bräuer, M. C. Gather, and K. Meerholz, "Measuring the internal luminescence quantum efficiency of OLED emitter materials in electrical operation", *Proc. SPIE* **7617**, 761715 (2010).

[39] M. Flämmich, D. Michaelis, and N. Danz, "Accessing OLED emitter properties by radiation pattern analyses", *Org. Electron.* **12** (1), 83-91 (2011).

[40] M. Flämmich, D. Michaelis, and N. Danz, "In situ measurement of spectrum, emission zone, and dipole emitter orientation in OLEDs", *Proc. SPIE* **7954**, 795410 (2011).

[41] J. Kalinowski, "Electroluminescence in organics", *J. Phys. D: Appl. Phys.* **32** (24), R179-R249 (1999).

[42] J. H. Round, "A Note on Carborundum", *Elect. World* **49**, 309 (1907).

[43] M. Pope, H. P. Kallmann, and P. Magnante, "Electroluminescence in Organic Crystals", *J. Chem. Phys.* **38** (8), 2042-2043 (1963).

[44] G. Gustafsson, Y. Cao, G. M. Treacy, F. Klavetter, N. Colaneri, and A. J. Heeger, "Flexible light-emitting diodes made from soluble conducting polymers", *Nature* **357**, 477-479 (1992).

[45] M. Berggren, O. Inganäs, G. Gustafsson, J. Rasmusson, M. R. Andersson, T. Hjertberg, and O. Wennerström, "Light-emitting diodes with variable colours from polymer blends", *Nature* **372**, 444-446 (1994).

[46] R. H. Friend, R. W. Gymer, A. B. Holmes, J. H. Burroughes, R. N. Marks, C. Taliani, D. D. C. Bradley, D. A. D. Santos, J. L. Bredas, M. Logdlund, and W. R. Salaneck, "Electroluminescence in conjugated polymers", *Nature* **397**, 121-128 (1999).

[47] M. Gross, D. C. Müller, H.-G. Nothofer, U. Scherf, D. Neher, C. Bräuchle, and K. Meerholz, "Improving the performance of doped π-conjugated polymers for use in organic light-emitting diodes", *Nature* **405**, 661-665 (2000).

[48] J. Kiso, M. Kimura, and K. Nagai, "Multilayer White Light-Emitting Organic Electroluminescent Device", *Science* **267** (5202), 1332-1334 (1995).

[49] M. A. Baldo, D. F. O'Brien, Y. You, A. Shoustikov, S. Sibley, M. E. Thompson, and S. R. Forrest, "Highly efficient phosphorescent emission from organic electroluminescent devices", *Nature* **395**, 151-154 (1998).

[50] M. A. Baldo, M. E. Thompson, and S. R. Forrest, "High-efficiency fluorescent organic light-emitting devices using a phosphorescent sensitizer", *Nature* **403**, 750-753 (2000).

[51] Z. Shen, P. E. Burrows, V. Bulovic, S. R. Forrest, and M. E. Thompson, "Three-Color, Tunable, Organic Light-Emitting Devices", *Science* **276** (5321), 2009-2011 (1997).

[52] C. D. Müller, A. Falcou, N. Reckefuss, M. Rojahn, V. Wiederhirn, P. Rudati, H. Frohne, O. Nuyken, H. Becker, and K. Meerholz, "Multi-colour organic light-emitting displays by solution processing", *Nature* **421**, 829-833 (2003).

[53] N. Tessler, G. J. Denton, and R. H. Friend, "Lasing from conjugated-polymer microcavities", *Nature* **382**, 695-697 (1996).

[54] V. G. Kozlov, V. Bulovic, P. E. Burrows, and S. R. Forrest, "Laser action in organic semiconductor waveguide and double-heterostructure devices", *Nature* **389**, 362-364 (1997).

[55] A. Dodabalapur, E. A. Chandross, M. Berggren, and R. E. Slusher, "Organic Solid-State Lasers: Past and Future", *Science* **277** (5333), 1787-1788 (1997).

[56] J. H. Burroughes, C. A. Jones, and R. H. Friend, "New semiconductor device physics in polymer diodes and transistors", *Nature* **335**, 137-141 (1988).

[57] Y. Yang and A. J. Heeger, "A new architecture for polymer transistors", *Nature* **372**, 344-345 (1994).

[58] C. W. Tang, "Two-layer organic photovoltaic cell", *Appl. Phys. Lett.* **48** (2), 183-185 (1986).

[59] J. J. M. Halls, C. A. Walsh, N. C. Greenham, E. A. Marseglia, R. H. Friend, S. C. Moratti, and A. B. Holmes, "Efficient photodiodes from interpenetrating polymer networks", *Nature* **376**, 498-500 (1995).

[60] M. Granström, K. Petritsch, A. C. Arias, A. Lux, M. R. Andersson, and R. H. Friend, "Laminated fabrication of polymeric photovoltaic diodes", *Nature* **395**, 257-260 (1998).

[61] J. H. Schön, C. Kloc, E. Bucher, and B. Batlogg, "Efficient organic photovoltaic diodes based on doped pentacene", *Nature* **403**, 408-410 (2000).

[62] P. Peumans, S. Uchida, and S. R. Forrest, "Efficient bulk heterojunction photovoltaic cells using small-molecular-weight organic thin films", *Nature* **425**, 158-162 (2003).

[63] Y. Sun and S. R. Forrest, "Enhanced light out-coupling of organic light-emitting devices using embedded low-index grids", *Nat. Photonics* **2**, 483-487 (2008).

[64] G. F. He, C. Rothe, S. Murano, A. Werner, O. Zeika, and J. Birnstock, "White stacked OLED with 38 lm/W and 100,000-hour lifetime at $1000\,\mathrm{cd/m^2}$ for display and lighting applications", *J. Soc. Inf. Display* **17** (2), 159-165 (2009).

[65] ORBEOS datasheet from www.osram.com, 29.03.2011.

[66] D. S. Setz, T. D. Schmidt, M. Flämmich, S. Nowy, J. Frischeisen, B. C. Krummacher, T. Dobbertin, K. Heuser, D. Michaelis, N. Danz, W. Brütting, and A. Winnacker, "Comprehensive efficiency analysis of organic light-emitting devices", *J. Photon. Energy* **1**, 011006 (2011).

[67] P. Zacharias, M. C. Gather, M. Rojahn, O. Nuyken, and K. Meerholz, "New Crosslinkable Hole Conductors for Blue-Phosphorescent Organic Light-Emitting Diodes", *Angew. Chem. Int. Edit.* **46** (23), 4388-4392 (2007).

[68] S. R. Forrest, "Ultrathin Organic Films Grown by Organic Molecular Beam Deposition and Related Techniques", *Chem. Rev.* **97** (6), 1793-1896 (1997).

[69] T. R. Hebner, C. C. Wu, D. Marcy, M. H. Lu, and J. C. Sturm, "Ink-jet printing of doped polymers for organic light emitting devices", *Appl. Phys. Lett.* **72** (5), 519-521 (1998).

[70] D. A. Pardo, G. E. Jabbour, and N. Peyghambarian, "Application of Screen Printing in the Fabrication of Organic Light-Emitting Devices", *Adv. Mater.* **12** (17), 1249-1252 (2000).

[71] N. Koch, "Organic Electronic Devices and Their Functional Interfaces", *Chem. Phys. Chem.* **8** (10), 1438-1455 (2007).

[72] R. Ballardini, G. Varani, M. T. Indelli, and F. Scandola, "Phosphorescent 8-quinolinol metal chelates. Excited-state properties and redox behavior", *Inorg. Chem.* **25** (22), 3858-3865 (1986).

[73] H. Yersin, ed., *Highly Efficient OLEDs with Phosphorescent Materials*, Wiley-VCH, Weinheim, 2008.

[74] X. Yang, D. Müller, D. Neher, and K. Meerholz, "Highly Efficient Polymeric Electrophosphorescent Diodes", *Adv. Mater.* **18** (7), 948-954 (2006).

[75] X.-H. Yang, F.-I. Wu, D. Neher, C.-H. Chien, and C.-F. Shu, "Efficient Red-Emitting Electrophosphorescent Polymers", *Chem. Mater.* **20**, 1629-1635 (2008).

[76] F.-I. Wu, X.-H. Yang, D. Neher, R. Dodda, Y.-H. Tseng, and C.-F. Shu, "Efficient White-Electrophosphorescent Devices Based on a Single Polyfluorene Copolymer", *Adv. Funct. Mater.* **17** (7), 1085-1092 (2007).

[77] T. Tsutsui, E. Aminaka, C. P. Lin, and D. U. Kim, "Extended molecular design concept of molecular materials for electroluminescence: sublimed–dye films, molecularly doped polymers and polymers with chromophores", *Phil. Trans. R. Soc. Lond. A* **355** (1725), 801-814 (1997).

[78] M. Pfeiffer, K. Leo, X. Zhou, J. S. Huang, M. Hofmann, A. Werner, and J. Blochwitz-Nimoth, "Doped organic semiconductors: Physics and application in light emitting diodes", *Org. Electron.* **4** (2-3), 89-103 (2003).

[79] M. A. Baldo, D. F. O'Brien, M. E. Thompson, and S. R. Forrest, "Excitonic singlet-triplet ratio in a semiconducting organic thin film", *Phys. Rev. B* **60** (20), 14422-14428 (1999).

[80] A. Köhler and H. Bässler, "Triplet states in organic semiconductors", *Mater. Sci. Eng.* **66** (4-6), 71-109 (2009).

[81] M. Wohlgenannt, K. Tandon, S. Mazumdar, S. Ramasesha, and Z. V. Vardeny, "Formation cross-sections of singlet and triplet excitons in π-conjugated polymers", *Nature* **409**, 494-497 (2001).

[82] J. S. Wilson, A. S. Dhoot, A. J. A. B. Seeley, M. S. Khan, A. Köhler, and R. H. Friend, "Spin-dependent exciton formation in π-conjugated compounds", *Nature* **413**, 828-831 (2001).

[83] M. Wohlgenannt, X. M. Jiang, Z. Vardeny, and R. A. J. Janssen, "Conjugation-Length Dependence of Spin-Dependent Exciton Formation Rates in π-Conjugated Oligomers and Polymers", *Phys. Rev. Lett.* **88** (19), 197401 (2002).

[84] A. Köhler and J. Wilson, "Phosphorescence and spin-dependent exciton formation in conjugated polymers", *Org. Electron.* **4** (2-3), 179-189 (2003).

[85] M. Reufer, M. J. Walter, P. G. Lagoudakis, B. Hummel, J. S. Kolb, H. G. Roskos, U. Scherf, and J. M. Lupton, "Spin-conserving carrier recombination in conjugated polymers", *Nat. Mater.* **4**, 340-346 (2005).

[86] C. Rothe, S. M. King, and A. P. Monkman, "Direct Measurement of the Singlet Generation Yield in Polymer Light-Emitting Diodes", *Phys. Rev. Lett.* **97** (7), 076602 (2006).

[87] M. Segal, M. A. Baldo, R. J. Holmes, S. R. Forrest, and Z. G. Soos, "Excitonic singlet-triplet ratios in molecular and polymeric organic materials", *Phys. Rev. B* **68** (7), 075211 (2003).

[88] E. M. Purcell, "Spontaneous emission probabilities at radio frequencies", *Phys. Rev.* **69** (11-12), 681 (1946).

[89] X.-W. Chen, W. C. H. Choy, C. J. Liang, P. K. A. Wai, and S. He, "Modifications of the exciton lifetime and internal quantum efficiency for organic light-emitting devices with a weak/strong microcavity", *Appl. Phys. Lett.* **91** (22), 221112 (2007).

[90] N. Danz, M. Flämmich, D. Michaelis, and C. A. Wächter, "Micro- and Nano-Optical Modeling of Organic LED", *Proc. IPNRA*, 2008.

[91] K. H. Drexhage, "Interaction of Light with Monomolecular Dye Layers", *Prog. Optics* **12**, 163-232 (1974).

[92] V. Cimrová, M. Remmers, D. Neher, and G. Wegner, "Polarized light emission from LEDs prepared by the Langmuir-Blodgett technique", *Adv. Mater.* **8** (2), 146-149 (1996).

[93] D. Poelman, R. L. van Meirhaeghe, W. H. Laflbre, and F. Cardon, "Spectral shifts in thin film electroluminescent devices: an interference effect", *J. Phys. D: Appl. Phys.* **25** (6), 1010-1013 (1992).

[94] U. Lemmer, R. Hennig, W. Guss, A. Ochse, J. Pommerehne, R. Sander, A. Greiner, R. F. Mahrt, H. Bässler, J. Feldmann, and E. O. Göbel, "Microcavity effects in a spin-coated polymer two-layer system", *Appl. Phys. Lett.* **66** (11), 1301-1303 (1995).

[95] S. E. Burns, N. Pfeffer, J. Grüner, M. Remmers, T. Javoreck, D. Neher, and R. H. Friend, "Measurements of Optical Electric Field Intensities in Microcavities Using Thin Emissive Polymer Films", *Adv. Mater.* **9** (5), 395-398 (1997).

[96] N. C. Greenham, R. H. Friend, and D. D. C. Bradley, "Angular Dependence of the Emission from a Conjugated Polymer Light-Emitting Diode: Implications for efficiency calculations", *Adv. Mater.* **6** (6), 491-494 (1994).

[97] K. A. Neyts, "Simulation of light emission from thin-film microcavities", *J. Opt. Soc. Am. A* **15** (4), 962-971 (1998).

[98] N. Danz, *Untersuchungen zur spontanen Emission von organischen Farbstoffmolekülen in Schichtsystemen.* PhD thesis, Friedrich-Schiller-University Jena, 2003.

[99] W. Lukosz and R. E. Kunz, "Light emission by magnetic and electric dipoles close to a plane interface. I. Total radiated power", *J. Opt. Soc. Am. A* **67** (12), 1607-1615 (1977).

[100] R. R. Chance, A. Prock, and R. Silbey, "Molecular Fluorescence and Energy Transfer Near Interfaces", *Adv. Chem. Phys.* **37**, 1-67 (1978).

[101] C. C. Katsidis and D. I. Siapkas, "General transfer-matrix method for optical multilayer systems with coherent, partially coherent, and incoherent interference", *Appl. Opt.* **41** (19), 3978-3987 (2002).

[102] J. Kalinowski, ed., *Organic Ligth-Emitting Diodes: Principles, Characteristics, and Processes*, Marcel Dekker, New York, 2005.

[103] B. Ruhstaller, T. Beierlein, H. Riel, S. Karg, J. Scott, and W. Riess, "Simulating electronic and optical processes in multilayer organic light-emitting devices", *IEEE J. Sel. Top. Quant.* **9** (3), 723-731 (2003).

[104] K. Müllen and U. Scherf, eds., *Organic Light Emitting Devices: Synthesis, Properties and Applications*, Wiley-VCH, Weinheim, 2006.

[105] S. Bange, *Transient Optical and Electrical Effects in Polymeric Semiconductors.* PhD thesis, University of Potsdam, 2009.

[106] E. Aminaka, T. Tsutsui, and S. Saito, "Effect of layered structures on the location of emissive regions in organic electroluminescent devices", *J. Appl. Phys.* **79** (11), 8808-8815 (1996).

[107] B. D'Andrade, M. Thompson, and S. Forrest, "Controlling Exciton Diffusion in Multilayer White Phosphorescent Organic Light Emitting Devices", *Adv. Mater.* **14** (2), 147-151 (2002).

[108] J. Hao, Z. Deng, and S. Yang, "Relationship between exciton recombination zone and applied voltage in organic light-emitting diodes", *Displays* **27** (3), 108-111 (2006).

[111] J.-W. Kang, S.-H. Lee, H.-D. Park, W.-I. Jeong, K.-M. Yoo, Y.-S. Park, and J.-J. Kim, "Low roll-off of efficiency at high current density in phosphorescent organic light emitting diodes", *Appl. Phys. Lett.* **90** (22), 223508 (2007).

[109] M. Lebental, H. Choukri, S. Chenais, S. Forget, A. Siove, B. Geffroy, and E. Tutis, "Diffusion of triplet excitons in an operational organic light-emitting diode", *Phys. Rev. B* **79** (16), 165318 (2009).

[110] Y. Divayana and X. Sun, "Existence of optimum intermolecular spacing for maximum exciton diffusion length in tris(2-phenylpyridine) iridium(III)", *Org. Electron.* **11** (1), 67-73 (2010).

[112] C. A. Wächter, N. Danz, D. Michaelis, M. Flämmich, S. Kudaev, A. H. Bräuer, M. C. Gather, and K. Meerholz, "Intrinsic OLED emitter properties and their effect on device performance", *Proc. SPIE* **6910**, 691006 (2008).

[113] M. Redecker, D. D. C. Bradley, M. Inbasekaran, and E. P. Woo, "Nondispersive hole transport in an electroluminescent polyfluorene", *Appl. Phys. Lett.* **73** (11), 1565-1567 (1998).

[114] B. Mazhari, "Impact of interfacial barriers on recombination profile in bilayer organic light-emitting diode", *Org. Electron.* **6** (5-6), 229-236 (2005).

[115] C.-H. Hsiao, Y.-H. Chen, T.-C. Lin, C.-C. Hsiao, and J.-H. Lee, "Recombination zone in mixed-host organic light-emitting devices", *Appl. Phys. Lett.* **89** (16), 163511 (2006).

[116] D. Poplavskyy and F. So, "Bipolar carrier transport in a conjugated polymer by complex admittance spectroscopy", *J. Appl. Phys.* **99** (3), 033707 (2006).

[117] N. Koch, A. Elschner, and R. L. Johnson, "Green polyfluorene-conducting polymer interfaces: Energy level alignment and device performance", *J. Appl. Phys.* **100** (2), 024512 (2006).

[118] J. A. E. Wasey, A. Safonov, I. D. W. Samuel, and W. L. Barnes, "Effects of dipole orientation and birefringence on the optical emission from thin films", *Opt. Commun.* **183** (1-4), 109-121 (2000).

[119] D. McBranch, I. H. Campbell, D. L. Smith, and J. P. Ferris, "Optical determination of chain orientation in electroluminescent polymer films", *Appl. Phys. Lett.* **66** (10), 1175-1177 (1995).

[120] C. Soc, D. Comoretto, F. Marabelli, and D. Moses, "Anisotropic photoluminescence properties of oriented poly(p-phenylene-vinylene) films: Effects of dispersion of optical constants", *Phys. Rev. B* **75** (7), 075204 (2007).

[121] S. H. Garrett, J. A. E. Wasey, and W. L. Barnes, "Determining the orientation of the emissive dipole moment associated with dye molecules in microcavity structures", *J. Mod. Optics* **51** (15), 2287-2295 (2004).

[122] M. C. Gather and D. D. C. Bradley, "An Improved Optical Method for Determining the Order Parameter in Thin Oriented Molecular Films and Demonstration of a Highly Axial Dipole Moment for the Lowest Energy pi-pi* Optical Transition in Poly(9,9- dioctylfluorene-co-bithiophene)", *Adv. Funct. Mater.* **17** (3), 479-485 (2007).

[123] S. M. King, H. L. Vaughan, and A. P. Monkman, "Orientation of triplet and singlet transition dipole moments in polyfluorene, studied by polarised spectroscopies", *Chem. Phys. Lett.* **440** (4-6), 268-274 (2007).

[124] P. W. Atkins, *Physikalische Chemie*, Wiley-VCH, Weinheim, 1990.

[125] L. H. Smith, J. A. E. Wasey, and W. L. Barnes, "Light outcoupling efficiency of top-emitting organic light-emitting diodes", *Appl. Phys. Lett.* **84** (16), 2986-2988 (2004).

[126] S. Nowy, B. C. Krummacher, J. Frischeisen, N. A. Reinke, and W. Brütting, "Light extraction and optical loss mechanisms in organic light-emitting diodes: Influence of the emitter quantum efficiency", *J. Appl. Phys.* **104** (12), 123109 (2008).

[127] B. C. Krummacher, S. Nowy, J. Frischeisen, M. Klein, and W. Brütting, "Efficiency analysis of organic light-emitting diodes based on optical simulation", *Org. Electron.* **10** (3), 478-485 (2009).

[128] N. Danz, R. Waldhäusl, A. Bräuer, and R. Kowarschik, "Dipole lifetime in stratified media", *J. Opt. Soc. Am. B* **19** (3), 412-419 (2002).

[129] L. H. Smith, J. A. E. Wasey, I. D. W. Samuel, and W. L. Barnes, "Light Out-Coupling Efficiencies of Organic Light-Emitting Diode Structures and the Effect of Photoluminescence Quantum Yield", *Adv. Funct. Mater.* **15** (11), 1839-1844 (2005).

[130] C.-L. Lin, T.-Y. Cho, C.-H. Chang, and C.-C. Wu, "Enhancing light outcoupling of organic light-emitting devices by locating emitters around the second antinode of the reflective metal electrode", *Appl. Phys. Lett.* **88** (8), 081114 (2006).

[131] N. Danz, D. Michaelis, and C. Wächter, "OLED design: combined micro-and nanophotonics modeling, and routes to a complex optimization algorithm", *Proc. SPIE* **6796**, 67963F (2007).

[132] N. C. Greenham, I. D. W. Samuel, G. R. Hayes, R. T. Phillips, Y. A. R. R. Kessener, S. C. Moratti, A. B. Holmes, and R. H. Friend, "Measurement of absolute photoluminescence quantum efficiencies in conjugated polymers", *Chem. Phys. Lett.* **241** (1-2), 89-96 (1995).

[133] P. E. Burrows, Z. Shen, V. Bulovic, D. M. McCarty, S. R. Forrest, J. A. Cronin, and M. E. Thompson, "Relationship between electroluminescence and current transport in organic hetero-junction light-emitting devices", *J. Appl. Phys.* **79** (10), 7991-8006 (1996).

[134] H. Murata, Z. H. Kafafi, and M. Uchida, "Efficient organic light-emitting diodes with undoped active layers based on silole derivatives", *Appl. Phys. Lett.* **80** (2), 189-191 (2002).

[135] D. M. Whittaker and I. S. Culshaw, "Scattering matrix treatment of patterned multilayer photonic structures", *Phys. Rev. B* **60** (4), 2610-2618 (1999).

[136] H. Greiner and O. J. F. Martin, "Numerical Modelling of Light Emission and Propagation in (Organic) LEDs with the Green's Tensor", *Proc. SPIE* **5214**, 248-259 (2004).

[137] K. Celebi, T. D. Heidel, and M. A. Baldo, "Simplified calculation of dipole energy transport in a multilayer stack using dyadic Green's functions", *Opt. Express* **15** (4), 1762-1772 (2007).

[138] "Radiating Slabs", contact norbert.danz@iof.fraunhofer.de for further information.

[139] J. C. Maxwell, "A Dynamical Theory of the Electromagnetic Field", *Phil. Trans. R. Soc. Lond.* **155**, 459-512 (1865).

[140] J. D. Jackson, *Klassische Elektrodynamik*, Walter de Gruyter, Berlin, New York, 2002.

[141] E. W. M. Born, *Principles of Optics*, Cambridge University Press, 1964.

[142] C.-T. Tai, *Dyadic Green's Functions in Electromagnetic Theory*, Intext, New York, 1971.

[143] H. Kuhn, "Classical Aspects of Energy Transfer in Molecular Systems", *J. Chem. Phys.* **53** (1), 101-108 (1970).

[145] W. Lukosz and R. E. Kunz, "Light emission by magnetic and electric dipoles close to a plane interface. III. Radiation patterns of dipoles with arbitrary orientation", *J. Opt. Soc. Am. A* **69** (11), 1495-1503 (1979).

[144] N. Danz, J. Heber, A. Bräuer, and R. Kowarschik, "Fluorescence lifetimes of molecular dye ensembles near interfaces", *Phys. Rev. A.* **66** (6), 063809 (2002).

[146] E. D. Palik, ed., *Handbook of Optical Constants of Solids*, Academic Press, New York, 1985.

[147] M. Gather, M. Flämmich, N. Danz, M. Kaiser, P. Zacharias, A. Köhnen, N. Rehmann, and K. Meerholz, "Where is the Dipole? Measuring and Optimizing the Emissive Dipole Distribution in Polymeric OLEDs", *Presentation at 7th International Conference on Electroluminescence of Molecular Materials and Related Phenomena, Dresden, Germany*, 2008.

[148] M. Roberts, "Optical modelling and efficiency optimization of P-OLED devices", *Proceedings of OEC' 06, Organic Electronics Conference, Frankfurt, Germany*, 2006.

[149] N. Ide, N. Matsusue, T. Kobayashi, and H. Naito, "Photoluminescence properties of facial- and meridional-Ir(ppy)3 thin films", *Thin Solid Films* **509** (1-2), 164-167 (2006).

[150] T. Asada, S. Hamamura, T. Matsushita, and S. Koseki, "Theoretical study on the absorption spectra of *fac*-Ir(ppy)$_3$ in the amorphous phase of organic electro-luminescent devices", *Res. Chem. Intermediat.* **35** (8-9), 851-863 (2008).

[151] S. Bange, A. Kuksov, and D. Neher, "Sensing electron transport in a blue-emitting copolymer by transient electroluminescence", *Appl. Phys. Lett.* **91** (14), 143516 (2007).

[152] D. Neher (University of Potsdam), personal communication, 18.05.2011.

[153] J. Wünsche, S. Reineke, B. Lüssem, and K. Leo, "Measurement of triplet exciton diffusion in organic light-emitting diodes", *Phys. Rev. B* **81** (24), 245201 (2010).

[154] W. Staroske, M. Pfeiffer, K. Leo, and M. Hoffmann, "Single-Step Triplet-Triplet Annihilation: An Intrinsic Limit for the High Brightness Efficiency of Phosphorescent Organic Light Emitting Diodes", *Phys. Rev. Lett.* **98** (19), 197402 (2007).

[155] S. Reineke, K. Walzer, and K. Leo, "Triplet-exciton quenching in organic phosphorescent light-emitting diodes with Ir-based emitters", *Phys. Rev. B* **75** (12), 125328 (2007).

[156] J. Kalinowski, M. Cocchi, V. Fattori, L. Murphy, and J. Williams, "Unified approach to electroluminescence efficiency in organic light-emitting diodes", *Org. Electron.* **11** (5), 724-730 (2010).

[157] P. A. Levermore, V. Adamovich, K. Rajan, W. Yeager, C. Lin, S. Xia, G. S. Kottas, M. S. Weaver, R. Kwong, R. Ma, J. J. Brown, and M. Hack, "Highly Efficient Phosphorescent OLED Lighting Panels for Solid-State Lighting", *Presentation at 48th Society for Information Display Symposium, Seattle, USA*, 2010.

[158] M. Hack, "Phosphorescent OLED Technology for Energy Efficient Solid State Lighting", *Presentation at 6th Global Plastic Electronics Conference & Exhibition, Dresden, Germany*, 2010.

List of figures

List of abbreviations

α-NPD .... N,N'-bis(naphthalen-1-yl)-N,N'-bis(phenyl)-2,2'-dimethylbenzidine

Ag .... silver

Alq$_3$ .... tris(8-hydroxy-quinolinato)aluminium

Ba .... barium

EBL .... electron-blocking layer

EIL .... electron-injection layer

EL .... electroluminescence

EML .... emissive layer

EQE .... external quantum efficiency

ETL .... electron-transport layer

HBL .... hole-blocking layer

HIL .... hole-injection layer

HOMO .... highest occupied molecular orbital

HTL .... hole-transport layer

Ir(MDQ)$_2$(acac) ...... iridium(III)bis(2-methyldibenzo-[f,h]quinoxaline)-(acetylacetonate)

Ir(ppy)$_3$ .... tris(2-phenyl-pyridine)iridium(III)

ITO .... indium-tin-oxide

LEP .... light-emitting polymer

LUMO .... lowest unoccupied molecular orbital

OLED .... organic light-emitting diode

PEDOT:PSS .... poly(3,4–ethylenedioxythiophene) poly(styrenesulfonate)

PhOLED .... phosphorescent organic light-emitting diode

PL .... photoluminescence

PLED .... polymeric organic light-emitting diode

PPV .... poly-(phenylene vinylene)

RMS .... root mean square

TE .... transverse electric

TM .... transverse magnetic

List of publications

A. Peer-reviewed papers

First author:

[1] M. Flämmich, J. Frischeisen, D. S. Setz, D. Michaelis, B. C. Krummacher, T. D. Schmidt, W. Brütting, and N. Danz, "Oriented phosphorescent emitters boost OLED efficiency", *Org. Electon.* **12** (10), 1663-1668 (2011). Bibliography item [36].

[2] M. Flämmich, D. Michaelis, and N. Danz, "Accessing OLED emitter properties by radiation pattern analyses", *Org. Electon.* **12** (1), 83-91 (2011). Bibliography item [39].

[3] M. Flämmich, M. C. Gather, N. Danz, D. Michaelis, A. H. Bräuer, K. Meerholz, and A. Tünnermann, "Orientation of emissive dipoles in OLEDs: Quantitative in situ analysis", *Org. Electon.* **11** (6), 1039-1046 (2010). Bibliography item [34].

[4] M. Flämmich, M. C. Gather, N. Danz, D. Michaelis, and K. Meerholz, "In situ measurement of internal electroluminescence quantum efficiency of emitter materials for organic light-emitting diodes", *Appl. Phys. Lett.* **95** (26), 263306 (2009). Bibliography item [37].

[5] M. Flämmich, N. Danz, D. Michaelis, A. Bräuer, M. C. Gather, J. H.-W. M. Kremer, and K. Meerholz, "Dispersion-model-free determination of optical constants: application to materials for organic thin film devices", *Appl. Optics* **48** (8), 1507-1513 (2009). Bibliography item [15].

Co-author:

[6] D. S. Setz, T. D. Schmidt, M. Flämmich, S. Nowy, J. Frischeisen, B. C. Krummacher, T. Dobbertin, K. Heuser, D. Michaelis, N. Danz, W. Brütting, and A. Winnacker, "Comprehensive efficiency analysis of organic light-emitting devices", *J. Photon. Energy* **1**, 011006 (2011). Bibliography item [66].

[7] M. C. Gather, M. Flämmich, N. Danz, D. Michaelis, and K. Meerholz, "Measuring the profile of the emission zone in polymeric organic light-emitting diodes", *Appl. Phys. Lett.* **94** (26), 263301 (2009). Bibliography item [26].

B. Conference papers

First author:

[8] M. Flämmich, D. Michaelis, and N. Danz, "In situ measurement of spectrum, emission zone, and dipole emitter orientation in OLEDs", *Proc. SPIE* **7954**, 795410 (2011). Bibliography item [40].

[9] M. Flämmich, D. Michaelis, N. Danz, C. Wächter, P. Dannberg, and A. H. Bräuer, "Micro-optical beam-shaper for tailoring light emission from OLEDs", *SPIE Photonics Europe*, 12.-16.04.2010, Brussels, Belgium. *Proc. SPIE* **7716**, 771616 (2010).

[10] M. Flämmich, S. Roth, N. Danz, D. Michaelis, A. H. Bräuer, M. C. Gather, and K. Meerholz, "Measuring the dipole orientation in OLEDs", *Proc. SPIE* **7722**, 77220D (2010). Bibliography item [35].

[11] M. Flämmich, N. Danz, D. Michaelis, C. Wächter, A. H. Bräuer, M. C. Gather, and K. Meerholz, "Measuring the internal luminescence quantum efficiency of OLED emitter materials in electrical operation", *Proc. SPIE* **7617**, 761715 (2010). Bibliography item [38].

Co-author:

[12] C. Wächter, N. Danz, D. Michaelis, M. Flämmich, S. Kudaev, A. H. Bräuer, M. C. Gather, and K. Meerholz, "Intrinsic OLED emitter properties and their effect on device performance", *Proc. SPIE* **6910**, 691006 (2008). Bibliography item [112].

C. Conference contributions

Invited talks:

[13] M. Flämmich, D. Michaelis, and N. Danz, "Optical Processes in OLEDs: Molecular Photonics", *Frühjahrstagung der Deutschen Physikalischen Gesellschaft (DPG)*, 13.-18.03. 2011, Dresden, Germany.

[14] M. Flämmich, D. Michaelis, N. Danz, D. Setz, B. Krummacher, J. Frischeisen, T. Schmidt, and W. Brütting, "Conclusive optical analysis of organic light-emitting devices", *6th Global Plastic Electronics Conference and Exhibition*, 19.-21.10.2010, Dresden, Germany.

Contributing talks:

[15] <u>M. Flämmich</u>, D. Michaelis, and N. Danz, "Optical Processes in OLEDs: Molecular Photonics", *Frühjahrstagung der Deutschen Physikalischen Gesellschaft (DPG)*, 13.-18.03. 2011, Dresden, Germany.

[16] <u>M. Flämmich</u>, D. Michaelis, and N. Danz, "In situ measurement of spectrum, emission zone, and dipole emitter orientation in OLEDs", *SPIE Photonics West*, 22.-27.01.2011, San Francisco, USA.

[17] <u>M. Flämmich</u>, S. Roth, N. Danz, D. Michaelis, A. H. Bräuer, M. C. Gather, and K. Meerholz, "Measuring the dipole orientation in OLEDs", *SPIE Photonics Europe*, 12.-16.04.2010, Brussels, Belgium.

[18] <u>M. Flämmich</u>, D. Michaelis, N. Danz, C. Wächter, P. Dannberg, and A. H. Bräuer, "Micro-optical beam-shaper for tailoring light emission from OLEDs", *SPIE Photonics Europe*, 12.-16.04.2010, Brussels, Belgium.

[19] <u>M. Flämmich</u>, N. Danz, D. Michaelis, C. Wächter, A. H. Bräuer, M. C. Gather, and K. Meerholz, "Measuring the internal luminescence quantum efficiency of OLED emitter materials in electrical operation", *SPIE Photonics West*, 27.-30.01.2010, San Francisco, USA.

[20] D. Michaelis, N. Danz, <u>M. Flämmich</u>, C. Wächter, P. Dannberg, and A. Bräuer, "Tailored light emission form OLEDs", *3rd EOS Topical Meeting on Optical Microsystems (OµS'09)*, 27.-30.09.2009, Capri, Italy.

Posters:

[21] <u>M. Flämmich</u>, N. Danz, D. Michaelis, C. A. Wächter, M. C. Gather, and K. Meerholz, "In situ determination of dipole emitter-orientation in organic light-emitting diodes", *4th European Conference on Organic Electronics and Related Phenomena (ECOER'07)*, 01.-04.10.2007, Varenna, Italy.

Co-author:

[22] <u>T. D. Schmidt</u>, D. S. Setz, B. Lebsanft, T. Wehlus, J. Frischeisen, B. C. Krummacher, M. Flämmich, N. Danz, and W. Brütting, "Determination of the effective radiative quantum efficiency of organic light-emitting guest-host systems", *Frühjahrstagung der Deutschen Physikalischen Gesellschaft (DPG)*, 13.-18.03.2011, Dresden, Germany.

[23] D. S. Setz, T. D. Schmidt, M. Flämmich, S. Nowy, <u>J. Frischeisen</u>, B. C. Krummacher, T. Dobbertin, K. Heuser, D. Michaelis, N. Danz, W. Brütting, and A. Winnacker, "Comprehensive efficiency analysis of organic light-emitting devices", *SPIE Optics + Photonics*, 21.-25.08.2010, San Diego, USA.

[24] <u>A. Bräuer</u>, D. Michaelis, N. Danz, M. Flämmich, C. Wächter, and P. Dannberg, "Tailored OLED light emission", *9th International Symposium on Advanced Organic Photonics (ISAOP-9)*, 03.-04.09.2009, Bunratty, Ireland.

[25] <u>D. Michaelis</u>, J. Kremer, N. Danz, M. Flämmich, C. Wächter, A. Bräuer, and K. Meerholz, "Micro-and Nano-optically structured Organic LEDs", *14th Microoptics Conference (MOC 08)*, 25.-27.09.2008, Brussels, Belgium.

[26] <u>M. Gather</u>, M. Flämmich, N. Danz, M. Kaiser, P. Zacharias, A. Köhnen, N. Rehmann, and K. Meerholz, "Where is the Dipole? Measuring and Optimizing the Emissive Dipole Distribution in Polymeric OLEDs", *7th International Conference on Electroluminescence of Molecular Materials and Related Phenomena (ICEL-7)*, 03.09.2008, Dresden, Germany.

[27] <u>N. Danz</u>, M. Flämmich, D. Michaelis, and C. A. Wächter, "Micro- and Nano-Optical Modeling of Organic LED", *Integrated Photonics and Nanophotonics Research and Applications (IPNRA)*, 13.-16.07.2008, Boston, USA.

[28] <u>C. Wächter</u>, N. Danz, D. Michaelis, M. Flämmich, S. Kudaev, A. H. Bräuer, M. C. Gather, and K. Meerholz, "Intrinsic OLED emitter properties and their effect on device performance", *Invited talk at SPIE Photonics West*, 19.-24.01.2008, San Jose, USA.

[29] <u>N. Danz</u>, M. Flämmich, D. Michaelis, C. A. Wächter, C. Pflumm, B. Fiebranz, and F. Voges, "Anomalous colour shift of OLED-substrate radiation due to bound modes", *4th European Conference on Organic Electronics and Related Phenomena (ECOER'07)*, 01.-04.10.2007, Varenna, Italy.

D. Patents

[30] W. Brütting, N. Danz, T. Dobbertin, M. Flämmich, J. Frischeisen, K. Heuser, B. Krummacher, N. Riegel, D. S. Setz, "Organische optoelektronische Bauelemente mit hoher Effizienz durch verbesserte Auskopplung mittels orientierten Farbstoffmolekülen in Guest-Host Systemen", *German Patent Application* DE 10 2010 054 893.6 (2010).

[31] D. Michaelis, C. Wächter, N. Danz, S. Kudaev, and M. Flämmich, "Beam shaper for use in organic LED, for producing radiation profile in e.g. region of projective display, has optical beam shaping elements provided with refractive elements and intensity modulating elements", WO 2010/112596 (2010).

Deutsche Kurzfassung

Seit dem ersten Bericht über eine organische licht-emittierende Diode (OLED) im Jahre 1987 [1] wurden beachtliche Anstrengungen unternommen um die Lebensdauer und Effizienz von OLEDs zu verbessern sowie die grundlegende Physik dieser Bauteile zu untersuchen. Auf Grund ihrer attraktiven Eigenschaften gelten OLEDs als vielversprechende Kandidaten für die Display- und Beleuchtungsanwendungen von morgen [2–4]. OLEDs sind dünn und leicht, und der Lichtentstehungsprozess der Elektrolumineszenz liefert eine hohe Elektronen-zu-Photonen Konversionseffizienz, denn im Idealfall wird aus jedem injizierten Ladungsträger ein Photon erzeugt [5]. Am wichtigsten aber ist, dass sich OLEDs konzeptionell von herkömmlichen punktförmigen Lichtquellen unterscheiden. OLEDs sind Flächenlichtquellen und das Licht entsteht in einer skalierbaren Fläche die bis zu Quadratmeter Abmessungen annehmen kann. Darüber hinaus verspricht das lösungsbasierte, nass-chemische Herstellungsverfahren sehr niedrige Produktionskosten, was insbesondere für eine Massenherstellung attraktiv ist [6–8]. Inspiriert von der Vision ergonomischer und ökonomischer, blendfreier, großflächiger Lichtkacheln entwickeln Forscher weltweit weiße OLEDs für die kommende Generation von Festkörperlichtquellen [9, 10]. Laborproben weißer OLEDs können bereits mit der Effizienz konventioneller Glühbirnen und Leuchtstoffröhren schritthalten [11–13] und seit kurzem sind erste Produkte kommerziell erhältlich.

Ein Faktor der die Bauteilleistung noch immer grundlegend limitiert ist die recht geringe Lichtextraktionseffizienz. Die Energie eines angeregten Emitters kann in verschiedene optische Kanäle abgestrahlt werden und lediglich ein geringer Anteil wird nutzenbringend in Luft ausgekoppelt. Wissenschaftler in Unternehmen und an Universitäten untersuchen den Schichtaufbau von OLEDs mit optischen Simulationsprogrammen um vielversprechende Konzepte

für die optische Bauteiloptimierung abzuleiten und letztlich effizientere, leistungsfähigere OLEDs zu entwickeln. Für solche Untersuchungen müssen allerdings die optischen Eigenschaften des internen Emissionsprozesses sowie die des OLED Schichtsystems gut bekannt sein. Die Verfügbarkeit von aussagekräftigen und belastbaren Eingangsdaten der optischen Bauteileigenschaften ist *die* fundamentale Voraussetzung für quantitative optische Simulationen und ganzheitliche Bauteilkonzepte.

Zum Zwecke der optischen Modellierung wird der Emissionsprozess der Elektrolumineszenz in OLEDs als Dipolübergang von einem angeregten molekularen Zustand in den Grundzustand behandelt. Hierbei ist wichtig, dass die Emission in einem Schichtsystem bzw. in einer ‚Mikrokavität' stattfindet. Die Wechselwirkung mit der lokalen Umgebung spielt eine erhebliche Rolle. Das Strahlungsfeld von OLEDs wird daher vom Zusammenspiel der *aktiven* optischen Eigenschaften des Emittermaterials und der *passiven* optischen Eigenschaften der Schichtsystems erzeugt. Unter den *aktiven* optischen Eigenschaften des Emittermaterials werden das interne Elektrolumineszenzspektrum, das Profil der Emissionszone, die Orientierungsverteilung der Dipolübergangsmomente sowie die interne Quanteneffizienz der Lumineszenz verstanden. Die *passiven* optischen Eigenschaften des Schichtsystems sind die Brechungsindizes und Schichtdicken der beteiligten Materialien. Während die *passiven* optischen Eigenschaften mit spektroskopischen Standardmethoden bestimmt werden können [14, 15], sind die *aktiven* optischen Eigenschaften schwieriger zu ermitteln. Häufig werden optisch angeregte Photolumineszenzexperimente durchgeführt um das Spektrum [16] und die molekulare Dipolorientierung des Emittermaterials zu bestimmen [17–20]. Allerdings ist ein ursprünglich optisch generierter angeregter Zustand nicht notwendigerweise identisch zu einem elektrisch angeregten Zustand [21]. Darüber hinaus können die internen Eigenschaften wie z.B. die Emitterorientierung von der genauen Schichtabscheidungsmethode oder etwaigen Nachbehandlungstechniken abhängen [22]. Daher sind *in situ* Untersuchungen an OLEDs wünschenswert. Ein vielversprechender Ansatz basiert dabei auf der Lösung des inversen Problems, d.h. der Rückwärtsrechnung vom gemessenen optischen Fernfeld von OLEDs im elektrischen Betrieb auf die internen Emittereigenschaften. Eine Vielzahl von mehr oder

weniger ausgeklügelten Methoden wurde bisher vorgestellt. Diese verwenden das gesamte winkel-, wellenlängen- und polarisationsaufgelöste Strahlungsfeld oder einige wichtige Anteile daraus um Rückschlüsse auf das Profil der Emissionszone [23–31] und die Orientierung der Dipolübergangsmomente zu ziehen [32, 33]. Allerdings gibt keine dieser Untersuchungen Aufschluss darüber, ob der beobachtete Teil des Strahlungsfeldes genügend Informationen über das zu bestimmende interne Merkmal trägt. Darüber hinaus behandelt keine dieser Untersuchungen die Fragestellung wie das OLED Schichtsystem angepasst werden müsste, um die Sensitivität der internen Eigenschaft von Interesse im OLED Fernfeld zu erhöhen. Weiterhin wurde bisher noch keine allgemeine Strategie erdacht, die es ermöglicht alle *aktiven* optischen Eigenschaften von OLED Emittermaterialien systematisch zu messen.

Die in der vorliegenden Dissertation eingeführten neuen Ansätze ermöglichen die akkurate *in situ* Bestimmung des internen Elektrolumineszenzspektrums, des Profils der Emissionszone, der Orientierung der Dipolübergangsmomente [34–36] sowie der internen Quanteneffizienz der Lumineszenz [37, 38] von OLED Emittermaterialien aus Messungen des optischen Fernfeldes von OLEDs im elektrischen Betrieb und dazugehörigen optischen Rückwärtsrechnungen. Die Verwendung von gut angepassten Schichtsystemen um die zu untersuchende Eigenschaft im Fernfeld optisch zu verstärken ist dabei eine fundmentale Idee die es erlaubt die internen Merkmale der Dipolemitter mit höchster Sensitivität zu beobachten [39, 40]. Grundlegende Charakteristika der internen Dipolabstrahlung erlauben es die Beiträge von verschieden orientierten Dipolen durch eine polarisationsaufgelöste Analyse zu unterscheiden. Weiterhin wird in der Arbeit dargelegt, dass die recht verbreitete experimentelle Verwendung einer brechungsindexangepassten Glashalbkugel (um das Strahlungsfeld im Substrat zugänglich zu machen) nicht ratsam ist [39]. Ein Leitfaden für die vollständige *in situ* Charakterisierung der *aktiven* optischen Eigenschaften von OLED Emittermaterialien wird entwickelt. Dieser ermöglicht es die zu untersuchende *aktive* optische Eigenschaft des Emittermaterials nahezu unabhängig von den anderen Emittereigenschaften zu bestimmen.

Die erarbeiteten Methoden werden auf Bauteilserien mit verschiedenen Emittermaterialien angewendet: ein blaues, fluoreszierendes polymeres Emittermaterial, sowie ein grünes

(Ir(ppy)$_3$) und ein rotes (Ir(MDQ)$_2$(acac)) phosphoreszierendes niedermolekulares Emitter-material. Auf der einen Seite werden dabei durchaus erwartete Resultate gefunden, wie z.B. die isotrope Emitterorientierung von Ir(ppy)$_3$, die konstante Emissionszone in den 10 nm dünnen niedermolekularen Schichten und der Abfall der internen Quanteneffizienz der Lumineszenz mit steigender Betriebsstromdichte. Diese allgemein anerkannten Resultate bestätigen die eingeführten Ansätze bezüglich ihrer grundsätzlichen Vorgehensweise sowie die Art und Weise der durchgeführten Experimente und Simulationen. Andererseits wurden aber auch neue, überraschende Ergebnisse gefunden: Die Untersuchungen der polymeren OLEDs liefern den ersten direkten optischen Beleg für Elektronen-dominierten Stromfluss in der Emitterschicht polymerer OLEDs [26]. Die Anwendung der Methode zum Messen der Emitterorientierung auf die blauen polymeren OLEDs erbringt den ersten Beweis der Existenz senkrechter Dipolmomente auch in polymeren Emittermaterialien [34, 35].[b] Als wichtigstes Resultat beinhaltet diese Dissertation den ersten Nachweis einer nicht-isotropen, vorzugsweise parallelen Emitterorientierung in einem phosphoreszierenden niedermolekularen Guest-Host System [36].

Besonders das letztere Resultat, die hauptsächlich parallele Emitterorientierung des wohlbekannten phosphoreszierenden OLED Emittermaterials Ir(MDQ)$_2$(acac) in einer α-NPD Trägermatrix [36], birgt enorme Konsequenzen auf künftige OLED Forschungsaktivitäten. Ein allgemein anerkanntes Argument in Diskussionen über Triplettemitter-OLEDs muss überdacht werden und emitterorientieungsbasierte Optimierung von OLEDs scheint in Reichweite zu gelangen. Parallele Emitter strahlen bevorzugt in Luft ab und können die Effizienz phosphoreszierender OLEDs um den Faktor 1.5 erhöhen. Ganz einfach durch die Nutzung intelligenter Emittermaterialien mit vorteilhafter molekularer Ausrichtung. Homogene OLED-Systeme ohne vermeintlich kostenintensive interne oder externe Auskoppelstrukturen könnten eine externe Quanteneffizienz (EQE) über 35% erzielen. Das konkrete Materialdesign, der Einfluss des Matrixmaterials und des Substrats sowie die verwendete Methode der OLED Herstellung sind lediglich einige Parameter die genauer untersucht werden müssen um das enorme Potential der Emitterorientierung in phosphoreszierenden OLEDs zu heben.

---

[b]Aus Gründen der Prägnanz sind diese Daten nicht Bestandteil der vorliegenden Arbeit.

Die Entdeckung einer bevorzugt parallelen Emitterorientierung in phosphoreszierenden OLEDs demonstriert anschaulich, wie quantitative optische Untersuchungen Erklärungen zu bestimmten Effekten liefern können, die vorher unverstanden waren – wie z.B. planare OLEDs mit EQEs über 30%. Die in dieser Dissertation vorgestellten Charakterisierungsansätze werden einen wichtigen Beitrag leisten um OLEDs als die Beleuchtungslösung von morgen weiter zu entwickeln. Die erarbeiteten Methoden stellen neuartige Werkzeuge dar, die künftig auf verschiedenste Fragestellungen in OLED-Forschung und -Entwicklung angewendet werden können. Eine genauere Untersuchung von weißen OLEDs (die aus blauen, grünen und roten Emittern bestehen) bei verschiedenen Stromdichten könnte aufschlussreiche Informationen über die Wechselwirkung verschiedener Chromophore (z.B. 'Triplet Harvesting') im elektrischen Betrieb des Bauteils liefern. *In situ* Messungen der Emissionszone in elektrisch betriebenen OLEDs könnten vielversprechende Ergebnisse z.B. über das Verhalten der Ladungsträger und Erkenntnisse über Injektionsbarrieren liefern, wenn sie mit gut durchdachten elektrischen Modellen kombiniert werden. Andere Effekte und Mechanismen wie z.B. das Besetzen von tiefen Fallenzuständen für Elektronen oder Löcher, der Einfluss einer geänderten negativen oder positiven Dotierkonzentration der Ladungsträgertransportschichten, oder die tatsächlich benötigte Dicke der Elektronen- und Lochblockerschichten können ebenfalls untersucht werden. Detaillierte Studien zur internen Quanteneffizienz der Lumineszenz bei erhöhten Stromdichten oder Bauteiltemperaturen könnten wertvolle Einblicke in die Ursachen des OLED Effizienzabfalles bei hohen Betriebsstömen liefern. Dieser ist besonders kritisch für Anwendungen die hohe Bauteilhelligkeiten verlangen. Eine Kombination mit anderen, etablierten Methoden der Photolumineszenzspektroskopie ist bei einigen Untersuchungen gewiss hilfreich. Für alle hier angedachten künftigen Forschungsvorhaben ist eine Rückkopplungsschleife mit OLED Materialherstellern wünschenswert um die erzielten Ergebnisse und Konzepte direkt in die OLED Anwendungen von morgen einfließen zu lassen.

Danksagung

Ich danke zu allererst Prof. Dr. Andreas Tünnermann für die Betreuung meiner Arbeit seitens der Friedrich-Schiller-Universität Jena sowie für die kritische Durchsicht und die konstruktiven Anregungen zur Verbesserung dieser Arbeit.

Die vorliegende Dissertation wurde am Fraunhofer-Institut für Angewandte Optik und Feinmechanik IOF, Jena, angefertigt. Die Unterstützung der Fraunhofer-Gesellschaft und die im Institut bereitgestellten Arbeitsbedingungen haben maßgeblichen Anteil am Gelingen der Arbeit. Die in der Arbeit vorgestellten Konzepte sind im Wesentlichen innerhalb der vom Bundesministerium für Bildung und Forschung geförderten Forschungsvorhaben "Hochwertige organische Leuchtdioden für Beleuchtungsanwendungen auf der Basis innovativer Technologien" (HOBBIT, FKZ 13N8951) und "Tausend Lumen organische Phosphoreszenzbauelemente für Anwendungen in Lichtsystemen" (TOPAS, FKZ 13N10474) entstanden.

Besonders großer Dank gilt meinen Betreuern Dr. Norbert Danz und Dr. Dirk Michaelis für ihre kontinuierliche Bereitschaft zur Diskussion der vielen "einfachen" Fragen und das Weitergeben ihrer Expertise. Es war und ist für mich stets Ansporn, dass beide jede Sachlage kritisch hinterfragen und genau zu verstehen versuchen. Dr. Danz bin ich im Besonderen dankbar für das nunmehr über eine Dekade andauernde "Mentoring". Neben den etwa tausend anderen wichtigen Aspekten habe ich von ihm gelernt die Ergebnisse wissenschaftlicher Arbeit auf eine prägnante und übersichtliche Art darzustellen.

Dr. Malte C. Gather aus der Arbeitsgruppe von Prof. Dr. Klaus Meerholz am Institut für Physikalische Chemie der Universität zu Köln bin ich für die äußerst gewissenhafte Herstellung und die Bereitstellung verschiedener Schichtproben, Mehrschichtproben und PLEDs sowie für alle fachlichen Diskussionen sehr dankbar. Einmal mit Profis zusammenarbeiten!

Ehrenwörtliche Erklärung

Ich erkläre hiermit ehrenwörtlich, dass ich die vorliegende Arbeit selbständig, ohne unzulässige Hilfe Dritter und ohne Benutzung anderer als der angegebenen Hilfsmittel und Literatur angefertigt habe. Die aus anderen Quellen direkt oder indirekt übernommenen Daten und Konzepte sind unter Angabe der Quellen gekennzeichnet.

Weitere Personen waren an der inhaltlich-materiellen Erstellung der vorliegenden Arbeit nicht beteiligt. Insbesondere habe ich hierfür nicht die entgeltliche Hilfe von Vermittlungs bzw. Beratungsdiensten (Promotionsberater oder andere Personen) in Anspruch genommen. Niemand hat von mir unmittelbar oder mittelbar geldwerte Leistungen für Arbeiten erhalten, die im Zusammenhang mit dem Inhalt der vorgelegten Dissertation stehen. Die Arbeit wurde bisher weder im In- noch im Ausland in gleicher oder ähnlicher Form einer anderen Prüfungsbehörde vorgelegt. Teile dieser Arbeit wurden jedoch aus Prioritätsgründen bereits veröffentlicht oder wurden zur Veröffentlichung eingereicht.

Die geltende Promotionsordnung der Physikalisch-Astronomischen Fakultät der Friedrich-Schiller-Universität Jena ist mir bekannt. Ich versichere ehrenwörtlich, dass ich nach bestem Wissen die reine Wahrheit gesagt und nichts verschwiegen habe.

Jena, 29. September 2011

Michael Flämmich

Lebenlauf

Persönliche Daten

Name	Michael Flämmich
Geburtsdatum	13.02.1982
Geburtsort	Jena

Ausbildung

1988 - 1991	Grundschule Erich-Weinert, Jena
1992 - 2000	Staatliches Gymnasium Am Anger, Jena
22.06.2000	Abitur am Gymnasium Am Anger, Jena
2001 - 2007	Studium der Physik an der Friedrich-Schiller-Universität Jena
2006 - 2007	Diplomarbeit zum Thema "Bestimmung des internen Elektrolumineszenzspektrums eines polymeren Emittermaterials für organische LEDs" am Fraunhofer-Institut für Angewandte Optik und Feinmechanik IOF, Jena
12.09.2007	Abschluss als Diplom-Physiker

Berufliche Tätigkeit

2000 - 2001	Zivildienst
seit 09/2007	Doktorand am Fraunhofer-Institut für Angewandte Optik und Feinmechanik IOF, Jena

Jena, 29. September 2011

_____

Michael Flämmich